



Calhoun: The NPS Institutional Archive
DSpace Repository

Theses and Dissertations

1. Thesis and Dissertation Collection, all items

2000-06

Impact analysis of a biomechanical model of the human thorax

Jolly, Johannes E.

Monterey, California. Naval Postgraduate School

<http://handle.dtic.mil/100.2/ADA379713>

Downloaded from NPS Archive: Calhoun



<http://www.nps.edu/library>

Calhoun is the Naval Postgraduate School's public access digital repository for research materials and institutional publications created by the NPS community. Calhoun is named for Professor of Mathematics Guy K. Calhoun, NPS's first appointed -- and published -- scholarly author.

Dudley Knox Library / Naval Postgraduate School
411 Dyer Road / 1 University Circle
Monterey, California USA 93943

NAVAL POSTGRADUATE SCHOOL

Monterey, California



THESIS

IMPACT ANALYSIS OF A BIOMECHANICAL MODEL OF THE HUMAN THORAX

by

Johannes E. Jolly

June 2000

Thesis Advisor:
Thesis Co-Advisor:

Young W. Kwon
Steven R. Baker

Approved for public release; distribution is unlimited.

DTIC QUALITY INSPECTED 4

20000724 040

REPORT DOCUMENTATION PAGE			Form Approved OMB No. 0704-0188	
Public reporting burden for this collection of information is estimated to average 1 hour per response, including the time for reviewing instruction, searching existing data sources, gathering and maintaining the data needed, and completing and reviewing the collection of information. Send comments regarding this burden estimate or any other aspect of this collection of information, including suggestions for reducing this burden, to Washington Headquarters Services, Directorate for Information Operations and Reports, 1215 Jefferson Davis Highway, Suite 1204, Arlington, VA 22202-4302, and to the Office of Management and Budget, Paperwork Reduction Project (0704-0188) Washington DC 20503.				
1. AGENCY USE ONLY (Leave blank)		2. REPORT DATE June 2000	3. REPORT TYPE AND DATES COVERED Master's Thesis	
4. TITLE AND SUBTITLE Impact Analysis of a Biomechanical Model of the Human Thorax			5. FUNDING NUMBERS	
6. AUTHOR(S) Jolly, Johannes E.				
7. PERFORMING ORGANIZATION NAME(S) AND ADDRESS(ES) Naval Postgraduate School Monterey CA 93943-5000			8. PERFORMING ORGANIZATION REPORT NUMBER	
9. SPONSORING/MONITORING AGENCY NAME(S) AND ADDRESS(ES)			10. SPONSORING/MONITORING AGENCY REPORT NUMBER	
11. SUPPLEMENTARY NOTES The views expressed here are those of the authors and do not reflect the official policy or position of the Department of Defense or the U.S. Government.				
12a. DISTRIBUTION/AVAILABILITY STATEMENT Approved for public release; distribution is unlimited.			12b. DISTRIBUTION CODE	
13. ABSTRACT (maximum 200 words) The biomechanical response of a finite element model of the human thorax and a protective body armor system was studied under impact loading from a projectile. The objective of the study was to create a viable finite element model of the human thorax. This objective was accomplished through the construction of a three-dimensional finite element model in DYNA3D, a finite element analysis program. The model was validated by comparing the results of tests of body armor systems conducted on cadavers to results obtained from finite element analysis. A parametric study was undertaken to determine the essential components of the model. The results from this investigation determined that the path of force propagation from a body armor system to the thorax upon bullet impact is directly through the vest to the sternum and then through the skeleton to the rest of the body. Thus, any parameters that affect the components in this pathway were essential to the model. This included the muscles, their geometries, material properties, and viscosity, as well as the Young's modulus of the sternochondral cartilage and the bones themselves.				
14. SUBJECT TERMS Finite Element Analysis, Human Thorax Model, Impact Analysis			15. NUMBER OF PAGES 134	
			16. PRICE CODE	
17. SECURITY CLASSIFICATION OF REPORT Unclassified	18. SECURITY CLASSIFICATION OF THIS PAGE Unclassified	19. SECURITY CLASSIFICATION OF ABSTRACT Unclassified	20. LIMITATION OF ABSTRACT UL	

NSN 7540-01-280-5500

Standard Form 298 (Rev. 2-89)
Prescribed by ANSI Std. Z39-18 298-102

Approved for public release; distribution is unlimited

**IMPACT ANALYSIS OF A BIOMECHANICAL MODEL OF THE HUMAN
THORAX**

Johannes E. Jolly
Ensign, United States Navy Reserve
B.S.E. Biomedical Engineering, Tulane University, 1999

Submitted in partial fulfillment of the
requirements for the degree of

MASTER OF SCIENCE IN PHYSICS


from the

**NAVAL POSTGRADUATE SCHOOL
June 2000**


Author:


Johannes E. Jolly

Approved by:


Young W. Kwon, Thesis Advisor


Steven R. Baker, Thesis Co-Advisor


William Maier, Chairman
Department of Physics

ABSTRACT

The biomechanical response of a finite element model of the human thorax and a protective body armor system was studied under impact loading from a projectile. The objective of the study was to create a viable finite element model of the human thorax. This objective was accomplished through the construction of a three-dimensional finite element model in DYNA3D, a finite element analysis program. The model was validated by comparing the results of tests of body armor systems conducted on cadavers to results obtained from finite element analysis. A parametric study was undertaken to determine the essential components of the model. The results from this investigation determined that the path of force propagation from a body armor system to the thorax upon bullet impact is directly through the vest to the sternum and then through the skeleton to the rest of the body. Thus, any parameters that affect the components in this pathway were essential to the model. This included the muscles, their geometries, material properties, and viscosity, as well as the Young's modulus of the sternochondral cartilage and the bones themselves.

TABLE OF CONTENTS

I.	INTRODUCTION	1
II.	BACKGROUND	3
A.	FINITE ELEMENT ANALYSIS	3
1.	Introduction to Finite Element Analysis	3
2.	History of Finite Element Analysis.....	3
3.	How the Method Works.....	5
4.	Range of Applications.....	9
B.	PROPERTIES OF BONE.....	10
C.	PROPERTIES OF CARTILAGE	17
D.	ANATOMY OF THORAX	19
1.	Spine	20
2.	Ribs	24
3.	Sternum	26
4.	Costal Cartilage.....	27
E.	BODY ARMOR.....	28
1.	A History of Body Armor	28
2.	Armor Classification.....	29
3.	Classification Requirements:	33
a.	Wet Testing.....	33
b.	Angle Shots.....	34

c.	Performance Testing	34
d.	V50 Testing.....	36
4.	Body Armor Construction.....	37
a.	Methods of Construction.....	39
b.	Materials Used	39
F.	LITERATURE SURVEY	41
III.	FINITE ELEMENT MODEL	45
A.	HUMAN THORACIC BODY MODEL	45
1.	Ribs	45
2.	Spine	46
3.	Sternum.....	48
4.	Muscle.....	49
5.	Cartilage.....	50
B.	BODY ARMOR.....	52
C.	INTERFACE ELEMENTS.....	53
D.	PROJECTILE	54
E.	BOUNDARY CONDITIONS	55
F.	ANALYSIS CODE.....	56
IV.	RESULTS AND DISCUSSION	57
A.	VALIDATION STUDY	58
1.	CBA Plate, Kevlar Vest, and NATO 7.62mm M80 Ball Round ..	58
2.	Kevlar Vest and NATO 9mm Round.....	64

B.	PARAMETRIC STUDY	70
V.	CONCLUSIONS/RECOMMENDATIONS.....	85
A.	CONCLUSIONS.....	85
B.	RECOMMENDATIONS.....	86
	LIST OF REFERENCES.....	89
	APPENDIX A: PARAMETRIC STUDY RESULTS	91
	APPENDIX B: VISCOELASTIC SOLIDS.....	107
	INITIAL DISTRIBUTION LIST	113

LIST OF FIGURES

Figure 1: Discretization of a Tapered Rod. From Ref. [2].....	5
Figure 2: Discretization of a Plate Member. From Ref. [2].....	6
Figure 3: Elements having Shape Distortions that Tend to Promote Poor Results. From Ref. [2].....	8
Figure 4: Eight Noded Brick Element. From Ref. [2].	9
Figure 5: Twenty-Noded Brick Element. From Ref. [5].	9
Figure 6: Human Skeleton. From Ref. [7].	11
Figure 7: Long Bone. From Ref. [6].	12
Figure 8: Cross-section of Compact Bone. From Ref. [7].	14
Figure 9: Basic Structure of Compact Bone. Original from Ham (1969). From Ref. [6].	15
Figure 10: Stress-Strain Curves of Human Femur. Original From Evans (1969). From Ref. [6].	16
Figure 11: Sternum and Costal Cartilages. From Ref. [7].	20
Figure 12: Vertebral Column. From Ref. [7].	21
Figure 13: Lumbar Vertebra. From Ref. [7].	21
Figure 14: Cervical Vertebra. From Ref. [7].	21
Figure 15: Thoracic Vertebra (Superior and Lateral Aspects). From Ref. [7].	23
Figure 16: Ninth, Tenth, and Eleventh Vertebrae. From Ref. [7].	23

Figure 17: (a) Fifth Rib, Inferior Aspect; (b) Fifth Rib, Posterior Aspect; (c) First Rib. From Ref. [7].	25
Figure 18: Posterior Aspect of the Sternum. From Ref. [8]	27
Figure 19: Range Set-up for Test Firings. From Ref. [12].	35
Figure 20: Impact Locations for NIJ Testing. From Ref. [12].	35
Figure 21: Plot of Sternum, Ribs, Spine, and Cartilage	46
Figure 22: Medial View of the Ribs and Spine	48
Figure 23: Sternum Shape in Thorax Model	49
Figure 24: Muscle as Constructed in Thorax Model	50
Figure 25: Articular Cartilage Connecting Sternum and Ribs	51
Figure 26: Depiction of Kevlar Vest Overlaying Muscle	53
Figure 27: Medial View of CBA Plate and Kevlar Vest	55
Figure 28: Sternum Acceleration (CBA Plate & Kevlar). Experimental Data (Exp. (#801)) versus DYNA3D Analysis (FEA). After Ref. [13].	59
Figure 29: Sternum Velocity (CBA Plate & Kevlar). Experimental Data (Exp. (#801)) versus DYNA3D Analysis (FEA). After Ref. [13].	61
Figure 30: Sternum Displacements (CBA Plate & Kevlar). Experimental Data (Exp. (#801)) versus DYNA3D Analysis (FEA). After Ref. [13].	61
Figure 31: Spinal Acceleration (CBA Plate & Kevlar). Experimental Data (Exp. (#801)) versus DYNA3D Analysis (FEA). After Ref. [13].	63
Figure 32: Spinal Velocity (CBA Plate & Kevlar). Experimental Data (Exp. (#801)) versus DYNA3D Analysis (FEA). After Ref. [13].	63

Figure 33: Spinal Displacement (CBA Plate & Kevlar). Experimental Data (Exp. (#801)) versus DYNA3D Analysis (FEA). After Ref. [13].....	64
Figure 34: Sternum Acceleration (Kevlar only). Experimental Data (Exp. (#678)) versus DYNA3D Analysis (FEA). After Ref. [13].....	67
Figure 35: Sternum Velocity (Kevlar only). Experimental Data (Exp. (#678)) versus DYNA3D Analysis (FEA). After Ref. [13].....	67
Figure 36: Sternum Displacements (Kevlar only). Experimental Data (Exp. (#678)) versus DYNA3D Analysis (FEA). After Ref. [13].....	68
Figure 37: Spinal Acceleration (Kevlar only). Experimental Data (Exp. (#678)) versus DYNA3D Analysis (FEA). After Ref. [13].....	68
Figure 38: Spinal Velocity (Kevlar only). Experimental Data (Exp. (#678)) versus DYNA3D Analysis (FEA). After Ref. [13].....	69
Figure 39: Spinal Displacement (Kevlar only). Experimental Data (Exp. (#678)) versus DYNA3D Analysis (FEA). After Ref. [13].....	69
Figure 40: Sternum Acceleration. Graphs of Experimental Data (Exp. (#801)), DYNA3D Results for Model without Muscle (FEA), and DYNA3D Results from First Validation Study (See Section A-1). After Ref. [13].....	71
Figure 41: Spinal Acceleration. Graphs of Experimental Data (Exp. (#801)), DYNA3D Results for Model without Muscle (FEA), and DYNA3D Results from First Validation Study (See Section A-1). After Ref. [13].....	72

Figure 42: Sternum Acceleration. Graphs of Experimental Data (Exp. (#801)), DYNA3D Results for Model without Dampers (FEA), and DYNA3D Results from First Validation Study (See Section A-1). After Ref. [13].....	73
Figure 43: Spinal Acceleration. Graphs of Experimental Data (Exp. (#801)), DYNA3D Results for Model without Dampers (FEA), and DYNA3D Results from First Validation Study (See Section A-1). After Ref. [13].....	74
Figure 44: Sternum Acceleration. Graphs of Experimental Data (Exp. (#801)), DYNA3D Results for Model with Muscle Young's Modulus increased by five times (FEA), and DYNA3D Results from First Validation Study (See Section A-1). After Ref. [13].....	75
Figure 45: Spinal Acceleration. Graphs of Experimental Data (Exp. (#801)), DYNA3D Results for Model with Muscle Young's Modulus increased by five times (FEA), and DYNA3D Results from First Validation Study (See Section A-1). After Ref. [13].....	76
Figure 46: Sternum Acceleration. Graphs of Experimental Data (Exp. (#801)), DYNA3D Results for Model with Sternal Cartilage Young's Modulus increased by ten times (FEA), and DYNA3D Results from First Validation Study (See Section A-1). After Ref. [13].	77
Figure 47: Spinal Acceleration. Graphs of Experimental Data (Exp. (#801)), DYNA3D Results for Model with Sternal Cartilage Young's Modulus increased by ten times (FEA), and DYNA3D Results from First Validation Study (See Section A-1). After Ref. [13].	77

Figure 48: Sternum Acceleration. Graphs of Experimental Data (Exp. (#801)), DYNA3D Results for Model without Contact Elements (FEA), and DYNA3D Results from First Validation Study (See Section A-1). After Ref. [13].....	79
Figure 49: Spinal Acceleration. Graphs of Experimental Data (Exp. (#801)), DYNA3D Results for Model without Contact Elements (FEA), and DYNA3D Results from First Validation Study (See Section A-1). After Ref. [13].....	79
Figure 50: Sternum Acceleration. Graphs of Experimental Data (Exp. (#801)), DYNA3D Results for Model with Kevlar Density increased five times (FEA), and DYNA3D Results from First Validation Study (See Section A-1). After Ref. [13].....	81
Figure 51: Spinal Acceleration. Graphs of Experimental Data (Exp. (#801)), DYNA3D Results for Model with Kevlar Density increased five times (FEA), and DYNA3D Results from First Validation Study (See Section A-1). After Ref. [13].....	81
Figure 52: Sternum Acceleration. Graphs of Experimental Data (Exp. (#801)), DYNA3D Results for Model with CBA Plate Density increased five times (FEA), and DYNA3D Results from First Validation Study (See Section A-1). After Ref. [13].....	82
Figure 53: Spinal Acceleration. Graphs of Experimental Data (Exp. (#801)), DYNA3D Results for Model with CBA Plate Density increased five times (FEA), and DYNA3D Results from First Validation Study (See Section A-1). After Ref. [13].....	82

Figure 54: Sternum Acceleration. Graphs of Experimental Data (Exp. (#801)), DYNA3D Results for Model with Thorax Dimensions increased 25% (FEA), and DYNA3D Results from First Validation Study (See Section A-1). After Ref. [13].....	84
Figure 55: Spinal Acceleration. Graphs of Experimental Data (Exp. (#801)), DYNA3D Results for Model with Thorax Dimensions increased 25% (FEA), and DYNA3D Results from First Validation Study (See Section A-1). After Ref. [13].....	84
Figure 56: Models of Viscoelastic Solids. From Ref. [24].....	107
Figure 57: Model of DYNA3D Viscoelastic Solid.....	108

LIST OF TABLES

Table 1: NIJ Body Armor Classification and Testing Summary. From Ref. [12].....	32
---	----

ACKNOWLEDGMENTS

The author would like to acknowledge the financial support of the Headquarters, U.S. Army Soldier & Biological Chemical Command, Soldier Systems Center for funding this project.

I would also like to express my sincerest appreciation to Professors Young W. Kwon and Steven R. Baker for their dedicated support throughout this endeavor. Their wisdom and technical guidance significantly enhanced my education at the Naval Postgraduate School.

I. INTRODUCTION

Since the early twentieth century, the United States government has conducted research in the field of protective body armor systems. Initial experiments with silk and steel proved either to provide an inadequate level of protection or were too unwieldy as a body armor system for soldiers. Recent advances in the field of material science have lead to the advent of such polymers as Kevlar and Spectra, and ceramics, such as boron carbide, that are incorporated into modern body armor systems. Although these bulletproof vests are resistant to bullet penetrations, the forces that are imparted to the body are still significant and potentially lethal.

The objective of research described in this thesis is to create a viable three-dimensional finite element model of the human thorax (including ribs, sternum, vertebral column, cartilages, and major musculature) that would predict the response of a bullet impact on a body armor system. Validation of the model was conducted by comparing the finite element analysis (FEA) results to those obtained during bullet impact analyses of body armor systems on cadavers. Upon validation, the model was subjected to a parametric study to determine its essential components.

With the model developed, it is possible to study the effects of different body armor systems, different projectiles with various velocities, and the thoracic dimensions of individuals, on the response of the thorax. This allows for realistic experimentation on new body armor systems for the United States government without the time and cost involved in cadaveric studies.

THIS PAGE INTENTIONALLY LEFT BLANK

II. BACKGROUND

A. FINITE ELEMENT ANALYSIS

1. Introduction to Finite Element Analysis

Finite Element Analysis (FEA) or the Finite Element Method (FEM) has developed from its infancy in the late 1940s into the mature computational science that it has become today. In its earliest days, the scope and the depth of problems analyzed by this particular method were limited by the size of the matrices created. However, today, with the enormous amounts of computing power available, areas such as structural mechanics, heat transfer, electromagnetics, fluid flow, orthopedic implant design, and tissue growth can all be adequately modeled and analyzed. It is becoming an integral part of the prototyping of new designs. By allowing engineers to model a design and test it in a computer environment, savings are realized in both time and money.

2. History of Finite Element Analysis

The ideas behind the finite element methods were first mentioned in 1943, when a mathematician, R. Courant, first proposed the idea of taking a continuum problem, breaking it down into triangular regions, and solving the problem in each region individually with piecewise approximations. Unfortunately, his ideas were not expounded upon until 1950 due to the fact that the computing power necessary to actually implement these ideas did not present itself until almost a decade after Courant's paper. [Ref. 1] In a ground-breaking paper published in 1956, Turner, Clough, Martin, and Topp established the original method, developed out of a problem originating in the

1930s. A structural engineer had been presented with the issue of how best to solve for the component stresses of a loaded truss. The issue was relatively straightforward and followed simple statics. Yet, this was only for the case of a finite number of interconnections. The question arose about how to deal with the problem if a plate replaced the truss. In this instance, an infinite number of interconnection points would be present. Hrenikoff proposed a solution by dividing the plate into elements or structural sections connected at a finite number of nodes. This allowed the problem to be resolved by conventional means and it planted the seeds for the finite element method. In fact, this idea was further developed and a solution presented in the paper by Turner, Clough, Martin, and Topp. It was in an extension of this work by Clough in 1960 where the name 'finite element method' first appeared.

Consequent developments in the field of finite element analysis have resulted in continued refinements to the original method. Additionally, the field has grown to encompass various disciplines such as thermodynamics, electromagnetics, and biomechanics. The advent and continued advances in computers have also significantly affected the implementation of finite element analysis. Today, numerous computer programs have been developed to help make the different steps of the finite element method easier and more automated. Computer programs can now take information from computer-aided design (CAD) and computer-aided manufacturing (CAM) programs and use this as a basis for the finite element model, saving time and reducing errors.

3. How the Method Works

In a continuum problem, the variables to be analyzed possess an infinite number of values because each is a function of a particular point in that region or body. Consequently, there are an infinite number of unknowns. By discretizing the region into a collection of finite elements, the infinite number of unknowns is reduced to a finite number. Solving for the values at nodes, or the intersection of these elements, gives a cloud of data about the region or body. Approximation, or interpolation, functions can then take the particular value at a specific node or series of nodes and average it across each element. This method allows a seemingly “impossible” problem to be broken down into a more manageable one. Now, the behavior of the field variable can be approximately described for the entire region. Figure 1 is an example of discretizing a given complex domain into elements. Note that u is the deformation in the x direction due to the applied force, P .

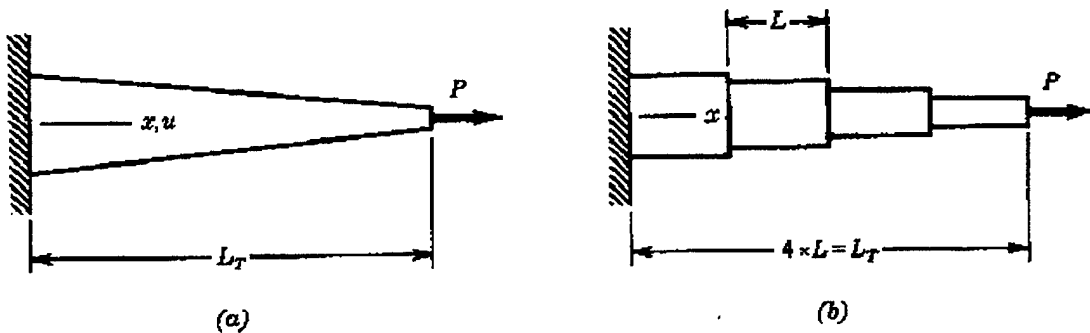


Figure 1: Discretization of a Tapered Rod. From Ref. [2].

The accuracy of the data returned by the method is subject not only to the number of nodes and elements used, but also to the particular interpolation functions that are

chosen. The determination of which functions to use will depend on the kind of element selected. Another important determination in the selection of the interpolation function is to ensure that the data will be continuous across element boundaries. Figure 2 demonstrates the potential discretization of a complex geometry and the resultant forces applied after creation of the finite element model. In this figure, u and v are the deformations in the x and y direction, respectively.

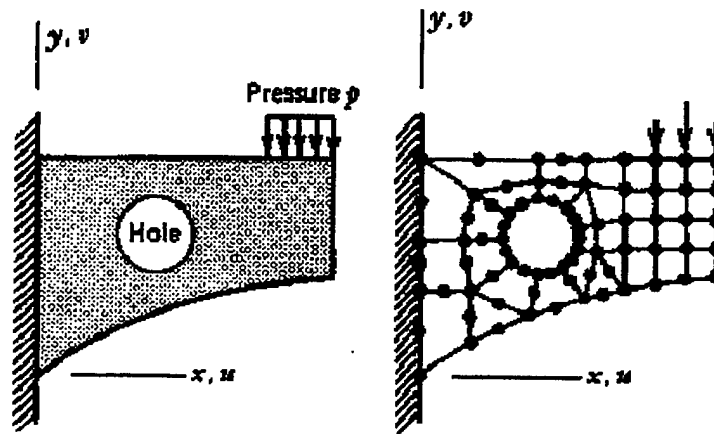


Figure 2: Discretization of a Plate Member. From Ref. [2].

Finite element analysis relies on several different approaches to solving a given problem. These include the direct approach, the variational method, and the weighted residuals method. The direct approach is a relatively simple method, based on the direct stiffness method of structural analysis, with the limitation that it can only be used on elementary problems. By understanding the points at which various beams intersect and the angle of their intersection, their transmission of forces from one to another can be calculated. By breaking down the complex structures into simpler elements, the “force-

deflection,” or stiffness, characteristics of that particular element can be determined.

Matrices can be constructed that represent the stiffness of each individual member. By combining these matrices, the stiffness for the entire structure can be determined. This method of calculating the effects of loads on framed structures became known as the direct stiffness method and resulted in the first approach to solutions in finite element analysis. [Ref. 3]

The variational approach to representing element properties relies on the calculus of variations and involves extremizing a functional. These functionals are dependent on the type of problem being studied. For example, in solid mechanics, the functional is the stationary potential energy. This method allows finite element analysis to extend beyond the limit of simple elements in structural mechanics and become incorporated into other fields. It also allows for the use of sophisticated element shapes, unlike the simple shapes required by the direct approach. [Ref. 4]

The most versatile of the approaches is the weighted residuals method. It can be used in cases where no functional can be defined, such as in nonstructural element fields like heat transfer and fluid mechanics. This method relies on a set of established governing equations defined for the problem, without requiring a variational function. This allows the finite element method to be utilized in different scientific fields than those opened up by either the direct or variational approaches. [Ref. 4]

The basic steps taken to perform a finite element analysis are the same regardless of the approach being used. The first step is to develop the model for the analysis. This includes creating the geometric representation of the object, defining the domain and

boundary conditions, defining material properties for the model, and apply the loads to be studied. Included in this step are any model idealizations that can be specified to simplify the model. This may include modeling only one side of a symmetrical object under a symmetrical load or renumbering nodes to minimize bandwidth of the required matrices. Due to the computer- and time-intensive nature of finite element analysis, any simplifications can significantly reduce computation costs.

The next step in the finite element method is to discretize the model and domain into finite elements and ensure that they are properly connected. This is a step of compromise. As the model is being discretized, the size, shape, and number of elements created becomes important. Figures 3, 4, and 5 show examples of elements that should and should not be used in the discretization. These parameters will determine the accuracy that is returned. If the elements created are too large and do not adequately model the region or body being analyzed, the data returned will be inaccurate. However, if the elements created are too small, the time and number of calculations required to arrive at a solution will be too large.

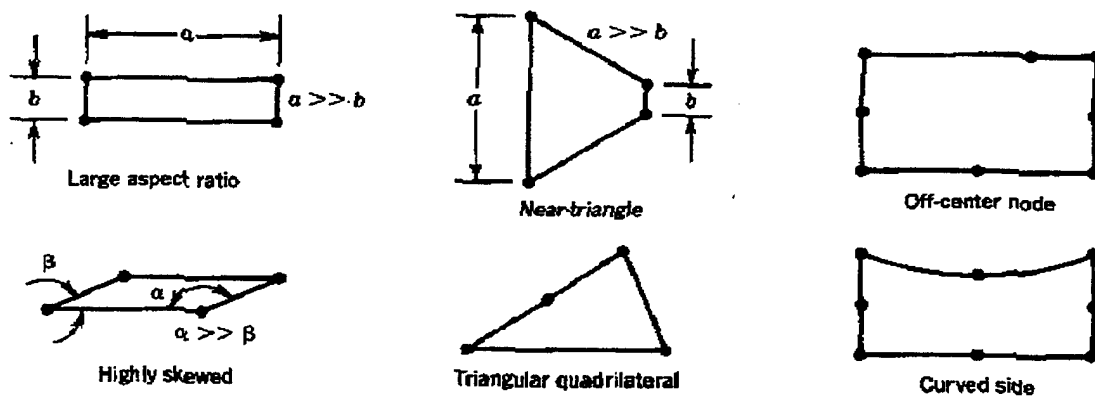


Figure 3: Elements having Shape Distortions that Tend to Promote Poor Results. From Ref. [2].

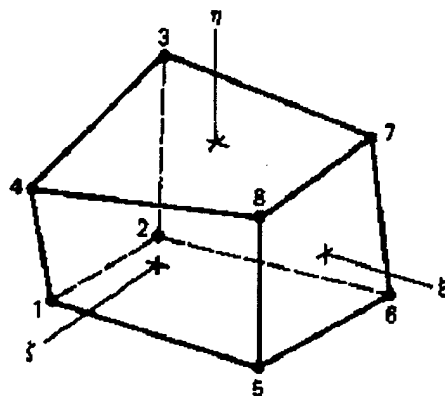


Figure 4: Eight Noded Brick Element.
From Ref. [2].

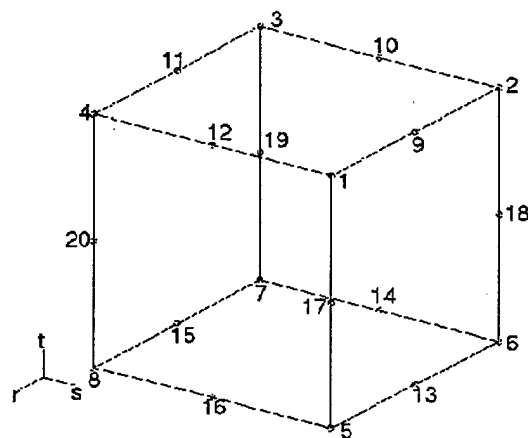


Figure 5: Twenty-Noded Brick Element.
From Ref. [5].

The next step is to perform the analysis itself. This is the application of one of the various methods, direct, variational, or weighted residuals, to the finite element model.

The final step is to verify the accuracy of the results and conduct any post-processing. The accuracy can be checked by several methods, including refining the model to check for convergence, and parametric studies. Post-processing, on the other hand, allows for accurate and complete documentation of the analysis results. This includes creating a graphical representation of the problem and the results so that the data are easily accessed and pertinent information can be easily extracted.

4. Range of Applications

There are three basic categories into which the applications of the finite element method fall. The first is the time-independent, or static analysis, problem. This contains the majority of the current uses for finite element analysis. The solutions are all created under steady-state conditions.

The second category into which finite element analysis applications fall is the eigenvalue problem. These problems are an investigation of the long-term state of a system. In addition, this type of problem can determine the natural frequencies and modes of vibrations in areas such as solid and fluid mechanics. These types of applications also include such as the stability of structures and the stability of laminar flows.

The final category is time-dependent or propagation problems. These problems must also consider the variable of time and its effect on a system. Those studying continuum mechanics are most interested in this area of application. It is these dynamic problems that were the focus of this study.

The finite element method is being incorporated into almost every field of engineering. Whereas the original users of the method were mostly civil, mechanical, or aerospace engineers, the finite element method has spread to various disciplines such as heat transfer, fluid mechanics, electromagnetics, and biomechanics. This widespread use illustrates the power and opportunities in the finite element method.

B. PROPERTIES OF BONE

The skeleton consists of 200 bones of various shapes and sizes as depicted in Figure 6 below. Bone consists primarily of calcium and phosphorous. Included in the chemical composition are traces of magnesium, fluorine, chlorine, and iron. Bones, a living tissue, are grown by the expansion of an epiphyseal plate. As the plate expands, the cartilaginous growth plate beneath it is subsequently calcified and turned into

compact bone. For flat bones, it is the calcification of membranous tissues that leads to the construction of the bone. Surrounding the bone, except at the points of articulation, is a thin layer called the periosteum. The interior layer of the periosteum contains cells that provide enlargement and remodeling of a growing long bone. After the bone has matured, the inner layer becomes primarily a network of capillary blood vessels and the outer layer becomes fibrous. However, if subject to injury, the inner layer of the periosteum can once again become osteogenic. [Refs. 6 & 7]

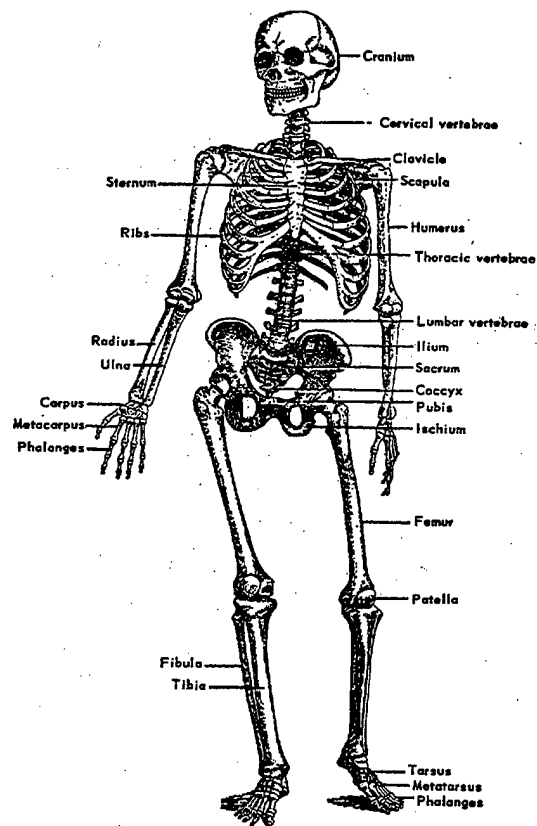


Figure 6: Human Skeleton. From Ref. [7].

Bones can be classified in four broad categories. These are long, short, flat, and irregular. Long bones, as illustrated in Figure 7 below, are the primary members of the limbs, where they are used to support the weight of the trunk and to provide the foundation for locomotion. These bones consist of a diaphysis and two epiphyses. The diaphysis is a tube of compact bone with the greatest thickness at the middle of the bone. Inside the tube is a thin layer of spongy tissue (cancellous bone) with a medullary canal running the length of the bone. The medullary canal is the location of the bone marrow. The extremities consist of primarily cancellous bone with a thin shell of compact bone. In addition, the epiphyses have a large surface area to provide room for muscle attachments and articulations with neighboring bones.

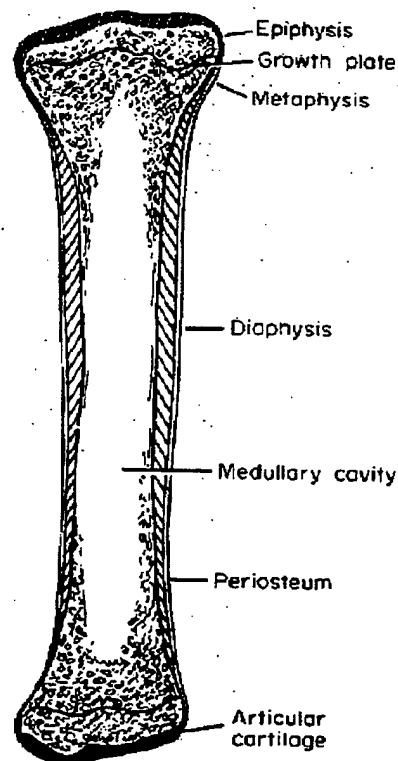


Figure 7: Long Bone. From Ref. [6].

The short bones provide strength and compactness while allowing for small movements. They are primarily found in the hands and feet (carpus and tarsus). Except for a thin shell of compact bone at the surface, they consist primarily of spongy bone.

The ribs, sternum, and bones of the cranium and face characterize the flat bones. Their primary purpose is for broad muscle attachments or protection. These bones consist of two thin layers of compact bone with spongy bone in the interior.

The irregular bones are those that do not fit into any of the previous categories. However, they do share the same general composition of compact bone on the exterior and spongy bone on the interior.

Bone is not a homogenous material. It is a composite of Haversian units, also known as osteons. The center of each osteon is an artery or a vein, called the Haversian canal, with transverse Volkmann's canals connecting adjacent units. The inorganic materials, such as calcium and phosphorous in a form called hydroxyapatite, make up two-thirds of the weight of bone. The remaining weight is primarily in the form of organic collagen fibers. These fibers can be either in parallel packages called lamellae or in a tangled web, dependent upon the type of bone. Within each osteon, the lamellae are arranged in approximately six to eight concentric circles about the Haversian canal. However, in the interstitial space between Haversian units, the lamellae are primarily parallel to the surface of the bone. Lacunae are small cavities equally spaced between lamellae. These cavities radiate canaliculi and connect with the Haversian canals. This network penetrates the bone matrix allowing for the transmittal of nutrients and removal

of wastes from the cells of the bone. A cross-section of a long bone is depicted in figures 8 and 9 below.

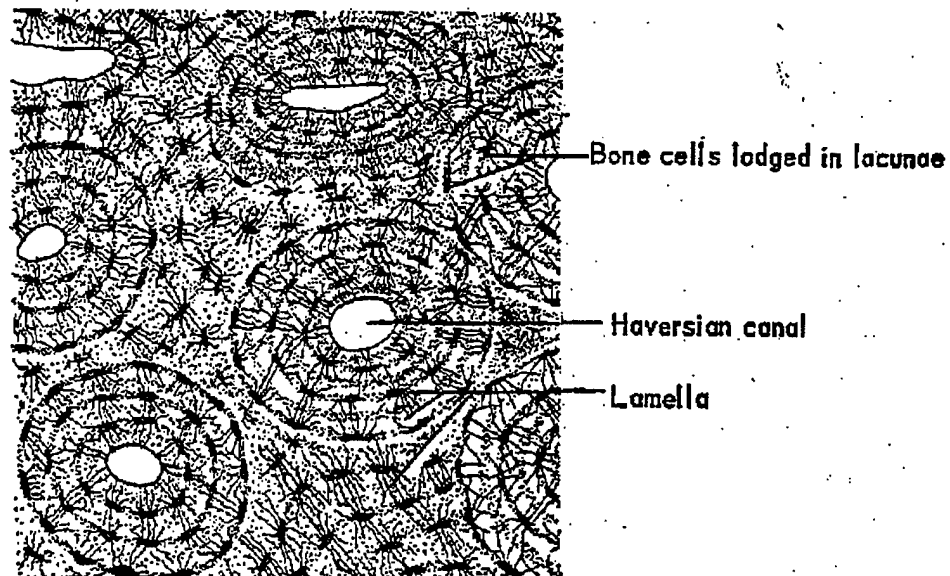


Figure 8: Cross-section of Compact Bone. From Ref. [7].

The primary cells of bone are the osteoblasts, osteoclasts, and osteocytes. The osteoblasts are found in a layer adjacent to the periosteum. They are primarily responsible for the formation of bone tissue. Osteoclasts are located at sites of bone reabsorption and are primarily responsible with dissolving bone for remodeling. Osteocytes are the mature, permanent bone cells of osseous tissue and differentiate from the osteoblasts.

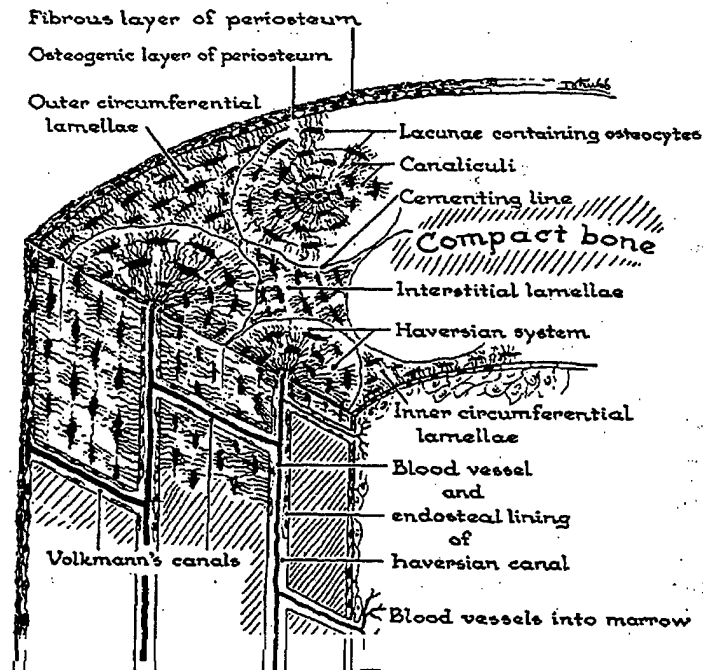


Figure 9: Basic Structure of Compact Bone. Original from Ham (1969). From Ref. [6].

The mechanical properties of bone are dependent upon its structure as a composite of minerals and collagen. However, bone's strength is higher than either of its constituent parts. This is due to the softer component (collagen) preventing the stiffer material (hydroxyapatite) from brittle cracking and the stiff component preventing the softer one from yielding.

Stress-strain curves have been obtained from placing human femurs under tension loads. As such, it has been determined that dry bone is brittle and fails at a strain of 0.4%. On the other hand, wet bone fails at 1.2% strain. Due to the initial linear nature of the stress-strain curves, it is possible to determine a Young's modulus for bone. It is important to note that the Young's modulus depends upon the load type and rate applied to the bone. Due to its anisotropic nature, the Young's modulus for a femur under

tension is approximately three times higher than that of a femur under compression. Stress-strain curves, such as those depicted below in Figure 10, can also be utilized to determine the ultimate tensile strength, the yield point, and the strain energy of bone. It is important to note that these tests were performed for the femur, which consists of both cortical and cancellous bone. (Cancellous bone tends to fail at 75% strain, whereas cortical fails at 2% strain.) [Ref. 6]

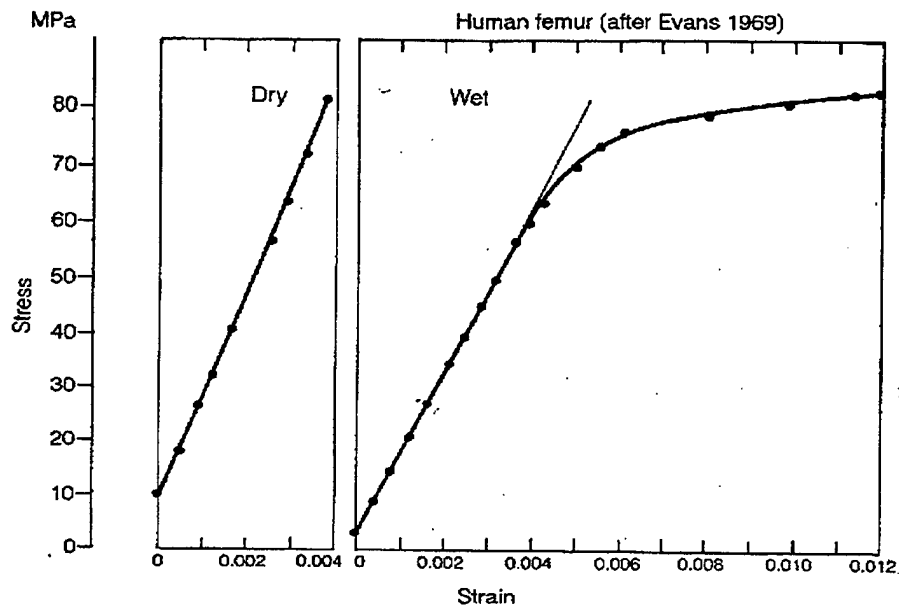


Figure 10: Stress-Strain Curves of Human Femur. Original From Evans (1969). From Ref. [6].

Bone exhibits both brittle and ductile behaviors. Additionally, due to its anisotropy, the behavior of bone subjected to applied forces will vary dependent upon the mechanical properties, the geometry, the loading modes, the loading rate, and the frequency of load application. Other important considerations in the calculation of the mechanical properties of bone are the sex and age of the subject, the location of the bone,

the orientation of the load, the strain rate, and whether the bone is wet or dry. Due to the uniqueness of each of these parameters for an individual, it is impossible to develop an average value for humans in general.

C. PROPERTIES OF CARTILAGE

Cartilage is found in various sites around the body, including the ears, nostrils, joints, and in the thorax. All three types of cartilage share the same basic elements: cells, intercellular matrix, and system of fibers. The varieties include hyaline cartilage, fibrocartilage, or fibroelastic cartilage, dependent upon the matrix in which the cartilage cells (chondrocytes) are imbedded. Cartilage can also be classified according to its position in the body. In this case, cartilage can be articular, interarticular, costal, or membraniform. [Ref. 8]

Hyaline cartilage covers the ends of bones within joints, acting as a shock buffer and providing smooth surfaces for articulation. Except at points of articulation, it is covered by a membrane that provides the chondrocytes with nutritive fluids. Articular, costal, and temporary cartilage are all of the hyaline variety. The only difference between them is the size and shape of the chondrocytes and the exact arrangement of the matrix. Articular cartilage has a finely granular matrix. It grows in response to the location of the largest stress. As such, it will be thickest at a tubercle or other protrusion that receives a majority of the force on a joint. Costal cartilage has large cells and fibrous striations in the matrix. For all three types of cartilage, calcification can occur. For the

temporary cartilage, it is this calcification that allows for the cartilaginous skeleton of the human fetus to develop into the bony skeleton. [Ref. 7]

Fibrocartilage is found in the intervertebral discs, the semilunar cartilages of the knee joint, and the cartilage of the symphysis pubis. It consists of a mixture of white fibrous tissue and cartilaginous tissue in various proportions. The fibrous tissue allows for flexibility and toughness, whereas the cartilaginous tissue provides elasticity. In the case of the intervertebral disc, this allows for shock absorption while still maintaining flexibility in the spine. The fibrocartilage can be of several varieties, including interarticular, connecting, circumferential, or stratiform, depending upon appearance and location. [Ref. 7]

The least pervasive type of cartilage is fibroelastic cartilage. It is found in certain small cartilages of the larynx, the epiglottis, and the ear. Similar to the other types of cartilage, it is differentiated by the network of tangled yellow elastic fibers that permeate its matrix. [Ref. 7]

Cartilage is a rather porous material, allowing for the movement of fluids in and out of the tissue. The physical structure responsible for this fluid absorption and discharge is chains of proteoglycans, large protein-polysaccharide molecules, which create the intracellular matrix of cartilage. Additionally, friction between these chains is responsible for the creep and stress relaxation that characterize the viscoelastic properties of cartilage. [Ref. 9] For example, upon indentation, cartilage will have an immediate recovery followed by a time-dependent one. This flexibility is what allows the thorax to change shape as the lung inhale and exhale. Additionally, this property allows cartilage

to have an extremely low coefficient of friction while still maintaining a long lifetime. It is thought that this occurs due to the presence of the fluids in the extracellular matrix. As the fluid is squeezed out, the coefficient of friction increases. Thus, joints, such as the synovial joints, are so effective because the time required for the fluids to be squeezed through the matrix is long and once the load is removed, the compressed cartilage rebounds quickly and reabsorbs the synovial fluid. This creates a unique system that is adapted for both shock absorption and lubrication of points of articulation. [Ref. 6]

D. ANATOMY OF THORAX

The human thorax consists of an osteo-cartilaginous cage to protect the primary organs of respiration and circulation. Its posterior surface consists of the twelve thoracic vertebrae and the sternum; the costal cartilages form the anterior surface. The ribs form the lateral surfaces. The upper boundary of the thorax is formed by the first thoracic vertebra, the superior of the sternum, and the first rib pair. The lower boundary of the thorax is the diaphragm which connects the twelfth thoracic vertebra, the twelfth rib pair, and the subcostal angle formed by the cartilage of the seventh, eighth, ninth, tenth, and eleventh rib pairs. A posterior view of the thorax, illustrating the sternum and costal cartilages, is depicted in Figure 11 below. [Ref. 8]

The differences between the male and female thorax are minor. On the female, the general volume is smaller than that of a male, the sternum is shorter, the superior portion of the sternum is generally in line with the lower portion of the third thoracic

vertebra rather than the lower portion of the second thoracic vertebra in males, and the upper ribs are more flexible. [Ref. 8]

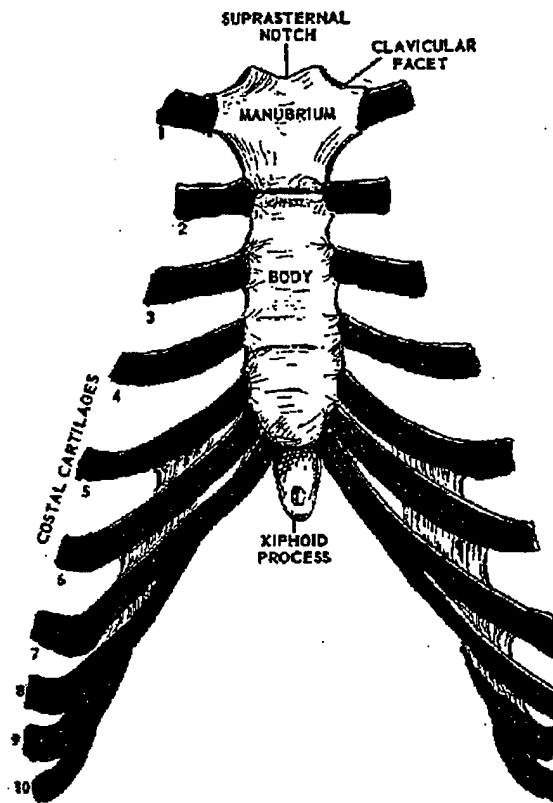


Figure 11: Sternum and Costal Cartilages. From Ref. [7].

1. Spine

In general, the spine consists of 34 vertebrae, 23 discs, and their connecting ligaments. The function of the spine is to form a strong support structure for the head and trunk, to protect the spinal cord, and to provide rigidity for the suspension of the limbs. There are three major regions: cervical vertebrae (7), thoracic vertebrae (12), and lumbar vertebrae (5). The additional vertebrae are included as either sacral vertebrae (5), which are fused together to form the sacrum, or coccygeal vertebrae (5), which are fused

together to form the coccyx. These regions, in turn, provide a method for naming each vertebra. The vertebrae in each region are labeled with a C, a T, or an L, depending upon whether they are in the cervical, thoracic, or lumbar region. Additionally, numbers are assigned, with one being the most superior vertebra in that particular region. Below, in Figures 12, 13, and 14, are illustrations of the spinal column, a lumbar vertebra, and a cervical vertebra, respectively.

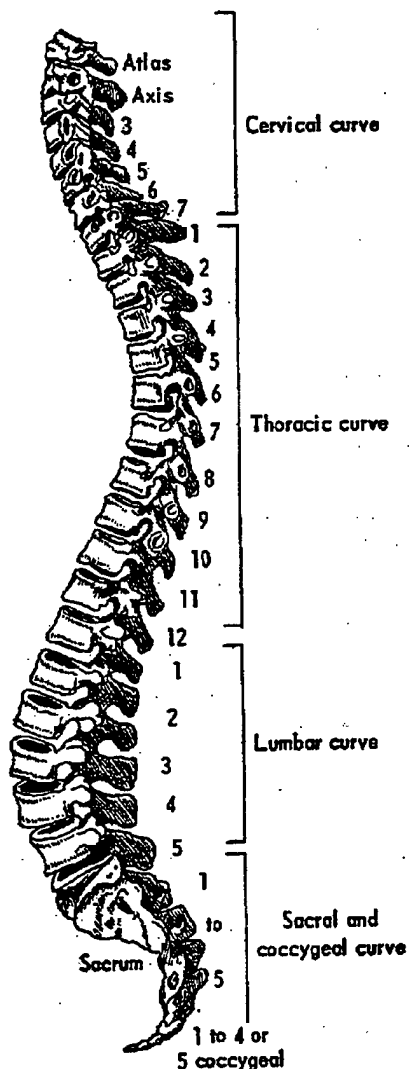


Figure 12: Vertebral Column. From Ref. [7].

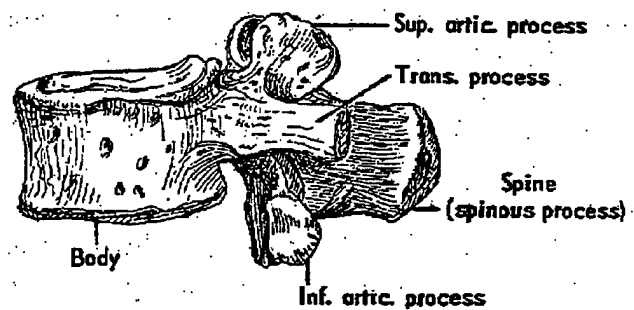


Figure 13: Lumbar Vertebra. From Ref. [7].

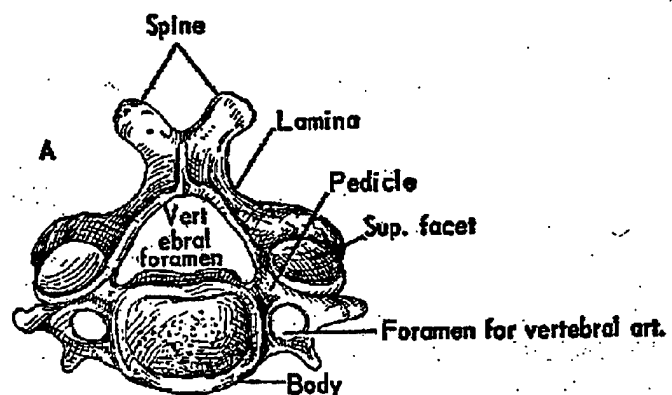


Figure 14: Cervical Vertebra. From Ref. [7].

A typical vertebra consists of a body and a vertebral arch, as depicted in Figure 15. The body is a thick disclike mass of cancellous bone with a thin covering of compact bone, situated anteriorly to the spinal cord. The body is convex horizontally in front and concave behind to form one side of the canal for the spinal cord. The vertebral bodies are stacked one on top of another, with intervening discs of cartilage, to form the vertebral column, as in Figure 16. The vertebral arch is located posteriorly of the body and closes off a space between the body and the arch called the vertebral foramen. The vertical alignment of this foramen creates the spinal canal and is the location of the spinal cord. The vertebral arch consists of two pedicles, two laminae, a spinous process, two transverse processes and four articular processes to interact with the neighboring vertebrae. The pedicles are two angled protrusions of bone sprouting from the body in a posterior direction. The laminae extend from the pedicles and meet in the midline, posterior from the center of the vertebral body. At the point of confluence, the spinous process is born and points backwards and downwards. The spinous process articulates with the spinous process of the vertebra beneath it. This adds additional support to the vertebral column. The transverse processes protrude laterally and posteriorly from the junction of the lamina and the pedicle. The articular processes also point in this direction. They are found in two pairs, one inferior and one superior. The superior articular processes face backwards, whereas the inferior articular process facets face forwards. Thus, the superior articular process of the lower vertebrae and the inferior articular process of the upper vertebrae interact to provide lateral and medial stability to the spine. [Ref. 8]

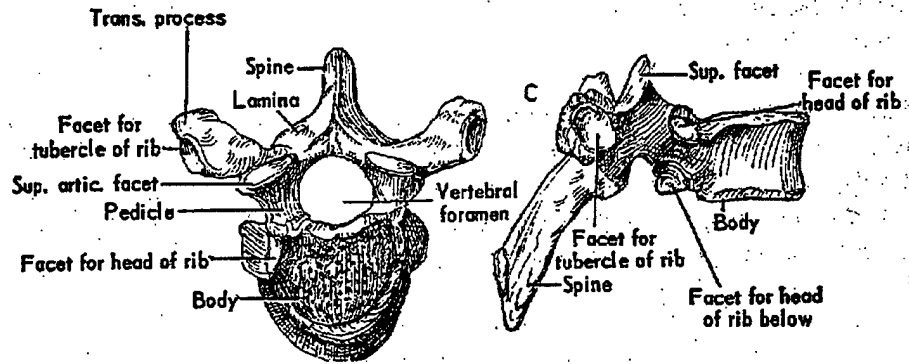


Figure 15: Thoracic Vertebra (Superior and Lateral Aspects). From Ref. [7].

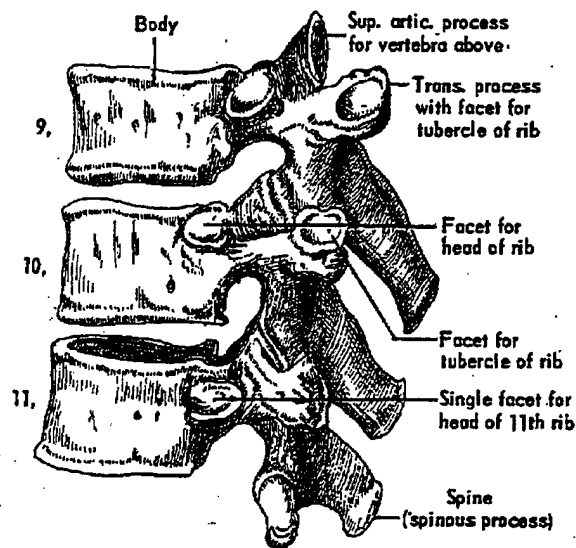


Figure 16: Ninth, Tenth, and Eleventh Vertebrae. From Ref. [7].

The ligaments of the spine can be divided into five sets, dependent on position. There are those connecting the bodies of the vertebrae, the laminae, the articular processes, the spinous processes, and those connecting the transverse processes. The most important are the interspinous ligament and the supraspinous ligament. The interspinous ligament is thin and membranous and extends from the root to the summit of the spinous processes between each vertebra. The supraspinous ligament is a strong cord

connecting the spinous processes from the seventh cervical vertebra to the sacrum. [Ref. 8]

2. Ribs

The ribs are 24 bowed bones in 12 pairs. Articulating with the thoracic vertebrae posteriorly and the sternum anteriorly, they form the framework for the thorax. They are numbered in ascending order with the most superior rib as one. This numbering corresponds to the thoracic vertebra that each rib pair articulates with as well. Ribs one through seven, as represented in Figure 17 below, are called the true ribs due to their direct connection to the sternum through costal cartilage. Ribs eight through twelve are false ribs. Ribs eight, nine, and ten share a common connection to the sternum through the subcostal angle, whereas ribs eleven and twelve are floating ribs with no connection to the sternum at all. The direction of the ribs varies as well, with the upper ones less oblique than the lower. The ribs increase in length from the first to the seventh, then they begin to decrease through the twelfth. The largest breadth of the rib is at the attachment point of the sternum. [Refs. 7 & 8]

Each rib has two extremities: the posterior (vertebral) and anterior (sternal). The connecting section is referred to as the shaft or body. The posterior section includes the head, a neck, and tuberosity. The head contains two facets for articulation with the articular surface created between the body of two adjacent vertebrae. Additionally, the head is attached to the intervertebral disc through a short ligament between the articular surfaces. The neck is the intervening region between the head and the tuberosity. It has a flattened portion for attachment of various ligaments. The articular tuberosity interacts

with the transverse process of the lower vertebrae. The shaft is thin, flat and is bowed and twisted as it proceeds from the vertebral to sternal extremity. Finally, the sharp bend both superiorly and anteriorly in the shaft is referred to as the angle. The anterior end of the rib is flattened and porous allowing for attachment via collagen anchors of the costal cartilage. [Ref. 8]

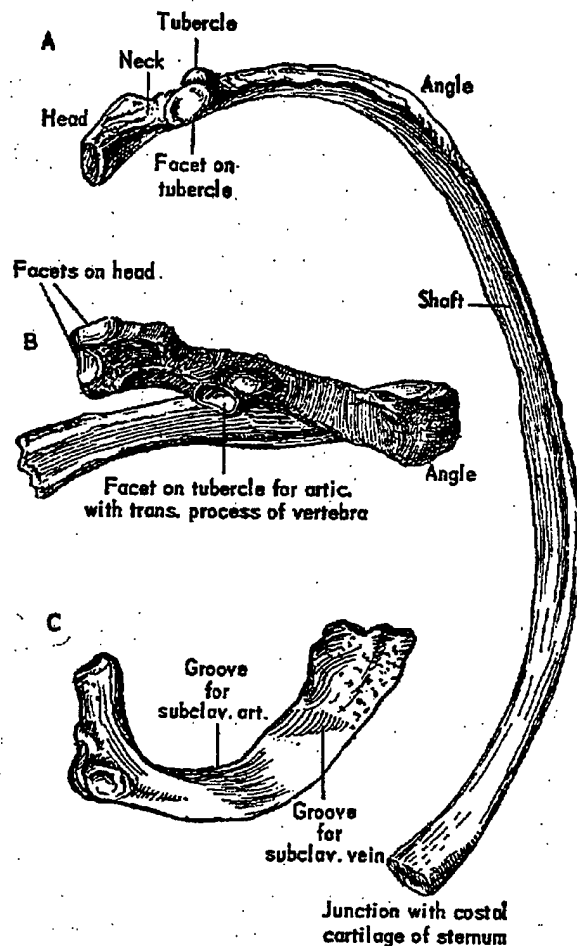


Figure 17: (a) Fifth Rib, Inferior Aspect; (b) Fifth Rib, Posterior Aspect; (c) First Rib. From Ref. [7].

The ribs are not uniform, and the first, second, tenth, eleventh, and twelfth exhibit interesting peculiarities. The first rib is the shortest and the most curved. The second

also exhibits sharp curves but is much longer than the first. The tenth rib only has one articular facet on its head. The eleventh and twelfth each have only one articular facet and they do not have a neck or tuberosity. Finally, the twelfth rib does not demonstrate an angle, whereas the angle in the eleventh rib is slight.

3. Sternum

The sternum is a flat, elongated bone situated in the median of the front of the chest. It consists of three individual portions. The upper segment is referred to as the manubrium, the middle section is called the gladiolus, and the lower, pointed section is called the xiphoid process. The sternum is slightly convex in front and concave in back. See Figure 18. The manubrium is of a triangular shape with lateral depressions for the articulation of the first costal cartilage. A notch on the inferior surface of the manubrium and a similar notch on the superior edge of the gladiolus create a depression for the articulation of the second costal cartilage. The gladiolus is relatively long and narrow. Its anterior surface is essentially flat, whereas the posterior surface is slightly concave. The lateral surface is marked with both inferior and superior notches for articulation with the seventh and second rib pairs, respectively. Included along its lateral edge are depressions for the costal cartilage of the third, fourth, fifth, and sixth rib pairs as well. The xiphoid process, also called the ensiform appendix, is the smallest of the three. It articulates with the gladiolus on its superior edge with depressions for the articulation of the seventh rib pair. [Refs. 7 & 8]

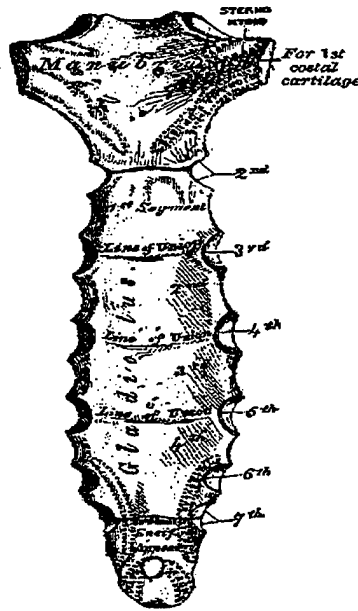


Figure 18: Posterior Aspect of the Sternum. From Ref. [8].

4. Costal Cartilage

The costal cartilages are bars of hyaline cartilage that extend the ribs forward to the connection with the sternum. Due to the mechanical properties of cartilage, this articulation significantly affects the flexibility of the thorax and its ability to absorb loads. The first seven pairs of costal cartilage directly attach ribs one through seven to the sternum. Costal cartilages eight, nine, and ten directly attach to the costal cartilage of the rib pair directly superior to it. There are also portions of costal cartilage attached to the last two rib pairs, however, these do not attach to the sternum and merely cover the anterior extremity of the bone. The posterior extremity of the costal cartilage is continuous with the osseous tissue of the rib from which it arose. The superior extremities of the second through seventh costal cartilages end in small, smooth, oval-shaped facets to articulate with the corresponding depression in the sternum. Contrarily,

the superior costal cartilage of the first rib pair is continuous with the osseous tissue of the sternum. [Ref. 6]

E. BODY ARMOR

1. A History of Body Armor

The history of body armor is as varied as the types of weaponry employed over the years. Initially, humans utilized animal skins for protective clothing and wood for shields. With the advancement of metallurgy in the Middle Ages, metal shields were developed and, consequently, the use of metal in suits of armor became widespread. However, the introduction of firearms around 1500 led to the obsolescence of these body armor systems. [Refs. 10 & 11]

The development of soft armor for protection is credited to the medieval Japanese. Creating a garment made from silk, it gave their warriors minimal protection for use in combat. However, the introduction of soft armor into the United States did not occur until the late 19th century. Relying on the same materials as the medieval Japanese had used, the military attempted the manufacture of soft armor from silk. However, the material was shown to be ineffective against the new higher velocity bullets (> 600 ft/sec) used at that time. Additionally, the cost per garment was prohibitive to widespread use.

World War I precipitated an increase in research into body armor to protect against shell fragments, but the materials were not available to create a vest with the correct protection for a reasonable weight. [Ref. 10]

The outbreak of World War II led to renewed interest in body armor. Several variations were tried, utilizing materials such as overlapping plates of steel, aluminum, or bonded fiberglass incorporated into a vest of ballistic nylon. These vests were lightweight and flexible while providing protection from shell fragments. However, the "flak jackets" did not provide adequate protection against rifle and pistol threats.

In the 1960's, the development of new fibers made the modern generation of bullet proof vest possible. Additionally, research in ceramics and composites, such as boron carbide, led to the creation of vests reliant upon a mesh of ballistic fibers while incorporating composite layers of steel or hard ceramics into their design. These vests have demonstrated their effectiveness in stopping even armor-piercing bullets. [Ref. 10]

2. Armor Classification

The National Institutes of Justice have developed a standard (NIJ Standard-0101.03) to establish six formal armor classification types, as well as a seventh special type. A table of the requirements is summarized below as Table 1. These are as follows:

Type I (.22 LR; .38 Special). For protection against .22 Long Rifle High-Velocity lead bullets, with nominal masses of 2.6 g (40 gr), impacting at a velocity of 320 m/s (1,050 ft/s) or less, and against .38 Special roundnose lead bullets, with nominal masses of 10.2 g (158 gr), impacting at a velocity of 259 m/s (850 ft/s) or less. It also provides protection against most other .25 and .32 caliber handgun rounds. [Ref. 12]

Type II-A (Lower Velocity .357 Magnum; 9mm). This armor protects against .357 Magnum jacketed soft-point bullets, with nominal masses of 10.2 g (158 gr), impacting at a velocity of 381 m/s (1,250 ft/s) or less, and against 9mm full-metal

jacketed bullets, with nominal masses of 8.0 g (124 gr), impacting at a velocity of 332 m/s (1,090 ft/s) or less. It also provides protection against such threats as .45 Auto, .38 Special +P, and some other factory loads in caliber .357 Magnum and 9mm, as well as the Type I threats. [Ref. 12]

Type II (Higher Velocity .357 Magnum; 9mm). This armor protects against .357 Magnum jacketed soft-point bullets, with nominal masses of 10.2 g (158 gr), impacting at a velocity of 425 m/s (1,395 ft/s) or less, and against 9mm full-jacketed bullets, with nominal velocities of 358 m/s (1,175 ft/s). It also protects against most other factory loads in caliber .357 Magnum and 9mm, as well as the Type I and II-A threats. [Ref. 12]

Type III-A (.44 Magnum; Submachine Gun 9mm). This armor protects against .44 Magnum, lead semi-wadcutter bullets with gas checks, nominal masses of 15.55 g (240 gr), impacting at a velocity of 426 m/s (1,400 ft/s) or less, and against 9mm full-metal jacketed bullets, with nominal masses of 8.0 g (124 gr), impacting at a velocity of 426 m/s (1,400 ft/s) or less. It also provides protection against most handgun threats, as well as the Type I, II-A, and II threats. [Ref. 12]

Type III (high-powered rifle). This armor, normally of hard or semirigid construction, protects against 7.62mm full-metal jacketed bullets (U.S. military designation M80), with nominal masses of 9.7 g (150 gr), impacting at a velocity of 838 m/s (2,750 ft/s) or less. It also provides protection against threats such as 223 Remington (5.56mm FMJ), 30 carbine FMJ, and 12-gauge rifled slug, as well as the Type I through III-A threats. [Ref. 12]

Type IV (armor-piercing rifle). This armor protects against .30-06 caliber armor-piercing bullets (U.S. military designation APM2), with nominal masses of 10.8 g (166 gr) impacting at a velocity of 868 m/s (2,850 ft/s) or less. It also provides at least single-hit protection against the Type I through III threats. [Ref. 12]

Type IV body armor provides the highest level of protection currently available. Designed to stop “armor-piercing” bullets, this armor often uses ceramic materials. Due to the brittle nature of these materials, they may only provide protection for a single shot. [Ref. 12]

Special type. This type is set aside for a consumer who has special requirements for body armor. As such, the consumer can specify the type of projectile to be used and the minimum impact velocities. It is put upon the manufacturer to construct the armor to resist these impacts. [Ref. 12]

Armor type	Test variables				Performance requirements		
	Test Round	Test ammunition	Nominal bullet mass	Minimum required bullet velocity	Required fair hits per armor part at 0° angle of incidence	Maximum depth of deformation	Required fair hits per armor part at 30° angle of incidence
I	1	38 Special RN Lead	10.2 g 158 gr	259 m/s (850 ft/s)	4	44 mm (1.73 in)	2
	2	22 LRHV Lead	2.6 g 40 gr	320 m/s (1050 ft/s)	4	44 (1.73 in)	2
II-A	1	357 Magnum JSP	10.2 g 158 gr	381 m/s (1250 ft/s)	4	44 mm (1.73 in)	2
	2	9 mm FMJ	8.0 g 124 gr	332 m/s (1090 ft/s)	4	44 mm (1.73 in)	2
II	1	357 Magnum JSP	10.2 158 gr	425 m/s (1395 ft/s)	4	44 mm (1.73 in)	2
	2	9 mm FMJ	8.0 g 124 gr	358 m/s (1175 ft/s)	4	44 mm (1.73 in)	2
III-A	1	44 Magnum Lead SWC Gas Checked	15.55 g 240 gr	426 m/s (1400 ft/s)	4	44 mm (1.73 in)	2
	2	9 mm FMJ	8.0 g 124 gr	426 m/s (1400 ft/s)	4	44 mm (1.73 in)	2
III		7.62 mm (308 Winchester) FMJ	9.7 g 150 gr	838 m/s (2750 ft/s)	6	44 mm (1.73 in)	0
IV		30-06	10.8 g	868 m/s	1	44 mm	0
		AP	166 gr	(2850 ft/s)		(1.73 in)	
Special requirement (sec sec. 2.2.7)*						44 mm (1.73 in)	*

* These items must be specified by the user. All of the items must be specified.

Notes: Armor parts covering the torso front and torso back, with or without side coverage, shall each be impacted with the indicated number of fair hits. Armor parts covering the groin and coccyx shall each be impacted with three fair hits at 0° angle of incidence. The deformation due to the first fair hit shall be measured to determine compliance. No fair hit bullet or one impacting at a velocity lower than the minimum required bullet velocity shall penetrate the armor.

Abbreviations: AP – Armor Piercing
 FMJ – Full Metal Jacketed
 JSP – Jacketed Soft Point
 LRHV – Long Rifle High Velocity
 RN – Round Nose
 SWC – Semi-Wadcutter

Table 1: NIJ Body Armor Classification and Testing Summary. From Ref. [12].

3. Classification Requirements:

Types I, II-A, II, and III-A armor are required to prevent penetration from the impact of six bullets at specified velocities and locations for two types of ammunition, including two shots at a 30° angle. Additionally, a maximum of 44mm of deformation to a clay model is allowed. This is to judge the effectiveness of the vest in blunt trauma. Finally, the armor must meet these requirements while both dry and wet. [Ref. 10]

Type III armor requirements are identical to those above, except that only one type of ammunition is specified, and all six test rounds are fired perpendicular to the surface of the armor. [Ref. 10]

Type IV armor is required to resist penetration from only a single type of ammunition (armor piercing) and is only required to prevent penetration from a single perpendicular impact. This last requirement is due to the inclusion of ceramic plates in many type IV body armor systems and the brittle nature of the ceramic material guaranteeing protection for only a single shot. [Ref. 10]

a. Wet Testing

Due to the lubricating action of water, it has been shown that the ballistic efficiency of a fabric can be reduced by 20% when wet. As such, the NIJ has devised a test to insure that fabrics will still meet the minimum requirements for their type even when saturated from perspiration, rain, or other form of precipitation. Laboratory tests conducted by the U.S. Army Natick R&D Command, using a mannequin that simulates human perspiration, verified that vests will absorb perspiration in significant amounts. A

series of tests was also conducted by a research team from the Department of Justice, in which officers wearing untreated vests were subjected to strenuous exercise on a hot humid day. The amount of perspiration in the vests corresponded to the Natick experiments. Tests conducted on these vests verified the significant reduction in the efficiency due to water. In view of this, the NIJ standard requires that a vest continue to provide the rated level of ballistic protection when wet. Due to these requirements, manufacturers use materials that are inherently waterproof, treat the fibers with a water repellant, cover the fabrics with a water repellant material, or any combination thereof. [Ref. 10]

b. Angle Shots

All Type I through Type III-A body armors are required to resist the penetration of bullets striking at an angle to the surface, because the probability of being hit exactly perpendicular to the surface is low. Certain fabrics are less efficient ballistically by as much as 20 percent when a bullet strikes at an angle. Armor must provide the rated level of protection regardless of the angle of impact. [Ref. 12]

c. Performance Testing

The NIJ has established its own standard on conducting performance tests of bulletproof vests. The following graphic, Figure 19, shows the test setup for ballistic testing of police body armor. The armor to be tested is placed on a clay mold. The consistency of this mold is controlled to ensure accurate deformation data. The chronograph measures the bullet velocity to ensure that each test round is within the range required by the standard. Additionally, the location of each impact is prescribed.

This is done to simulate real-world conditions in which impacts are not on the center of the sternum. Figure 20 shows the impact positions prescribed by the NIJ. It is vital that the vest provides the protection required by its type, regardless of impact location.

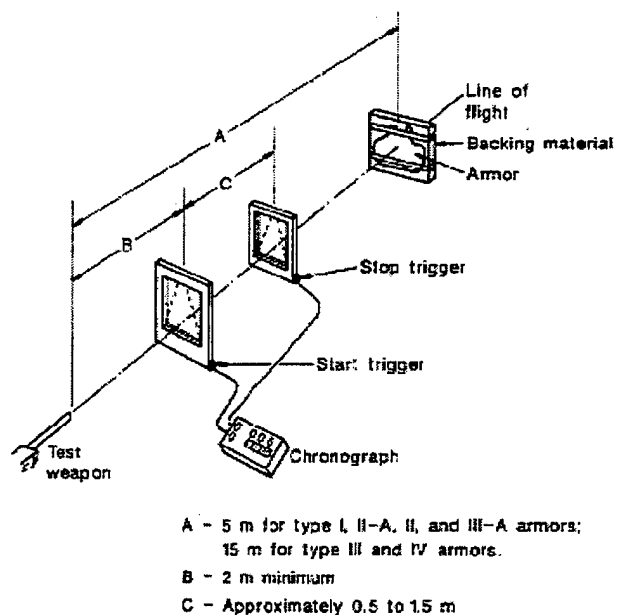
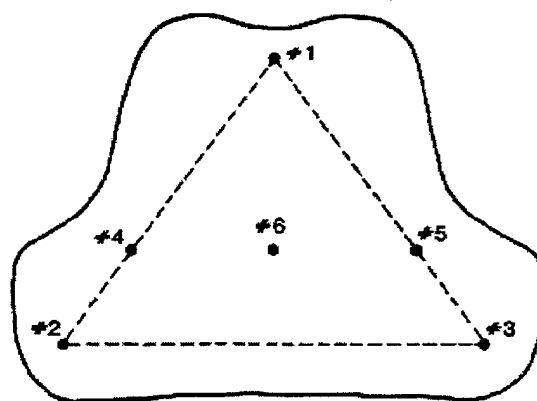


Figure 19: Range Set-up for Test Firings. From Ref. [12].



All shots at least 7.6 cm (3 in) from any edge
and at least 5 cm (2 in) from another shot

Figure 20: Impact Locations for NIJ Testing. From Ref. [12].

The armor is tested both while dry and after being sprayed with a measured quantity of water for 3 minutes on each side before being mounted on the clay. Both the front and back of the armor are tested, and tests are conducted on groin and coccyx protection panels, if present. [Ref. 10]

Although in use by the NIJ, judgement of the efficacy of a body armor material based on clay deformation testing alone has been called into question. Based on test-firings done on goats with bulletproof vests, early tests of low-velocity rounds led to the development of the clay-based model test protocol. The correlation between clay deformation and trauma to the goats has been good for low-velocity projectiles. However, experiments have not been conducted to assess the validity of these clay model tests for high-velocity or large-caliber projectiles. As a result, DeMaio, et al, at the Armed Forces Institute of Pathology, have tested the effects of high-velocity bullets on cadavers wearing a protective vest. As expected, none of the projectiles were able to penetrate the vest; however, the force imparted to the thorax created internal injuries that, in their assessment, would have been lethal. As such, this study has called into question the validity of clay model deformation testing for type determination as the sole determinant of protection for an individual. [Ref. 13]

d. V50 Testing

Another comparative testing method has emerged from use by the military. The V50 ballistic limit testing is a statistical test to evaluate hard armor of homogenous construction used to protect vehicles. It has been incorporated by many manufacturers into the design and assessment stage of their body armor systems. V50

testing as used by body armor manufacturers experimentally identifies a velocity at which a specific projectile has a 50-percent chance of penetrating the armor being tested. In this form of testing, the armor is mounted and bullets are fired to determine the velocities at which the bullets do and do not penetrate the armor. A sufficient number of bullets are fired at various velocities to obtain groups of five nonpenetrating bullets and five penetrating bullets, with a velocity range of no more than 38 m/s (125 ft/s) between the lowest velocity nonpenetrating bullet and the highest velocity penetrating bullet. The V50 ballistic limit is calculated as the average velocity of the 10 bullets. [Ref. 14]

V50 ballistic limit testing allows manufacturers to evaluate various designs against one another to optimize their design for a specific type of body armor. V50 ballistic limit testing is a useful and informative statistical tool for evaluating certain characteristics of armor. In addition to being helpful during the design phase of armor development, it may also have the potential for being a valuable tool in evaluating armor's degradation over time. However, it does not evaluate the level of protection afforded against blunt trauma, nor is a uniform standard for V50 ballistic limit testing used by all manufacturers. Therefore, it is not suited for use in a performance standard. [Ref. 14]

4. Body Armor Construction

By deforming a bullet upon impact, the soft armor in a protective vest dissipates the kinetic energy of the bullet into the multiple layers of the vest. The fibers absorb and disperse, through strain, the impulse momentum that is transmitted to the vest from the bullet, causing the bullet to deform or "mushroom." The vest must provide a resistive

force, F , for a time, Δt , so as to reduce the momentum of the bullet to zero according to $F\Delta t = m\Delta v = impulse$. The vest is designed to make Δt as large as possible and to spread the force over as large an area as possible. Each successive layer of material in the vest absorbs additional energy, until such time as the bullet has been stopped. Because the fibers work together both in the individual layer and with other layers of material in the vest, a large area of the garment becomes involved in preventing the bullet from penetrating. This also helps in distributing the forces that can cause nonpenetrating injuries (what is commonly referred to as "blunt trauma") to internal organs. Research by Philip Cunniff at the U.S. Army Natick Research site has lead to the development of a semiempirical model of the ballistic impact performance of textile-based personnel armor. [Ref. 15] His equations predict the residual bullet velocity after impact with a vest layer, dependent upon the mass of the bullet, the areal density of the fabric system, the presented area of the projectile, and the angle of incidence. Additional work has been done by Vinson and Zukas [Ref. 16] to develop a mathematical model for the physics of high-velocity bullet impacts to a textile fabric. Their study has created a stepwise procedure for use a on computer to determine strains, projectile position, forces, and decelerations as a function of time. However, their model does not incorporate the loss of kinetic energy accompanying the deformation of the projectile.

Combining soft armor, which absorbs bullet energy, with a hard plate, such as steel or boron carbide, it is feasible to create a vest impervious to a bullet. However, selection of a body armor system is dependent upon the threat that will be faced. For instance, police officers are more concerned with bullets from handguns. As such,

exclusively soft armor systems, which are concealable, more flexible, and, hence, more comfortable, may be sufficient. However, for military applications, use of rigid or semi-rigid systems will be required due to the nature of the threats faced.

a. Methods of Construction

The primary element of a body armor system is the "ballistic panel." Created from multiple layers of a weaved ballistic fiber, these panels are inserted into a "carrier." The carrier is essentially the harness that holds the ballistic panels in place and is usually created of nylon or cotton. Depending upon the design, the panels may be removable or stitched into the carrier. Additionally, pockets may be incorporated into the carrier for insertion of the hard plates. As such, versatile bulletproof vest can be created.

The ballistic fabric is the key element of the vest. As such, its properties are dependent upon the manufacturer and are guarded as proprietary information. Each manufacturer incorporates different fibers with different weaves into their fabrics. The ballistic performance of a fabric is dependent upon the method in which the fibers are woven and the types of fibers used. Additionally, many manufacturers incorporate nonballistic materials into the layers of the ballistic panel in order to help reduce blunt trauma.

b. Materials Used

Due to the proprietary nature of these fibers, material properties are very difficult to obtain. As such, the following fibers will be discussed based on the claims made by their manufacturer.

Dupont has been one of the premier developers of ballistic fibers. Its Kevlar® brand fiber, first developed in 1965, was the first material identified for use in the modern generation of concealable body armor. Kevlar® is a manmade organic fiber, with a combination of properties allowing for high strength with low weight, high chemical resistance, and high cut resistance. Kevlar® is also flame resistant, does not melt, soften, or flow, and the fiber is unaffected by immersion in water. [Ref. 10]

Kevlar® 29, introduced in the early 1970s, was the first generation of bullet-resistant fibers developed by DuPont and helped to make the production of flexible, concealable body armor practical for the first time. In 1988, DuPont introduced the second generation of Kevlar® fiber, known as Kevlar® 129. This fabric offered increased ballistic protection capabilities against high-energy rounds such as the 9mm full metal jacket. In 1995, Kevlar® Correctional™ was introduced, which provides puncture-resistant technology to both law enforcement and correctional officers against puncture-type threats. [Ref. 10]

The newest addition to the Kevlar® line is Kevlar® Protera™, which DuPont made available in 1996. DuPont contends that the Kevlar® Protera™ is a high-performance fabric that allows lighter weight, more flexibility, and greater ballistic protection in a vest design due to the molecular structure of the fiber. Its tensile strength and energy-absorbing capabilities have been increased by the development of a new spinning process. [Ref. 10]

Spectra® fiber, manufactured by AlliedSignal, is an ultra-high-strength polyethylene fiber. The fibers consist of ultra high molecular weight polyethylene

dissolved in a solvent, spun through a series of small orifices, and then solidified through cooling. The fibers are then placed in two unidirectional layers, at a 90-degree angle, and covered with a flexible resin. Finally, two thin sheets of polyethylene film are spread on either side of the fibers and resin. The resulting fabric is the Spectra Shield™ composite. According to AlliedSignal, the fabric is incredibly strong, lightweight, and has excellent ballistic protection capabilities. This fabric is incorporated into a variety of styles for both concealable and hard armor applications. The same spinning technology is used by AlliedSignal to manufacture another type of shield composite called Gold Shield®. Gold Shield® is manufactured using aramid fibers instead of the Spectra fiber. Gold Shield® is currently made in three types: Gold Shield® LCR and GoldFlex®, which are used in concealable body armor, and Gold Shield® PCR, which is used in the manufacture of hard armor, such as plates and helmets. [Ref. 10]

F. LITERATURE SURVEY

To date, there is little existing research into the dynamics of bullet impacts to the thorax. The predominant areas of study have been into the creation and validation of a human thorax finite element model and into analysis of the thorax reaction to blunt impacts in automobile collisions. A majority of the research has been concerned with static analyses to validate human thorax finite element models. Very few studies have examined dynamic effects on the thorax. The present research project breaks new ground in the use of the finite element method for investigations into the biomechanical response of the thorax to dynamic loading.

Research into a mathematical model of the thorax began with the studies of Roberts and Chen in 1970. [Ref. 17] Utilizing gross geometric data and approximate cross-sectional properties, they were able to develop an elastostatic finite element model of the thorax. Placing the sternum of the model under various static loading cases, they obtained reasonable data for sternal displacements, thereby validating their model. Due to the success of their model, it has been incorporated into most of the models utilized in later studies of the thorax. In addition, it provided the framework for the model developed by Hughes in his work and, consequently, was incorporated into the model developed for this study. [Ref. 18]

Andriacchi, Schultz, Belytschko, and Galante [Ref. 19] used the model developed by Roberts and Chen in a study of the mechanics of the human skeleton. In order to study the interactions between the rib cage and the spine, their model further refined the existing model. In their study, they were able to examine the bending responses of the spine, the lateral stability of the spine, and the underlying mechanisms in scoliotic deformities. However, their analyses relied on static loading cases on the thorax and were not very useful in the development of a valid dynamic model.

Along with the development of the geometry of a three-dimensional thorax model, research was done into the material properties of the thorax. Due to the individual nature of these properties, these studies compiled results for a large population. In work by Yoganandan and Pintar, the mechanical properties of the seventh and eighth rib pairs were determined for 30 cadavers. [Ref. 20] Utilizing three-point bending techniques on isolated ribs, the researchers were able to determine the cross-sectional area, moment of

inertia, failure load, deflection, and Young's modulus. However, it is believed that further investigation into the material properties of the other rib pairs as well as the costal and articular cartilage is necessary due to the individual nature of these properties.

In the study by Hughes [Ref. 18], the data from Andriacchi, et al and Yongananda, et al was combined to create a viable three-dimensional model of the thorax. The computed response due to an applied static load was studied to validate the finite element model. In addition, a limited dynamic study of the impact of a bullet into body armor protecting the thorax was also investigated. Numerical data were compared to that obtained from "live-fire" exercises performed on human cadavers. Although the correlation was strong, the response of the sternum in the model exhibited large oscillations, which were not observed in the cadavers. It is believed that this occurred as a result of the lack of damping in the model. Soft tissues, such as the skin and muscle, were incorporated into the model for the present study to supply damping for these oscillations.

The only existing cadaveric study on the biomechanical response of the thorax to bullet impacts was performed by DeMaio, et al at the Armed Forces Institute of Pathology. [Ref. 13] In their studies, cadavers were protected with a bulletproof vest incorporating either soft armor alone or soft armor plus one of two variations on a ceramic plate. These cadavers were then struck with either a NATO 9mm round or a NATO 7.62mm M80 ball round fired from a distance of 50 feet. Various parameters were recorded including the accelerations of the sternum, spine, and carina, and the left and right ventricular pressures. Post-shot autopsies were performed to judge injury and

assess survivability. The model utilized in the present study was created in an attempt to obtain similar results from finite element analysis for these parameters, dependent upon the projectile and body armor used. As such, the boundary conditions and loads applied in our study were derived from the test parameters used at AFIP.

III. FINITE ELEMENT MODEL

A. HUMAN THORACIC BODY MODEL

The human thorax presents a myriad of modeling problems for the researcher. Along with the complex geometries of the various ribs themselves, there are multiple connections, such as the articular cartilage between the rib pairs and the vertebrae that must be accurately modeled to create a viable model. In addition, the material properties of the ribs are not constant along their entire length. This adds an additional level of complexity to the model. Another fundamental concern is the wide variation that may take place between individuals. Thus, the correct material properties for a 20-year-old male are unlikely to match those of a 70-year-old female. In the model created for this study, depicted in Figure 21 below, all the finite element position nodal data were taken from work by Andriacchi, et al [Ref. 19] and Roberts and Chen [Ref. 17], which was later adapted by Hughes [Ref. 18].

1. Ribs

The modeling of the ribs was an area of some difficulty due to their complex shape and material properties. The size and shape of the ribs correspond to that of a smaller, female build. Each rib is represented by thirteen beam elements. A larger number would have been prohibitively costly in terms of computation time. Each element is given a specified cross-sectional area dependent upon its distance from the spine. This enables the correct size, shape, and angle of the head, tuberosity, midaxillary line junction, costochondral joint, and sternochondral junction to be

modeled. In addition to the geometry of the ribs, each element had to have its material property specified. The values used were based on the work done by Yogananda and Pintar [Ref. 20], who utilized three point bending experiments to determine material properties for the seventh and eighth rib of multiple subjects. Their “average” values were used to determine the approximate material properties for each element of each rib pair. The ribs were assumed to be composed of only compact bone and were modeled as a linear elastic material. The Young’s Modulus chosen was 2.83 GPa; a density of 1000 kg/m³ and a Poisson’s ration of 0.2 were used.

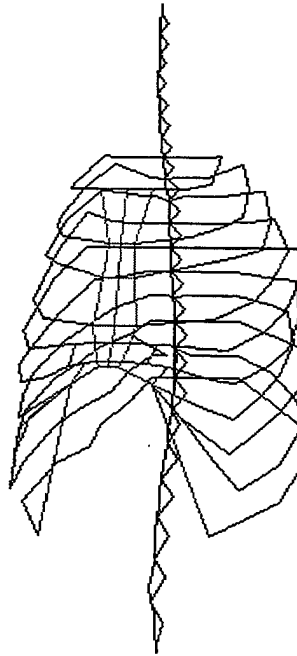


Figure 21: Plot of Sternum, Ribs, Spine, and Cartilage

2. Spine

Due to the nature of this study, the complexities of the spine were not fundamental to the research being conducted. As such, the spine was modeled by a series

of beam elements, based on previous experiments. [See Refs. 21 and 22] Each modeled vertebra consisted of two beam elements, with an intervening beam element between adjacent vertebra to model the intervertebral disc. The facet joints were modeled by connecting two beam elements, one from the midpoint of each adjacent vertebra. Figure 22 below depicts how the spine was modeled. The material properties for the vertebrae and the vertebral disc derived from work done by Sundaram and Belytschko [Ref. 23]. The vertebra and facet joints were modeled with a Young's Modulus of 12.13 GPa, a density of 1000 kg/m³, and a Poisson's ratio of 0.2. The intervertebral discs were given the following material properties: Young's Modulus: 1.5 GPa, Density: 100 kg/m³, and Poisson's ratio: 0.2.

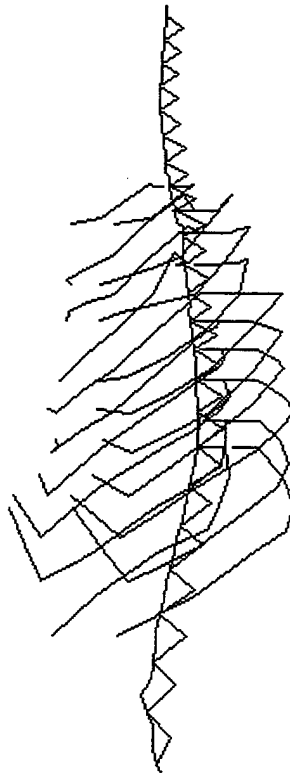


Figure 22: Medial View of the Ribs and Spine

3. Sternum

The sternum, as seen in Figure 23 below, was modeled with a series of twelve thin shell elements. Each element was given a specified thickness of 0.25 inches (0.63 cm) to create the three-dimensional model. The material properties for the sternum were derived from the compact bone properties of rib 4. As such, the sternum's Young's Modulus was 12.13 GPa, density was 1000 kg/m³, and Poisson's ration was 0.2.

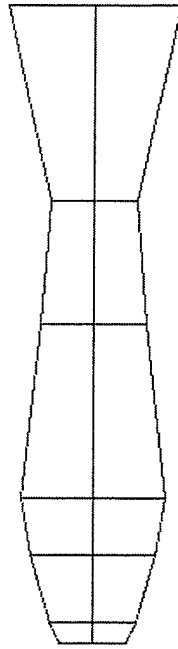


Figure 23: Sternum Shape in Thorax Model

4. Muscle

The modeling of the muscle, which is shown in Figure 24, was done with 24 solid elements. The elements varied in thickness from 0.25 inches (0.63 cm) along the central, anterior edge of the sternum to a maximum of 2.35 inches (5.97 cm) at the most distal position of rib #4. This accurately models the correct curvature of the muscle along the anterior side of the thorax. The material properties of muscle were modeled with a viscoelastic material type. (See Refs. 24, 25 and 26 for a discussion on viscoelasticity.) The material property values utilized were a density of 950 kg/m^3 , a bulk modulus of $5 \times 10^5 \text{ Pa}$, a short-time shear modulus of $1 \times 10^5 \text{ Pa}$, a long-time shear modulus of $1 \times 10^4 \text{ Pa}$, and a decay constant of 1000. The equation used to calculate the shear relaxation behavior is as follows:

$$G(t) = G_{\infty} + (G_0 - G_{\infty})e^{-\beta t}$$

$G(t)$ = Shear Modulus
 G_0 = Short-Time Shear Modulus
 G_{∞} = Long-Time Shear Modulus
 β = Decay Constant
 t = Time

This time-dependent shear modulus relationship is explained further in Appendix

B.

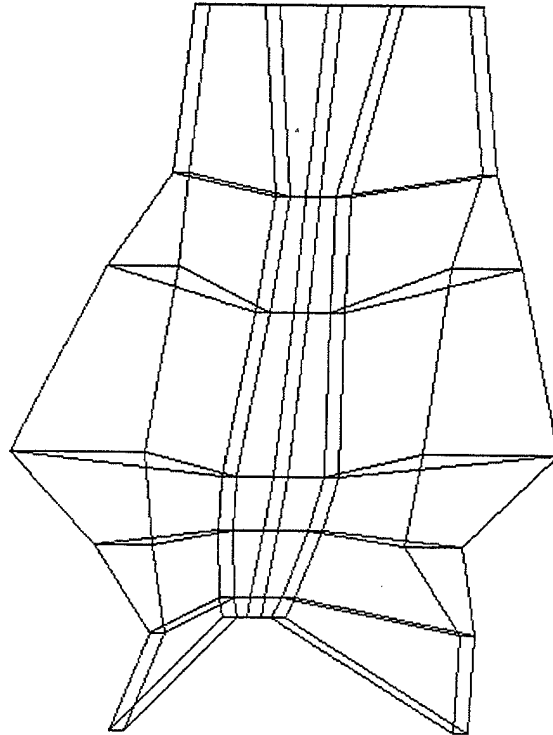


Figure 24: Muscle as Constructed in Thorax Model

5. Cartilage

The cartilaginous connections of the thorax were modeled with beam elements, as depicted by the darker lines in Figure 25 below. A single beam element was used to

model the sternochondral joint whereas two beam elements were utilized to model the articular cartilage between the rib and the vertebrae. The material properties of the cartilage at the sternochondral junction were given values of 64.7 MPa for Young's Modulus, 1000 kg/m^3 for density, and 0.2 for Poisson's ratio. Material properties for the chondracostal cartilage were a density of 1000 kg/m^3 , a Young's Modulus of 5 MPa, and a Poisson's ratio of 0.2. Additionally, a series of vertical cartilaginous connections at the inferior edge of the sternum, modeled as beam elements, were used to create the subcostal angle.

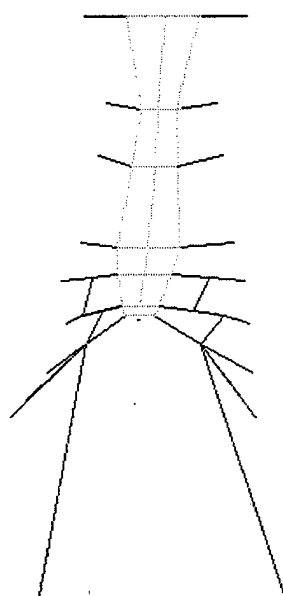


Figure 25: Articular Cartilage Connecting Sternum and Ribs

B. BODY ARMOR

The body armor itself consisted of a plate of CBA (concealable body armor) composite material and sheet of Kevlar. Due to the proprietary nature of these materials, the determination of their material properties was subject to some guesswork. However, realistic values were used throughout the study. The material properties of Kevlar were assumed to be a density of 1440 kg/m^3 , a Young's Modulus of 1 GPa, and a Poisson's ratio of 0.2. The CBA plate was given a density of 2500 kg/m^3 , a Young's Modulus of 448 GPa, and a Poisson's ratio of 0.2. In one investigation that was undertaken, a plate of CBA composite material was modeled with 126 thick shell elements. The thickness of this plate was set as 0.5 inches (0.51 cm). This plate was directly attached to a sheet of Kevlar, modeled by 126 thick shell elements as well and a thickness of 0.25 inches (0.63 cm). This sheet was modeled such that it projected directly across from the most anterior points of the muscle tissue as noted below in Figure 26. This created a gap between the muscle and the Kevlar above the sternum, which is an accurate representation of the actual placement of the vest when worn. In another investigation, the CBA plate was removed to simulate the usage of just soft armor.

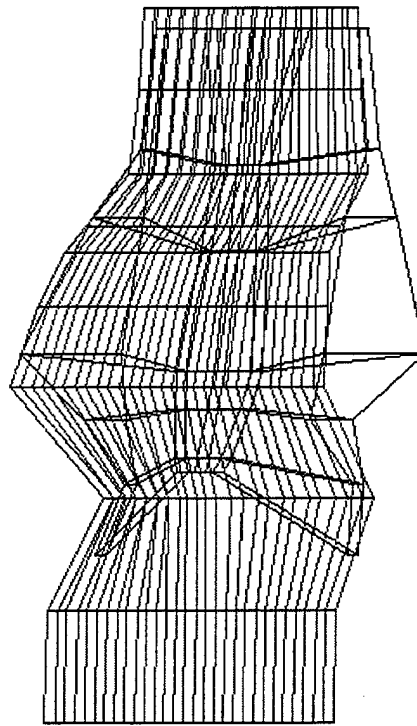


Figure 26: Depiction of Kevlar Vest Overlaying Muscle

C. INTERFACE ELEMENTS

In order to prevent rigid body motion of the body armor after bullet impact, several contact elements had to be added to the model. The interface between the vest and the muscle was modeled with a tied-type contact element. This allows for the movement of the vest in one direction to impart a force onto the muscle, while movement in the other creates a separation between the two parts without any transfer of force. Additionally, springs and dampers were added between the muscle and the ribs. This was necessary to portray the correct viscous nature of the muscle and its corresponding transfer of force to the ribs. This also suppressed spurious oscillations in the sternum.

D. PROJECTILE

Due to inherent problems with the analysis, more than one set of contact elements was not possible. Thus, it was not possible to insert contact elements between the bullet and the body armor. Therefore, the projectile was given the correct mass and shape and was attached directly to the most anterior body armor component. This was either the CBA plate or the Kevlar sheet, depending upon the test being run. It is visible as the single element on the left side of Figure 27. The projectile was modeled as a single solid element and given the dimensions and material properties of either a NATO 7.62 mm Ball M80 round or a NATO 9 mm full metal jacket round. In order to model the motion of the projectile, the most anterior four nodes of the projectile were given an initial velocity. This imparted a momentum to the bullet that was transferred to the body armor in a manner consistent with that of bullet impact analysis. The material properties of the projectile were based on a linear elastic material, with the Young's modulus and density corresponding to that of steel. The initial velocity of the projectile was determined experimentally during test firings at the Aberdeen Proving Grounds in Maryland. [Ref. 13] These numbers (2900 f/s for the 7.62mm round and 1500 f/s for the 9mm round) were used in the DYNA3D input file. By directly modeling the motion of the bullet, it was possible to avoid errors which might occur in an attempt to model a forcing function to apply to the body armor.

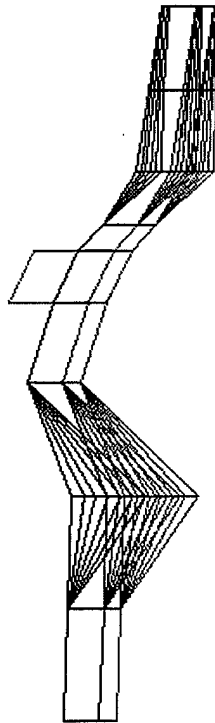


Figure 27: Medial View of CBA Plate and Kevlar Vest

E. BOUNDARY CONDITIONS

The boundary conditions that were chosen were based on the experimental set-up during the cadaveric studies at Armed Forces Institute of Pathology. [Ref. 13] In their experiment, cadavers were laid flat on a wooden board and secured to it via wires. To approximate this set-up, the most posterior nodes of the thoracic model were constrained to prevent translations. It is believed that this would adequately model the experimental set-up.

F. ANALYSIS CODE

After the finite element model had been created, it was put into the input deck specifications for DYNA-3D, a finite element analysis program available from Lawrence Livermore National Laboratories. The particular version utilized was DYNA-3D version N-12, compiled on 10-03-98. This software was run on Silicon Graphics International OCTANE workstations running IRIX 6.4.

IV. RESULTS AND DISCUSSION

After construction of the finite element model and imposition of the boundary conditions and initial velocities for the projectile, an analysis was run for a model time duration of two milliseconds. The DYNA3D input deck was designed to output the acceleration, velocity, and displacement in the anterior to posterior direction for the center of the sternum as well as the T7 vertebra. These locations correspond to those used by DeMaio, et al at AFIP [Ref. 13]. Data obtained from the DYNA3D analysis was subsequently smoothed using a simple twelve-point averaging method to remove aberrant oscillations. The experimental data from DeMaio, et al [Ref. 13] was obtained as text files with the time and value listed and did not require processing before comparison. The model was analyzed with two variations. The first was that of the 7.62mm projectile impacting on a vest constructed of Kevlar and a CBA (concealable body armor) plate. The second was the impact of a 9mm projectile into a body wearing only the Kevlar vest. For purposes of validation, the acceleration information was used as the primary comparison data between that from DYNA3D and that obtained from AFIP. This was due to the use of numerical integration by the experimenters at AFIP to obtain the velocities and displacements. In order to set a standard for comparisons, the characteristics that were focused upon were the times and magnitudes of the first peak and trough, and the trend of the parameter at the end of the analysis period.

A. VALIDATION STUDY

1. CBA Plate, Kevlar Vest, and NATO 7.62mm M80 Ball Round

This test case utilized the NATO 7.62mm M80 ball round as the projectile, with an impact velocity of 966 m/s. This velocity is consistent with those obtained by DeMaio, et al from a chronometer during their test firings [Ref. 13]. The vest consisted of a layer of Kevlar and a CBA plate. The time duration of the model analysis time was five milliseconds.

The following figures (see Figures 28 through 33) display the results that were obtained from the DYNA3D analysis, labeled FEA, versus those results obtained experimentally, labeled as Exp. #801 to refer to the case number used by DeMaio, et al [Ref. 13]. They include comparisons of sternum and spinal accelerations, velocities, and displacements in the anterior to posterior direction. This direction is chosen because it is the direction of the projectile upon impact.

The match between the experimental sternal acceleration data and the computer model was excellent for this case, as illustrated in Figure 28. The magnitude of the initial peak is of the right order, the location of the first peak and troughs are at the right time, and the long-term behaviors are similar. The only discrepancy occurs at approximately one millisecond. Postmortem examinations revealed that massive sternal fractures had occurred in this case. These fractures would significantly reduce the stiffness of the sternum and allow for greater accelerations, hence a greater magnitude of the trough, than those predicted by the DYNA3D analysis. This is because there are no failure modes included in the DYNA3D model allowing for bone fractures. Otherwise, there was an

excellent correlation between the two cases. In this particular case, the analysis was run for five milliseconds. However, due to the long computer processing time necessary, as well as the consideration that the most important responses occurred in the first two milliseconds, all subsequent analyses were run for a shorter model time of two milliseconds.

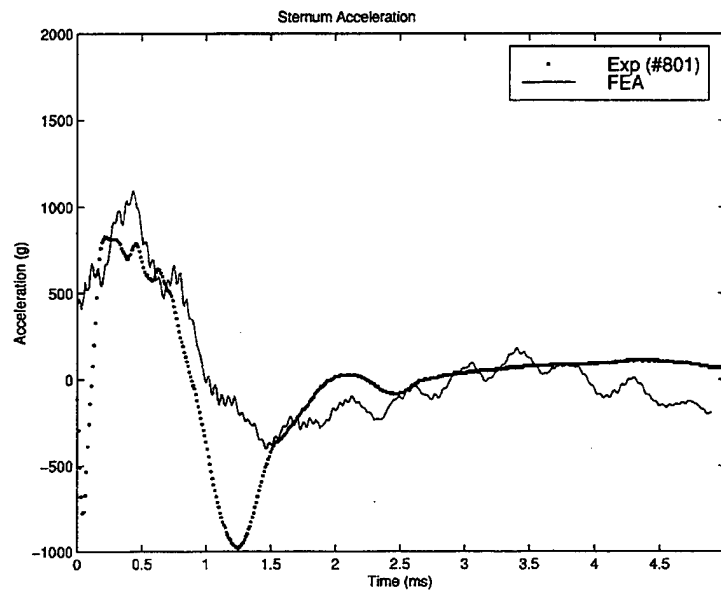


Figure 28: Sternum Acceleration (CBA Plate & Kevlar). Experimental Data (Exp. (#801)) versus DYNA3D Analysis (FEA). After Ref. [13].

The data for the sternum velocity did not match as well as expected. In their original investigation, DeMaio, et al [Ref. 13] only recorded the accelerations and then used numerical integration to obtain the results for the velocities and displacements. As such, the acceleration data will be considered more fundamental to validation. In this particular example (see Figure 29), the general shapes of the velocity curves match well. However, there exists some doubt about the initial response of the sternum immediately

upon impact, due possibly to instrumentation error or interference effects. The initial acceleration is in the opposite direction to the impact direction. Consequently, the data obtained for the sternum acceleration at the immediate time of impact may not be completely accurate (See discrepancy in first 0.2 milliseconds in Figure 28). This discrepancy then propagates through to the estimations of the displacements and velocities due to the use of numerical integration. As such, in the sternum velocity graph, the initial downward motion of the experimental results, dependent upon the initial negative acceleration in the first 0.2 milliseconds in Figure 28, is questionable. The separation that this initial motion creates is carried through the rest of the analysis. If this initial separation were discounted, the match between the two would be excellent.

DeMaio, et al [Ref. 13] estimated about 30 millimeters of displacement at the sternum at approximately 30 milliseconds from experimental observation even though there was no direct measurement of the displacement. However, the results displayed (see Figure 30) below do not show this displacement. They obtained this displacement value at the end of their data recording period, at approximately 30 milliseconds. Due to the computer time required to run an analysis for this length of time, the period of investigation was limited to five milliseconds with the final displacement to be extrapolated from the resulting data. As the velocity begins to approach zero at the end of the five millisecond period, the displacement will obtain a steady-state value. Extrapolating from the available results leads to an estimation of between 25 and 30 millimeters of displacement, corresponding to the results obtained by DeMaio [Ref. 13].

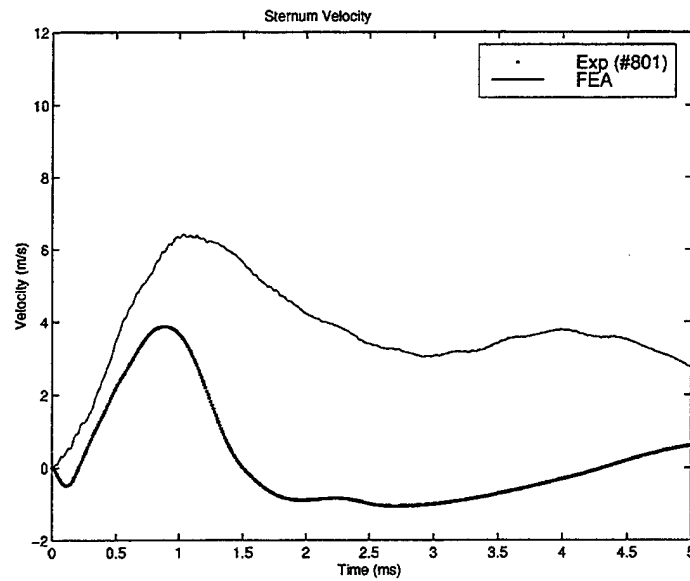


Figure 29: Sternum Velocity (CBA Plate & Kevlar). Experimental Data (Exp. (#801)) versus DYNA3D Analysis (FEA). After Ref. [13].

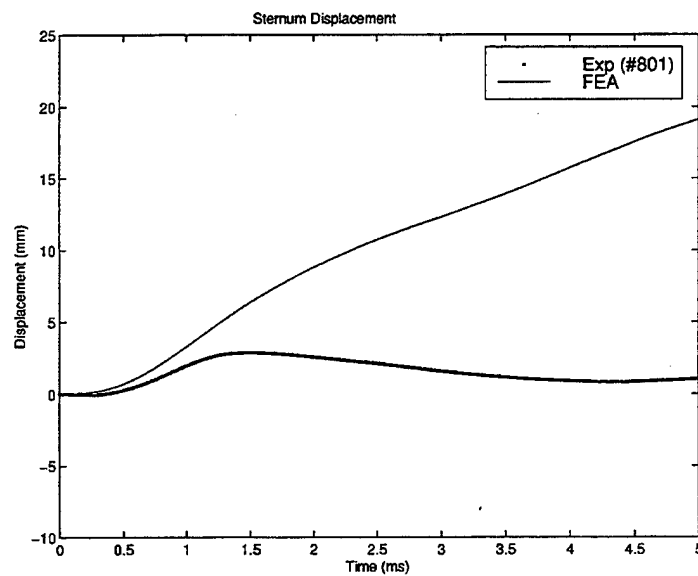


Figure 30: Sternum Displacements (CBA Plate & Kevlar). Experimental Data (Exp. (#801)) versus DYNA3D Analysis (FEA). After Ref. [13].

The comparison between the spinal acceleration results from the computer model and the experimental data also correlated well, as depicted in Figure 31. The magnitudes are approximately the same and the points of inflection are located at similar times. The discrepancy between the magnitudes lends credence to the idea that the model is too stiff. However, this is an inherent problem in the finite element method and does not detract from the validity of the computer model. Additionally, it is important to note that the correlation is excellent until one millisecond. It is believed that the separation after this point is due to the massive sternal fractures that occurred and the resulting higher accelerations in the sternum than those predicted by DYNA3D. Because the forces imparted from the impact on the anterior face of the thorax must propagate through the connective and soft tissues as well as the skeleton to affect the spinal acceleration, these fractures in the sternum have a direct consequence on the acceleration of the spine. However, due to the same overall trends being predicted, the high degree of correlation lends validity to the constructed model. This correspondence is also noted in the predicted and experimental values for the spinal velocities (see Figure 32) and displacements (see Figure 33).

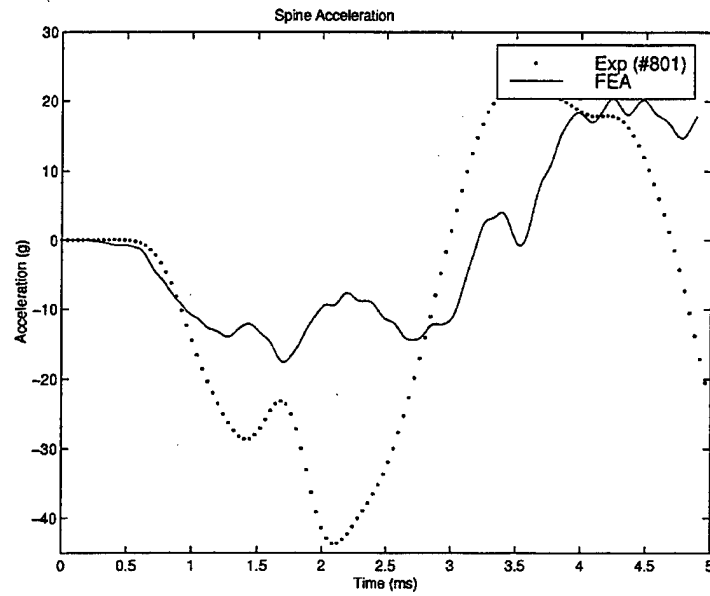


Figure 31: Spinal Acceleration (CBA Plate & Kevlar). Experimental Data (Exp. (#801)) versus DYNA3D Analysis (FEA). After Ref. [13].

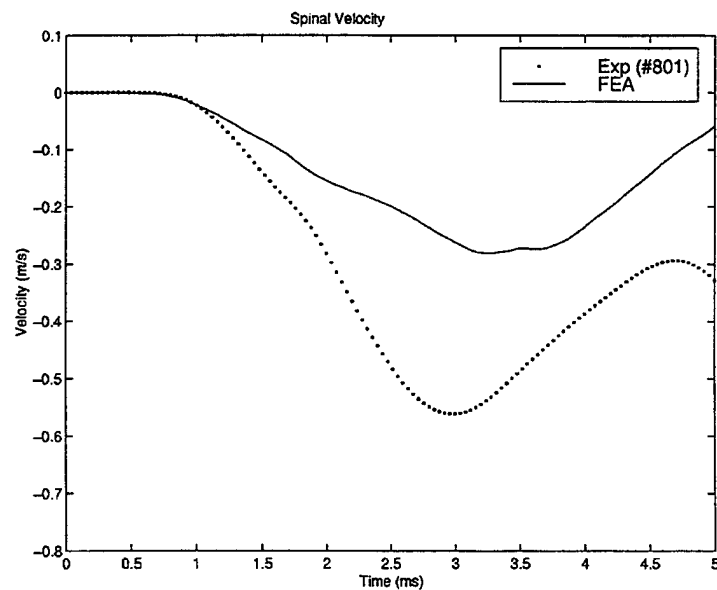


Figure 32: Spinal Velocity (CBA Plate & Kevlar). Experimental Data (Exp. (#801)) versus DYNA3D Analysis (FEA). After Ref. [13].

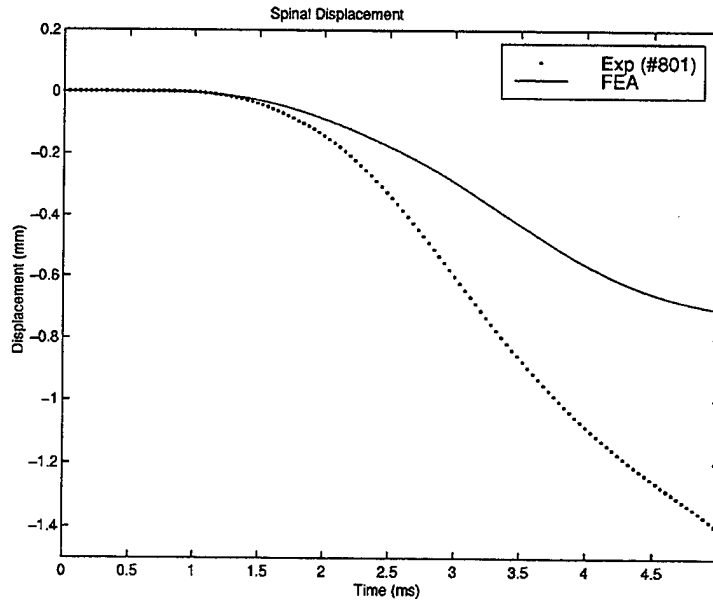


Figure 33: Spinal Displacement (CBA Plate & Kevlar). Experimental Data (Exp. (#801)) versus DYNA3D Analysis (FEA). After Ref. [13].

2. Kevlar Vest and NATO 9mm Round

This test case utilized the NATO 9mm full metal jacket round as the projectile, with an impact velocity of 500 m/s. The armor vest consisted of only a layer of Kevlar. The analysis time duration was two milliseconds.

The correlation between the results from DYNA3D and those of experimental case #678 reported by DeMaio [Ref. 13] were high in the early analysis time for this case as well, as seen in Figures 34 through 39 below. The discrepancies that occur at the later time in the sternum acceleration can be attributed to the inherent stiffness of the finite element method as well as other sources of error. In Figure 34 below, note that the locations for the first and second peak match exactly. Unfortunately, the magnitudes of these first peaks were clipped in the experimental data, yet extrapolation from the

available data suggests that the magnitudes would match very well. It is believed that the method by which the accelerometer was mounted accounts for the discrepancy noted at approximately 0.9 milliseconds in Figure 34. Securing the accelerometer to the posterior side of the sternum with a length of string allows for accurate measurements of acceleration as the sternum moves in the posterior direction, but stretching of the string under anterior acceleration of the sternum may create the noted discrepancy.

Additionally, the massive sternal fractures noted in the previous validation case are not noted in post-mortem report for this test case. As such, the magnitude of the experimental response at the first trough does not exceed that predicted by the DYNA3D analysis. However, the long-term behavior of the DYNA3D predictions and those obtained experimentally match well, with both approaching zero. For this test case, similar to the first, the discrepancies noted in the acceleration data propagate through to the predictions of velocity and displacements due to the use of numerical integration. There is a significant deviation between the experimental results and those predicted by DYNA3D for the spinal acceleration, velocity, and displacements. Although the possibility for instrumentation error, such as incorrect mounting of the accelerometer during the cadaveric studies exists, the most logical explanation for the discrepancy is due to problems with the boundary conditions. The experimental method utilized called for securing the cadaver to a backboard by a simple wire wrapping around the body and backboard. This may have allowed for movement of the cadaver that the boundary conditions imposed on the FEA model would have made impossible. This movement would have a more pronounced effect on the spinal data rather than that of the sternum

due to the presence of the backboard limiting the movement of the spine whereas no such restrictions would exist on the sternum. Additional to the boundary conditions, simple mechanics dictates that the high accelerations imposed on the thorax should result in higher magnitude accelerations in the spine than those actually reported. As such, we do not feel that there is any need to question the viability of our model. Rather, the consistent behavior of our model under these various load conditions lends credibility to it. A comparison between Figure 31 and Figure 37, the spinal accelerations for the two test cases, illustrates the consistent behavior of the FEA model. The shape predicted through FEA in the second test case (Figure 37) matches well with that experimentally determined in test case one (Figure 31). This indicates that the model performed consistently and lends credence to a boundary condition mismatch between the experimental work and the FEA modeling.

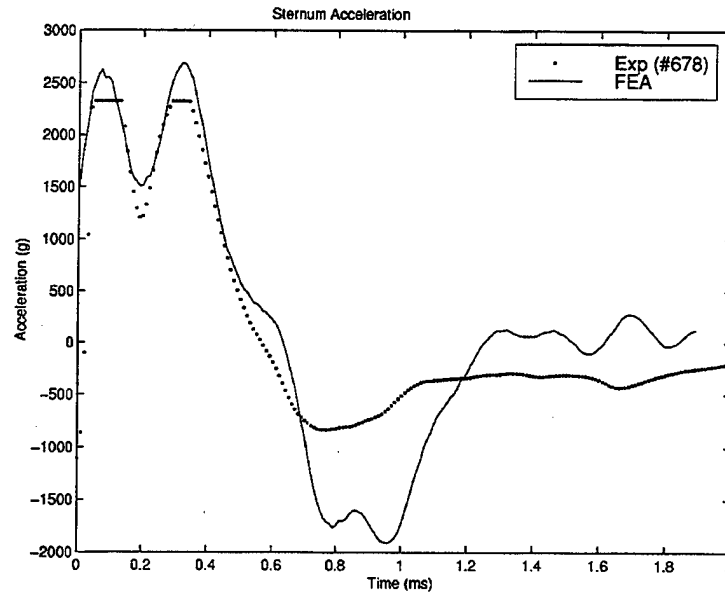


Figure 34: Sternum Acceleration (Kevlar only). Experimental Data (Exp. (#678)) versus DYNA3D Analysis (FEA). After Ref. [13].

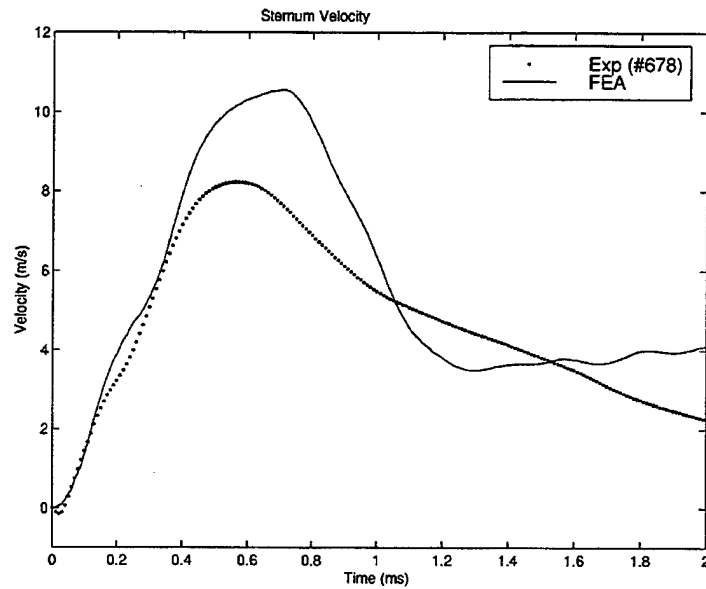


Figure 35: Sternum Velocity (Kevlar only). Experimental Data (Exp. (#678)) versus DYNA3D Analysis (FEA). After Ref. [13].

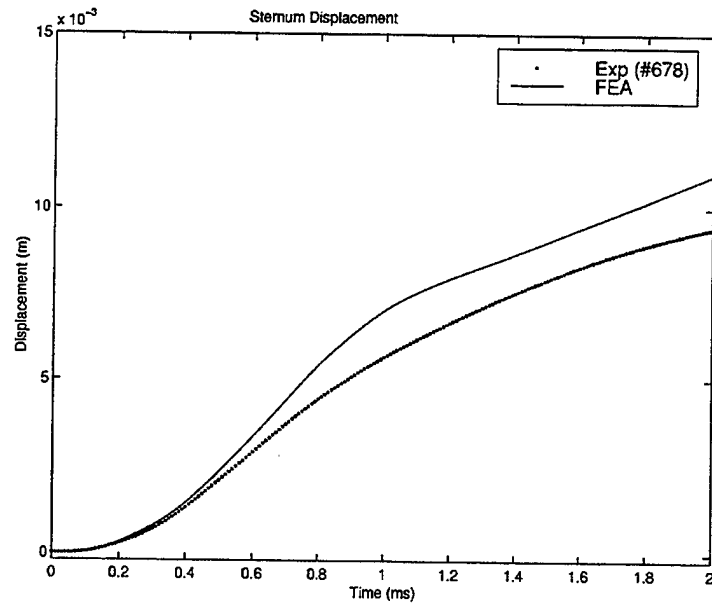


Figure 36: Sternum Displacements (Kevlar only). Experimental Data (Exp. (#678)) versus DYNA3D Analysis (FEA). After Ref. [13].

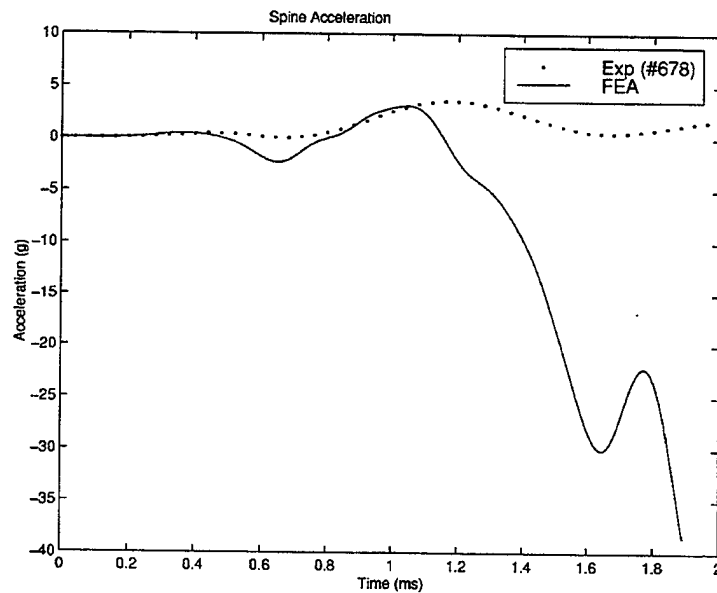


Figure 37: Spinal Acceleration (Kevlar only). Experimental Data (Exp. (#678)) versus DYNA3D Analysis (FEA). After Ref. [13].

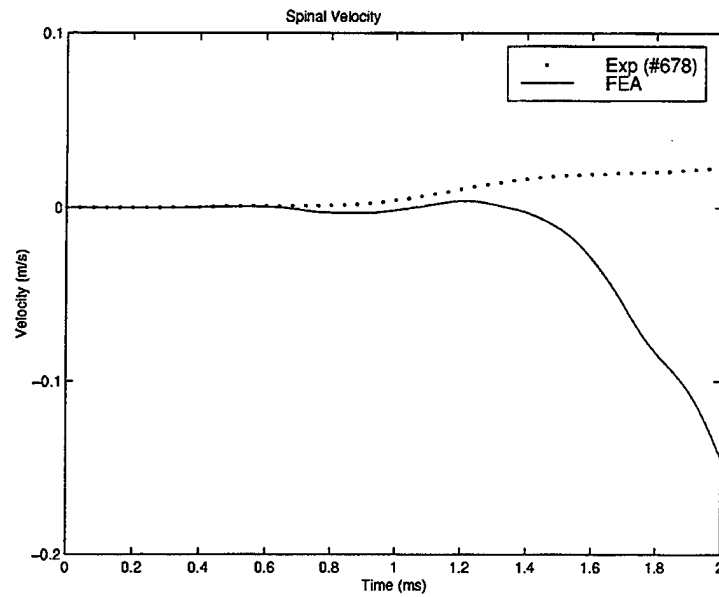


Figure 38: Spinal Velocity (Kevlar only). Experimental Data (Exp. (#678)) versus DYNA3D Analysis (FEA). After Ref. [13].

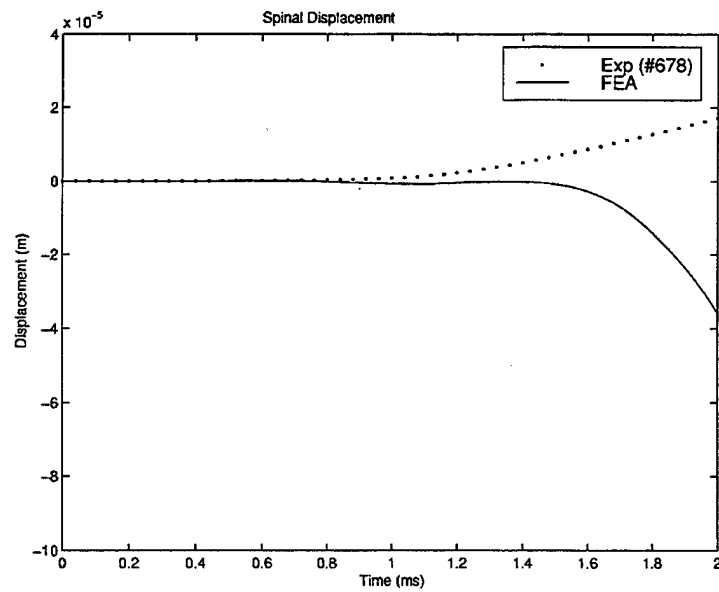


Figure 39: Spinal Displacement (Kevlar only). Experimental Data (Exp. (#678)) versus DYNA3D Analysis (FEA). After Ref. [13].

B. PARAMETRIC STUDY

In order to gain a better understanding of the constructed model, a parametric study was conducted. Parameters such as the Young's Modulus of the sternum, muscle, Kevlar, CBA (concealable body armor) plate, sternal cartilage, and intervertebral disc were changed individually to assess their importance to the overall behavior of the model through comparisons with the Kevlar and CBA plate case presented above. Due to the use of numerical integration of the experimental data to obtain the velocities and displacements, the accelerations were considered the most important element for comparison. Through this study, the muscles, the Young's Modulus of the sternum articular cartilage and of the skeleton in general, the contact elements and gap between the vest and the sternum, the size of the thorax, and the densities of the CBA and Kevlar were determined to be the most important factors in determining the correct behavior of the model. The following graphs are those that were obtained after changing one of the factors listed above. Note that in Figures 40 and 41, as in all subsequent figures, the three items graphed are the experimental results obtained by DeMaio, et al [Ref. 13], the results from DYNA3D for the first validation case (CBA plate, Kevlar vest, and NATO 7.62mm M80 ball round) (See Section A-1), and the results returned from DYNA3D with one of the parameters changed. All of the test cases conducted are included in Appendix A.

The most important element in the behavior of the model was the inclusion of muscle. Removing the muscle from the model had serious ramifications to the predictive power of the biomechanical response. It is believed that the muscles provide much of the

damping and viscous effects that are essential to reduce the high forces that are imparted to the body upon impact. (Recall that the muscles were modeled as a viscoelastic material.) Additionally, muscle damping suppresses the high frequency oscillations that would otherwise dominate the dynamic response following impact. The graphs below, Figures 40 and 41, depict the results that were obtained for the sternum and spinal accelerations with the muscle removed from the Kevlar and CBA plate case.

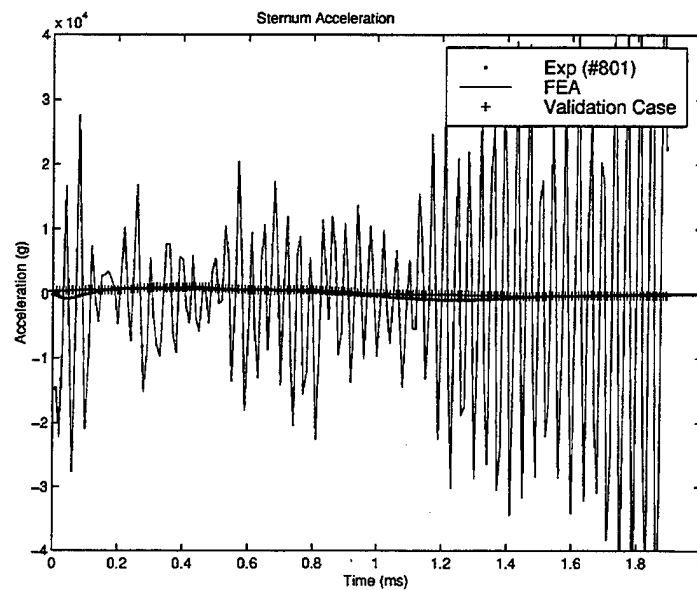


Figure 40: Sternum Acceleration. Graphs of Experimental Data (Exp. (#801)), DYNA3D Results for Model without Muscle (FEA), and DYNA3D Results from First Validation Study (See Section A-1). After Ref. [13].

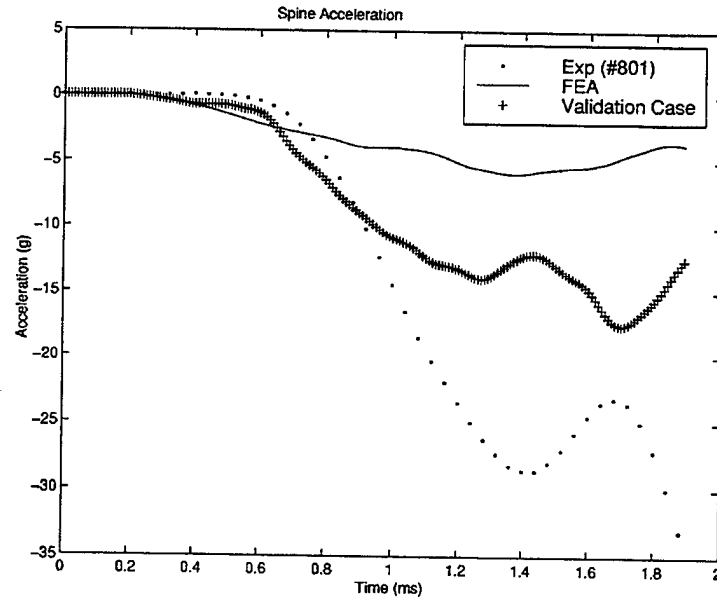


Figure 41: Spinal Acceleration. Graphs of Experimental Data (Exp. (#801)), DYNA3D Results for Model without Muscle (FEA), and DYNA3D Results from First Validation Study (See Section A-1). After Ref. [13].

Another important element in the construction of a viable model was the dampers between the muscles and the ribs. Although they were modeled as separate elements in the model, the dampers and the muscles, combined, were both required to accurately model the viscoelastic behavior of human skin and muscle. The majority of the damping occurred in the muscles themselves, as depicted in Figure 40, but the dampers were also required to ensure the correct behavior in the model, as evidenced in the following graphs. The graphs depict the DYNA3D results for a model without the damping discrete elements. Note that the trough depicted in the sternum acceleration in the validation studies is missing and that the behaviors of the experimental data and the DYNA3D results at the end of the analysis time do not match well. Although the point of

inflection is at the same time in the spinal acceleration comparisons, the magnitudes do not correlate well.

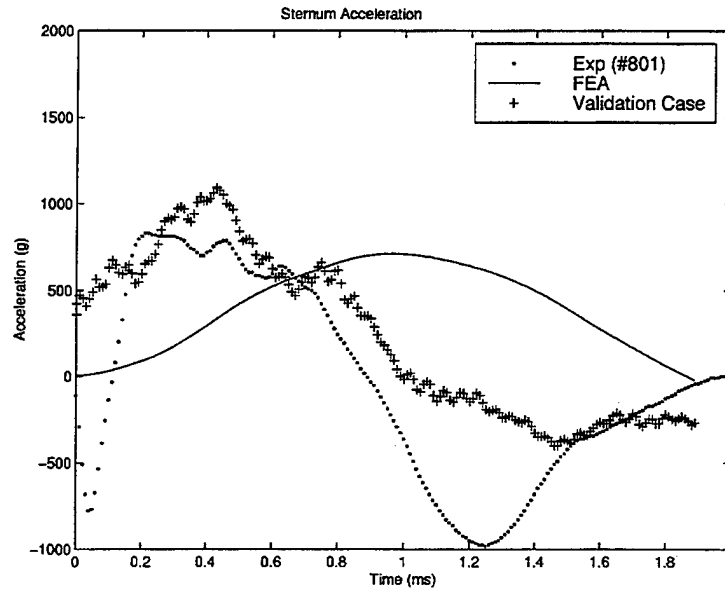


Figure 42: Sternum Acceleration. Graphs of Experimental Data (Exp. (#801)), DYNA3D Results for Model without Dampers (FEA), and DYNA3D Results from First Validation Study (See Section A-1). After Ref. [13].

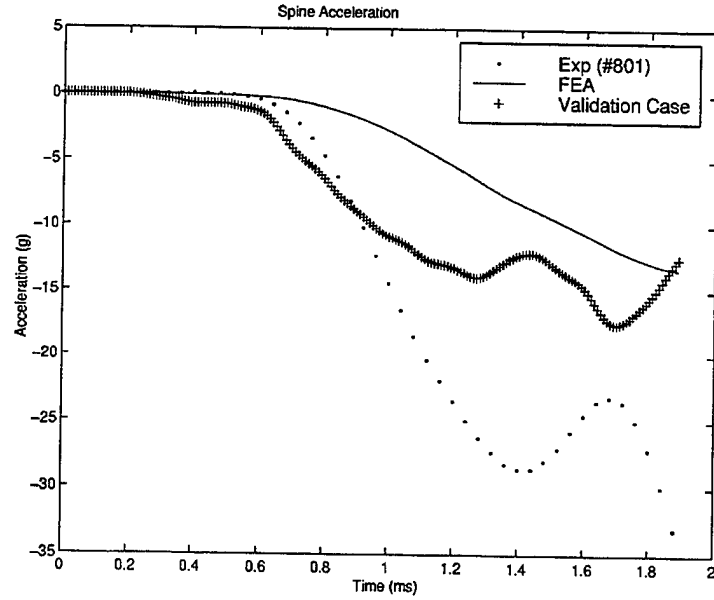


Figure 43: Spinal Acceleration. Graphs of Experimental Data (Exp. (#801)), DYNA3D Results for Model without Dampers (FEA), and DYNA3D Results from First Validation Study (See Section A-1). After Ref. [13].

The Young's Modulus of the muscle was also varied to determine its effect on the biomechanical behavior of the thorax model. In the following case, the Young's Modulus was increased by a factor of five from its original value. This increase in the modulus leads to an increase in the speed of sound calculated for the model according to the following equation:

$$V_s = \sqrt{\frac{E}{\rho}}$$

V_s = Speed of sound
 E = Young's Modulus
 ρ = Density

The increase in the speed of sound results in an increase in frequency response for the model as illustrated below in Figures 44 and 45. Thus, the locations for the first peak and

trough in the sternum acceleration data are not the equivalent. Additionally, the change in the Young's Modulus also increases the magnitude of the first peak predicted by DYNA3D. There are no notable changes noticed in the behavior of the spine with this change in muscle Young's Modulus.

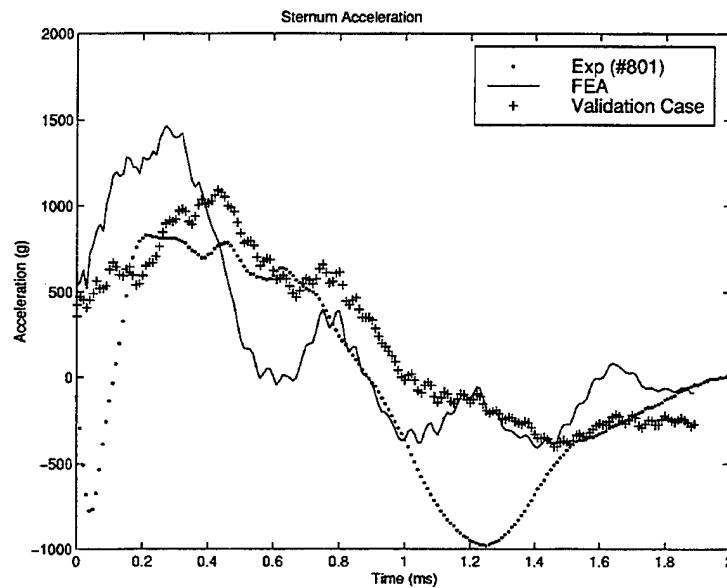


Figure 44: Sternum Acceleration. Graphs of Experimental Data (Exp. (#801)), DYNA3D Results for Model with Muscle Young's Modulus increased by five times (FEA), and DYNA3D Results from First Validation Study (See Section A-1). After Ref. [13].

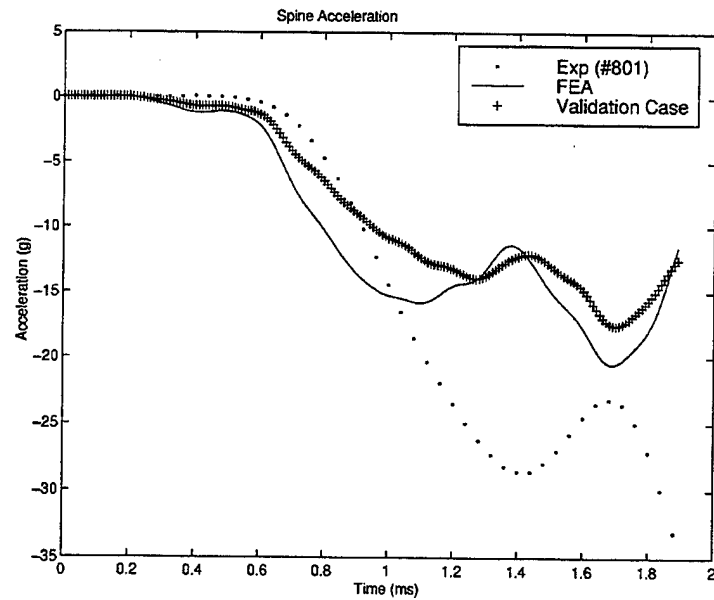


Figure 45: Spinal Acceleration. Graphs of Experimental Data (Exp. (#801)), DYNA3D Results for Model with Muscle Young's Modulus increased by five times (FEA), and DYNA3D Results from First Validation Study (See Section A-1). After Ref. [13].

A significant response was also noted for an increase in the Young's Modulus of the sternal articular cartilage. Due to the direct contact between the vest and the sternum via the muscle, a ten-fold increase in the Young's Modulus of the articular cartilage does not have any effect on the acceleration of the sternum. However, because of the connection of the sternum to the ribs through the articular cartilage, the change in the Young's Modulus does affect the response of the spine as illustrated in Figure 47 below. Note that the point of inflection has advanced from approximately 0.7 milliseconds to 0.2 milliseconds. Additionally, the change in Young's Modulus introduced several new local maxima and minima in the predicted acceleration of the spine.

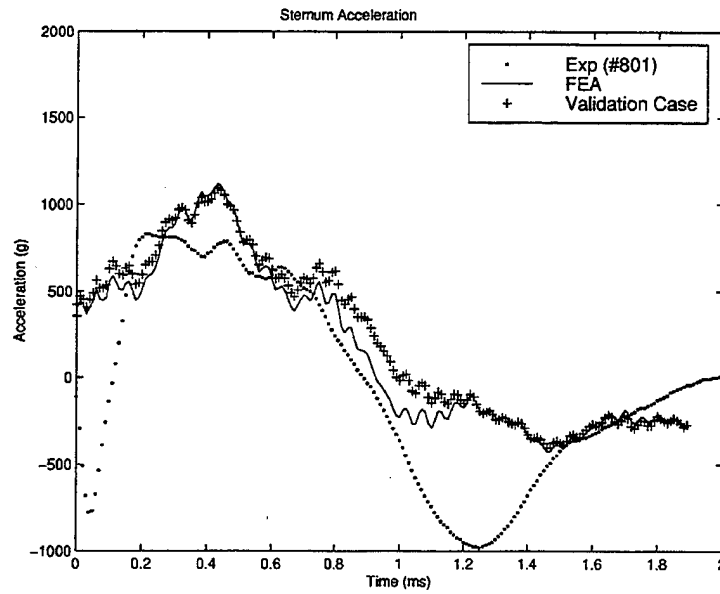


Figure 46: Sternum Acceleration. Graphs of Experimental Data (Exp. (#801)), DYNA3D Results for Model with Sternal Cartilage Young's Modulus increased by ten times (FEA), and DYNA3D Results from First Validation Study (See Section A-1). After Ref. [13].

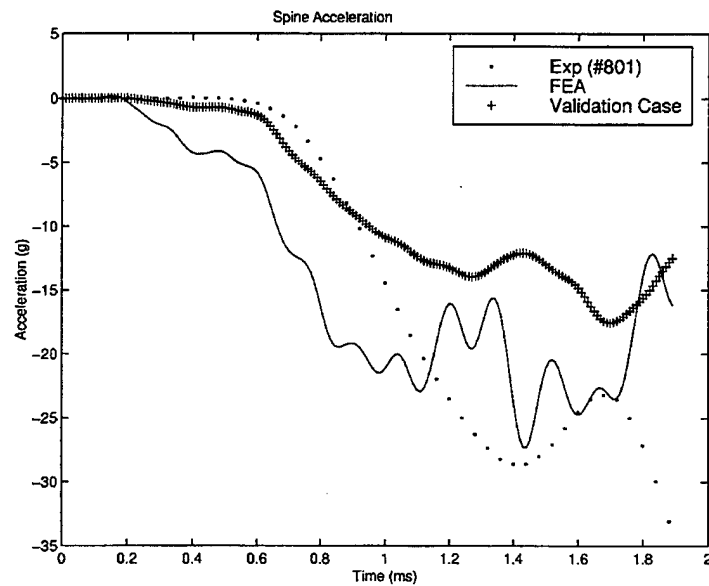


Figure 47: Spinal Acceleration. Graphs of Experimental Data (Exp. (#801)), DYNA3D Results for Model with Sternal Cartilage Young's Modulus increased by ten times (FEA), and DYNA3D Results from First Validation Study (See Section A-1). After Ref. [13].

Another important parameter was deemed to be the contact elements between the muscle and the vest. The contact elements provide a link between these two independent objects. Without the contact elements, the vest would move with rigid body motion and not interact with the thorax at all. In this case, the contact elements immediately between the sternum and the vest were removed, while those surrounding the sternum were left in place. The resulting response in the sternum (see Figure 48) indicates that the motion is directly dependent upon the direct transfer of force from the vest to the sternum. Thus, without the contacts to help in this transfer, the behavior in both the sternum and the spine is altered significantly. Note that the magnitude of the predicted response at the first peak in the sternum acceleration has decreased from the standard case and that the trough has disappeared. In addition, the behaviors at the end of the analysis period deviate with the predicted response indicating a constant decrease in acceleration and the experimental results depicting a return to zero. Also, observe that the spinal accelerations (Figure 49) are not effected by this change in the model. This suggests that a significant path of force propagation influencing the behavior of the spine comes directly from the muscle attached to the lateral edges of the thorax.

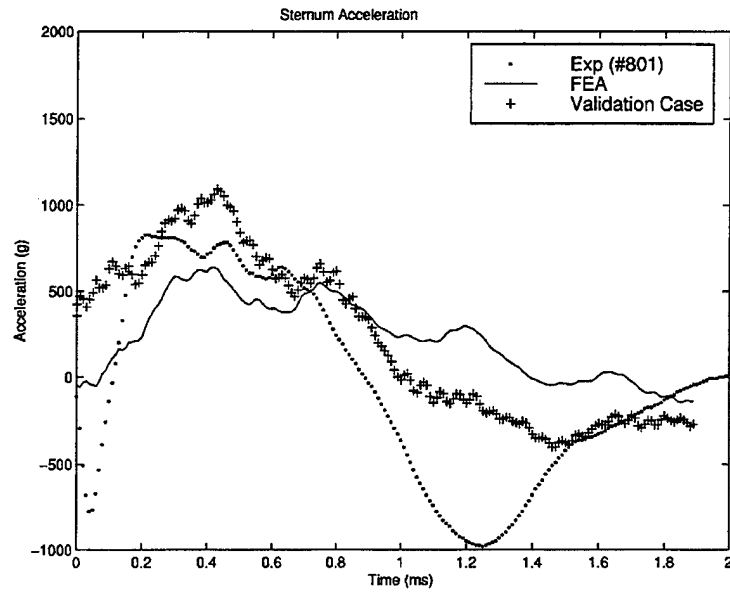


Figure 48: Sternum Acceleration. Graphs of Experimental Data (Exp. (#801)), DYNA3D Results for Model without Contact Elements (FEA), and DYNA3D Results from First Validation Study (See Section A-1). After Ref. [13].

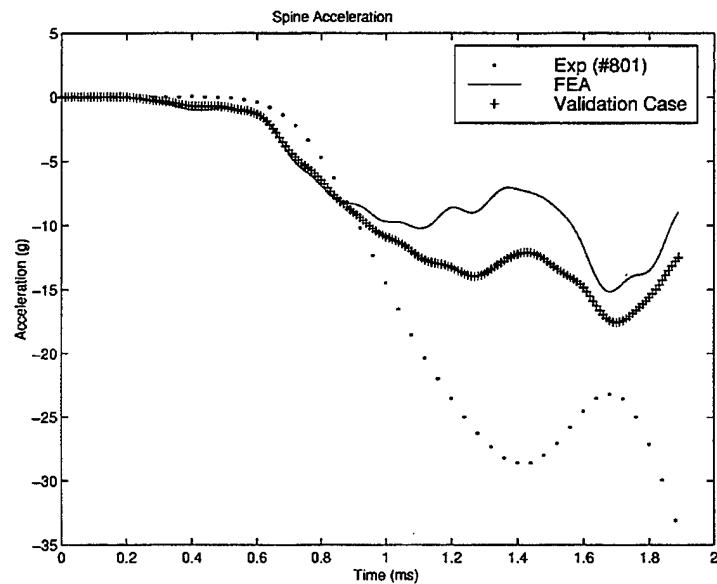


Figure 49: Spinal Acceleration. Graphs of Experimental Data (Exp. (#801)), DYNA3D Results for Model without Contact Elements (FEA), and DYNA3D Results from First Validation Study (See Section A-1). After Ref. [13].

The properties of the materials of the body armor vest were also investigated. The densities of both Kevlar and the CBA plate were increased to determine their effect on the response of the thorax. Both the spinal and sternum accelerations (see Figure 50 and Figure 52) were decreased in peak magnitude and frequency. In addition, the trough observed in the validation study is not observed in either case reported here. The frequency effect can be attributed to the speed of sound equation reported above. The magnitude effect is dependent upon simple Newtonian mechanics. Since the force remains constant and the mass increases due to the increase in density, the acceleration must go down. Due to the decrease in force propagated to the anterior thorax by the vest, the consequent magnitude of the response in the spine is also decreased (see Figure 51 and Figure 53); however, the time of the point of inflection does not change. This is consistent with the results obtained from the parametric study. The point of inflection in the spine is dependent upon the material properties of the elements that directly transfer this force. Since the properties varied in these cases are not directly in this path of force propagation, there is no effect on the time of the point of inflection.

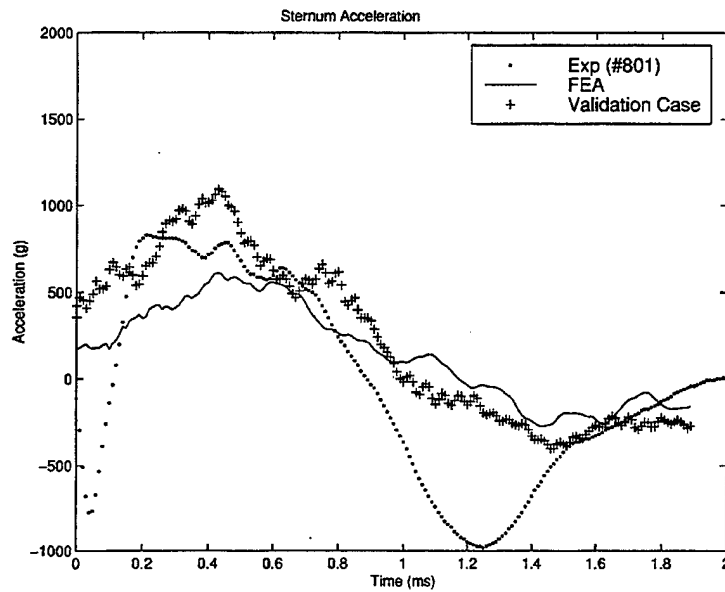


Figure 50: Sternum Acceleration. Graphs of Experimental Data (Exp. (#801)), DYNA3D Results for Model with Kevlar Density increased five times (FEA), and DYNA3D Results from First Validation Study (See Section A-1). After Ref. [13].

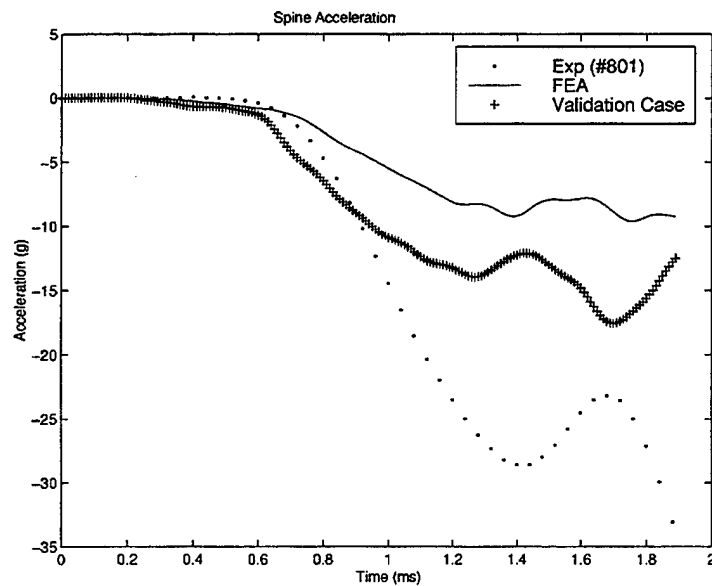


Figure 51: Spinal Acceleration. Graphs of Experimental Data (Exp. (#801)), DYNA3D Results for Model with Kevlar Density increased five times (FEA), and DYNA3D Results from First Validation Study (See Section A-1). After Ref. [13].

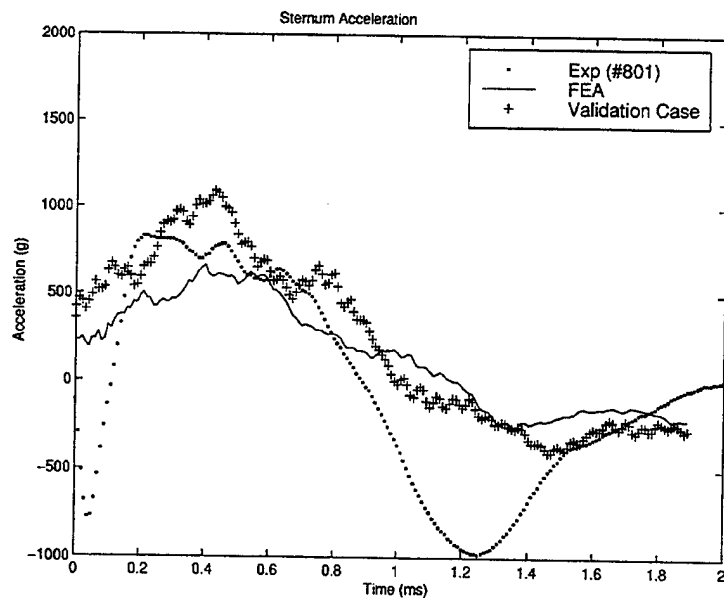


Figure 52: Sternum Acceleration. Graphs of Experimental Data (Exp. (#801)), DYNA3D Results for Model with CBA Plate Density increased five times (FEA), and DYNA3D Results from First Validation Study (See Section A-1). After Ref. [13].

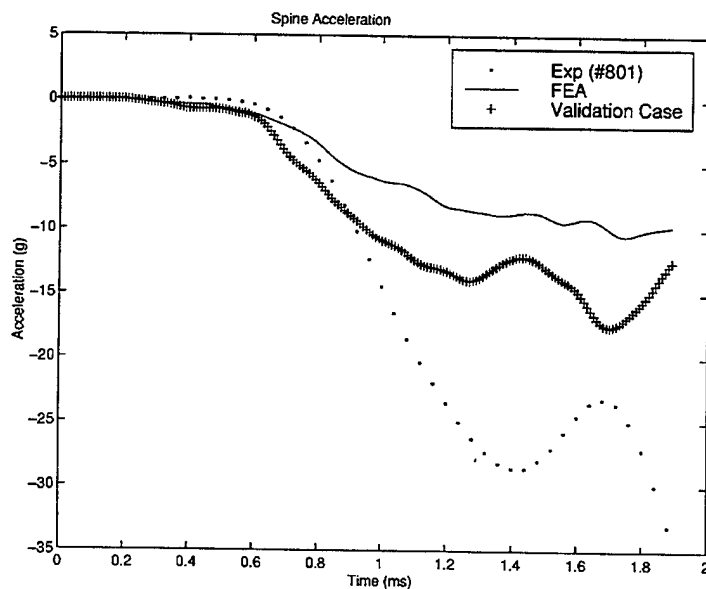


Figure 53: Spinal Acceleration. Graphs of Experimental Data (Exp. (#801)), DYNA3D Results for Model with CBA Plate Density increased five times (FEA), and DYNA3D Results from First Validation Study (See Section A-1). After Ref. [13].

In order to understand the effect of the size of the individual on the effectiveness of the body armor, the thorax dimensions were increased by 25%. The vest size was kept constant to eliminate that as a variable. The response of the sternum demonstrates a similar response as that of the increased density of the CBA plate or Kevlar with the corresponding lack of a trough and decreased magnitude of the first peak. (See Figure 54 below.) It is thought that this is due to the increase in size of the sternum itself. As the sternum size increases, it becomes more massive. Thus, it will have a smaller acceleration due to Newton's Second Law. Additionally, the decreased magnitude of the response in the spine can be attributed to similar effects. Due to the increase in body size, the distance of stress propagation through the ribs plus the increased mass of the ribs themselves limit the magnitude of the response in the spine. In addition, the increased size of the thorax creates a longer path of propagation for the force to reach the spine. This results in a later point of inflection (1.2 milliseconds versus 0.7 milliseconds) than that noted in the validity studies. (See Figure 55 below.)

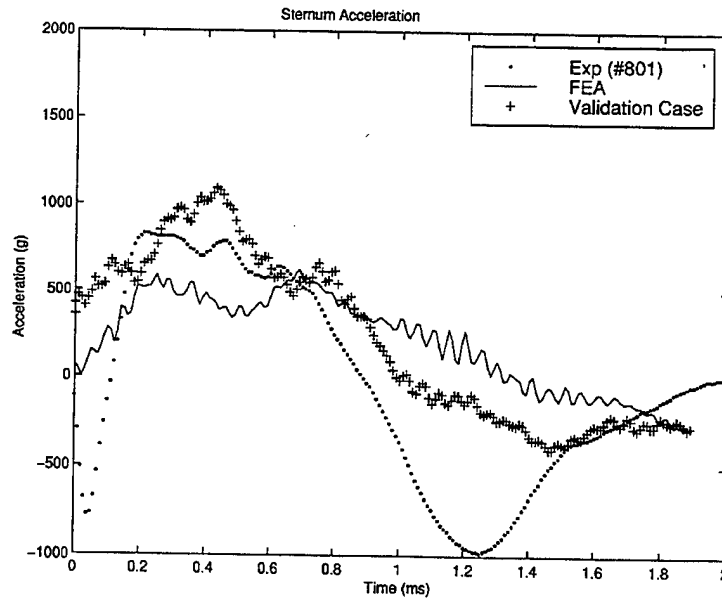


Figure 54: Sternum Acceleration. Graphs of Experimental Data (Exp. (#801)), DYNA3D Results for Model with Thorax Dimensions increased 25% (FEA), and DYNA3D Results from First Validation Study (See Section A-1). After Ref. [13].

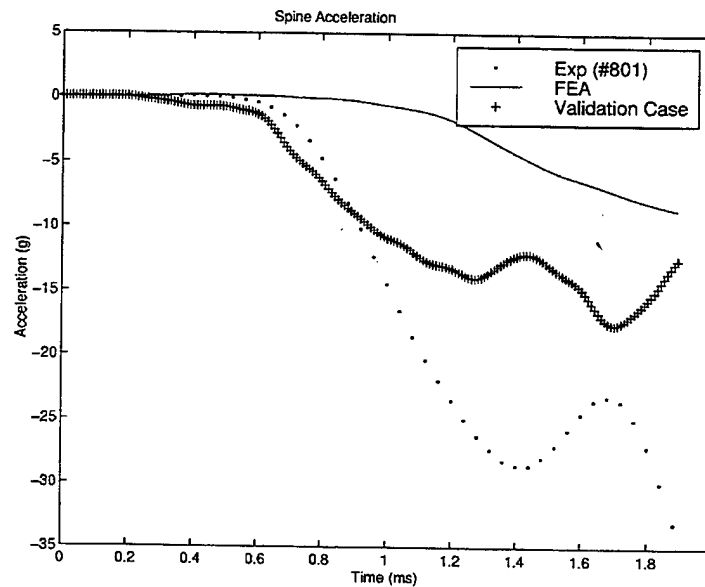


Figure 55: Spinal Acceleration. Graphs of Experimental Data (Exp. (#801)), DYNA3D Results for Model with Thorax Dimensions increased 25% (FEA), and DYNA3D Results from First Validation Study (See Section A-1). After Ref. [13].

V. CONCLUSIONS/RECOMMENDATIONS

A. CONCLUSIONS

The research described in this thesis was undertaken to investigate the construction of a finite element model to model the effects of impact loads to a human thorax wearing a body armor system. The overriding goal for this study was to obtain a viable model of the human thorax that could be used to adequately predict the accelerations experienced by a body subjected to impact by a projectile, namely a bullet. After construction of the model, two studies were undertaken. The first was to prove the viability of the model. The results demonstrated that the model adequately matched the available experimental data for both load cases imposed. As such the model was deemed to be viable, and a parametric study was then undertaken to determine the critical components of the model. This analysis determined that the damping properties of the muscles were the most important element in the model. Hughes [Ref. 18] had presented a model for the prediction of human thorax response to impact loads; however, by not including this essential element, his model suffered from oscillations and, therefore, lacked the quantitative predictive power demonstrated through this study. The inclusion of the musculature into the finite element model provided for the good correlation between the finite element analysis (FEA) results and the experimental data.

Additional elements were deemed significant in establishing the correct model of the thorax, including the Young's Moduli of the sternum articular cartilage and the bones and the initial gap between the vest and the sternum. The parametric study demonstrated

that the method of stress propagation from the body armor system to the sternum was direct, via the layer of muscle over the sternum and consequently through the ribs and sternochondral cartilage to the rest of the body. Therefore, variations in the stiffness of these elements, namely alterations in the Young's Modulus, resulted in significantly different responses in both the sternum and the spine. Additionally, this method of stress propagation was dependent upon the initial gap between the sternum and the bulletproof vest. Thus, removal of this space resulted in a different method of force transference, leading to a different predicted behavior.

The final consideration in the construction of this model was with the material properties chosen for the body armor system itself. One of the experimental setups used by DeMaio relied on a Kevlar vest with a Concealable Body Armor (CBA) ceramic plate to prevent bullet penetrations. Due to the proprietary nature of these materials, it was difficult to obtain accurate properties; however, reasonable values were chosen. The parametric study demonstrated that the densities of these materials are paramount to the behavior of the human thorax under impact. Thus, use of another body armor system for protection could have significant effects on the responses of the body to impacts.

B. RECOMMENDATIONS

Although this model has excellent predictive powers, several refinements can be made.

- This model lacks the soft inner tissues of the thoracic cavity. It is possible that there is an element of stress propagation through the soft tissues, such as

the heart and lungs, into the spine, though the majority will likely be found to be through the skeletal structure of the thorax. The inclusion of these tissues is unlikely to radically change the responses predicted for the spine, but their inclusion is important in creating a complete thoracic model. Additionally, the various ligaments, tendons, and minor muscles of the thorax are not included in this model. These soft tissues are more likely to directly influence the response predicted by this model as they regulate the method by which forces are transferred between the various elements of the thoracic skeleton. As such, they are important elements to be included in a refined model of the human thorax.

- A perpetual need in biomechanical modeling has been adequate research into the material properties of the human body, including densities and Young's moduli of the bones and cartilage. Unfortunately, there exists a dearth of reliable data in this area. Previous sample sizes in existing studies have been too small to adequately obtain average values for the population at large. Additionally, no studies have been discovered that examined the material properties of muscle in detail. These are important aspects in predicting the correct behavior for the thorax upon impact and serious consideration should be given to further research in that area.
- Due to computer processor limitations, the number of elements in the thorax were kept to a minimum necessary to adequately model the structure.

However, increasing the number of elements could further refine the predicted behaviors of the biomechanical model.

- Due to the focus of this study on using the experimental data obtained by AFIP for validation, it is important to understand the parameters they used in their study. This includes more investigations into the material properties of the protective body armor, the boundary conditions imposed by their methods, and the exact positions, orientations, and manner in which they secured the instruments to the structures studied.
- A better approximation of the musculature of the anterior facet of the thorax is also necessary. As this study demonstrated, the behavior of the model is intimately linked to the shape and material properties of this muscle tissue. An such, it is important to refine the meshing of the muscle and obtain experimental data, if possible, on the exact geometries.
- Inclusion of a failure mode for the bones is essential to accurately model the responses expected in the human thorax upon impact. Due to the changes in stiffness that occur as a result of a fracture, the mechanism for stress propagation may alter leading to a significantly different prediction for the thorax response.

LIST OF REFERENCES

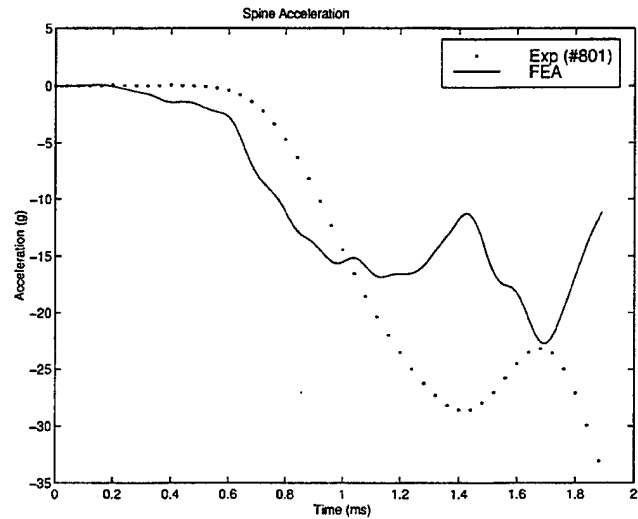
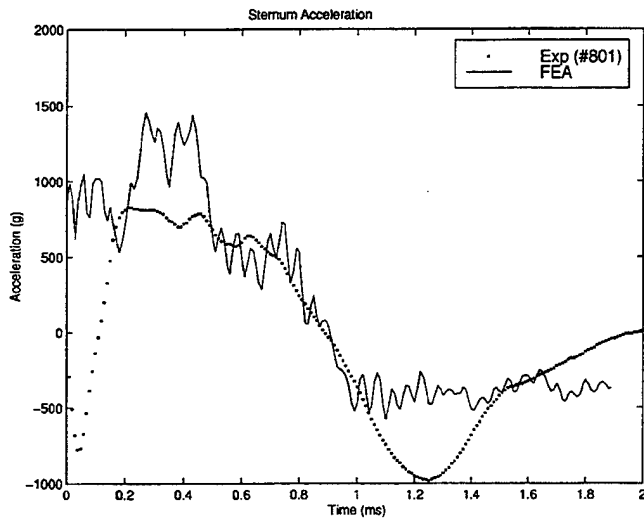
1. Brauer, J. R., (Editor), *What Every Engineer should know about Finite Element Analysis*, 2nd ed., Marcel Dekker, 1993.
2. Cook, R. D., Malkus, D. S., & Plesha, M. E., *Concepts and Applications of Finite Element Analysis*, 3rd ed., John Wiley & Sons, 1989.
3. Huebner, K. H., Thornton, E. A., & Bryom, T. G., *The Finite Element Method for Engineers*, 3rd ed., John Wiley & Sons, 1995.
4. Akin, J., *Finite Element Analysis for Undergraduates*, Academic Press, 1986.
5. Personal Communication between Dr. Richard T. Hart, Chairman, Department of Biomedical Engineering, Tulane University, New Orleans, LA and the author, 1999.
6. Fung, Y.C., *Biomechanics: Mechanical Properties of Living Tissue*, 2nd Ed., Springer-Verlag, New York, 1993.
7. Best, C. H. and Taylor, N. B. *The Human Body: Its Anatomy and Physiology*, 4th Ed., Holt, Rinehart, & Winston, 1963.
8. Gray, H., *Anatomy: Descriptive and Surgical*, 15th ed., Barnes and Noble Books, 1995.
9. Nordin, M. and Frankel, V., *Basic Biomechanics of the Musculoskeletal System*, Williams and Wilkins, 1989.
10. National Law Enforcement and Corrections Technology Center / National Institutes of Justice, "Selection and Application Guide to Police Body Armor," [<http://www.ncjrs.org/txtfiles/169587.txt>], Oct 1998.
11. Encyclopedia Britannica, "Bulletproof Vest," [<http://www.britannica.com/bcom/eb/article/0/0,5716,18305+1+18046,00.html>].
12. Office of Law Enforcement Standards / National Institutes of Justice, "Ballistic Resistance of Police Body Armor: NIJ Standard 0101.03," [<http://www.oles.org/pdf/aaaad.pdf>], April 1987.
13. DeMaio, M., Parks, S., et al., "Biomechanical Evaluation of Chest Body Armor," report, Armed Forces Institute of Pathology (AFIP).

14. Military Standard V50 Ballistic Test for Armor, MIL-STD-622E, January 1987.
15. Cunniff, P., "A Semiempirical Model for the Ballistic Impact Performance of Textile-Based Personnel Armor," *Textile Research Journal*, v. 66, pp. 45-59, Jan 1996.
16. Vinson, J., Zukas, J., "On the Ballistic Impact of Textile Body Armor," *Journal of Applied Mechanics*, v. 42, pp. 263-268, June 1975.
17. Roberts, S. B. and Chen, P. H., "Elastostatic Analysis of the Human Thoracic Skeleton," *Journal of Biomechanics*, v. 3, pp. 527-545, 1970.
18. Hughes, T., *Biomechanical Model of the Human Thorax for Impact Analysis*, Master's Thesis, Naval Postgraduate School, Monterey, California, September 1999.
19. Andriacchi, T., Shultz, A., Belytschko, T., and Galante, J., "A Model for the Studies of the Mechanical Interaction between the Human Spine and Rib Cage," *Journal of Biomechanics*, v. 10, pp. 497-507, 1974.
20. Yogananda, N. and Pintar, F., "Biomechanics of Human Thoracic Ribs," *Journal of Biomechanical Engineering*, v. 120, pp. 100-104, Feb 1998.
21. Lee, K. S., *Biomechanical Response of the Human Body inside a Military Vehicle Exposed to Mine Explosion*, Master's Thesis, Naval Postgraduate School, Monterey, California, March 1999.
22. King, Q. M., *Investigation of Biomechanical Response due to Fragment Impact on Ballistic Protective Helmet*, Master's Thesis, Naval Postgraduate School, Monterey, California, March 1998.
23. Sundaram, S., and Feng, C., "Finite Element Analysis of the Human Thorax," *Journal of Biomechanics*, v. 10, pp. 505-516, 1977.
24. Kolsky, H., *Stress Waves in Solids*, Dover, 1963.
25. Flügge, W., *Viscoelasticity*, Blaisdell Publishing, 1967.
26. Lockett, F. J., *Nonlinear Viscoelastic Solids*, Academic Press, 1972.

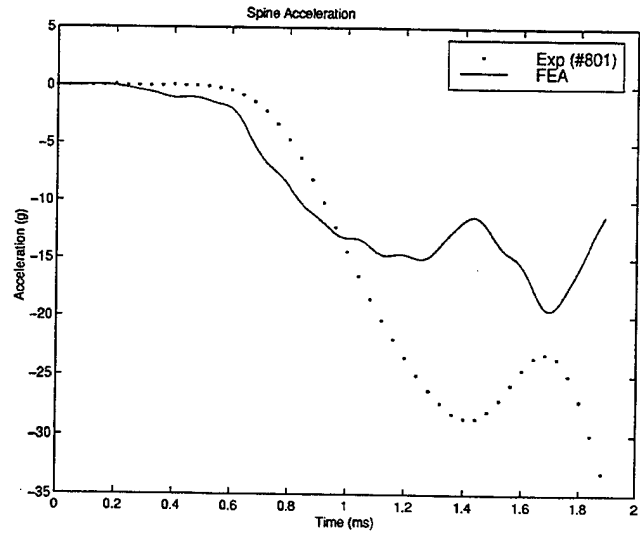
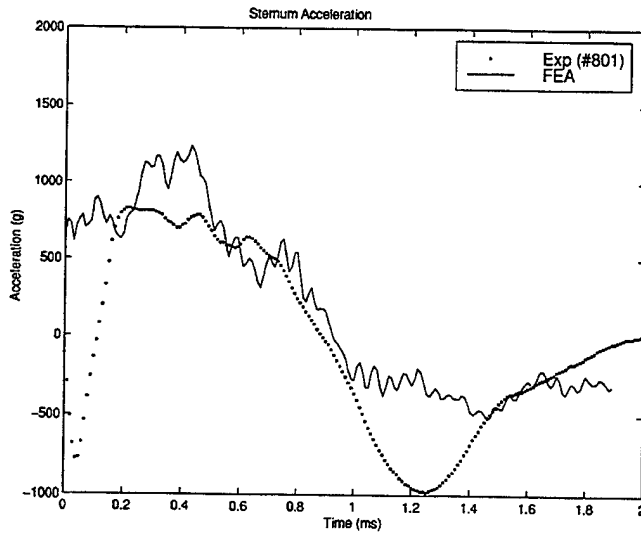
APPENDIX A: PARAMETRIC STUDY RESULTS

In an attempt to understand the effects of the various parameters on the biomechanical response of the thorax, the model parameters were changed individually from the “standard” Kevlar vest and CBA plate model presented above. The results were then compared to those obtained by DeMaio, et al [Ref. 13]. Significant changes between the “standard” case and the results obtained with a parameter changed indicated their importance to the model. The following is a listing of the various parameters that were changed and the results obtained.

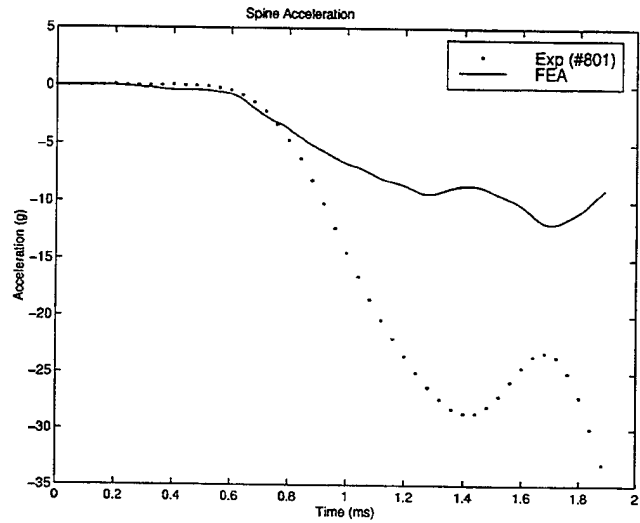
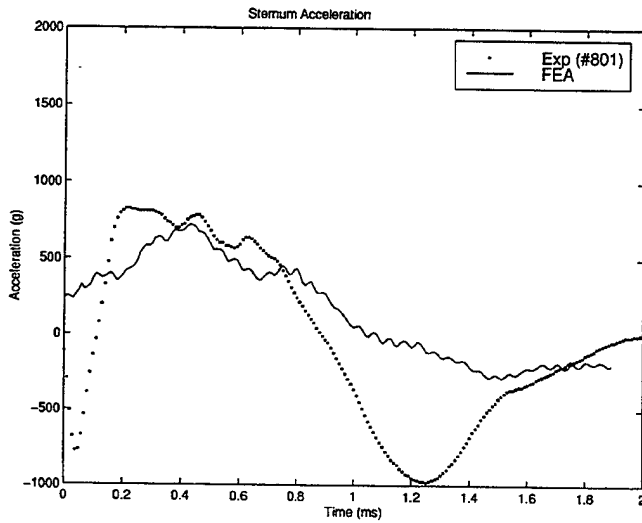
- Damping constant for damping discrete elements increased by four times



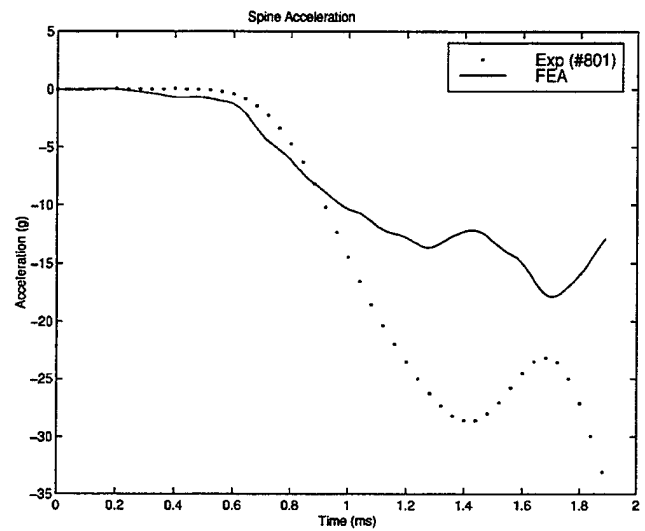
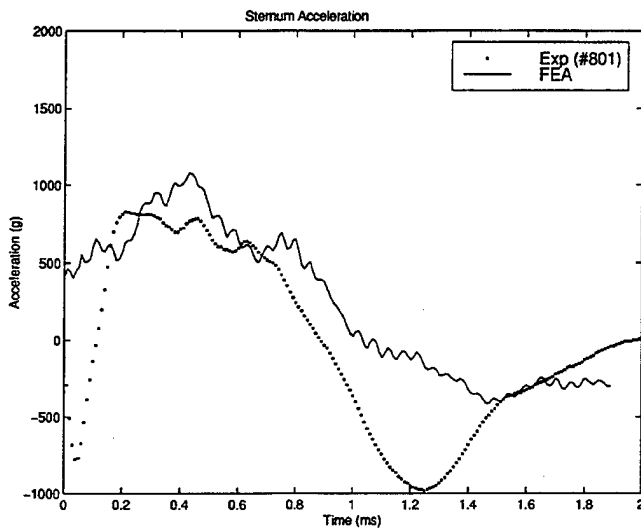
- Damping constant for damping discrete elements increased by two times



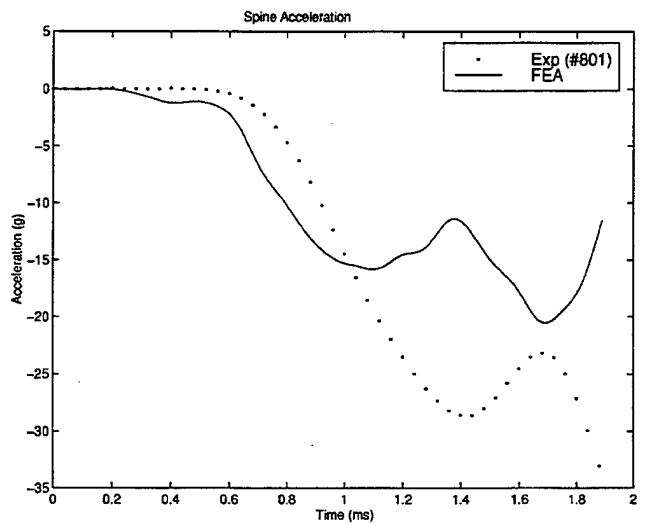
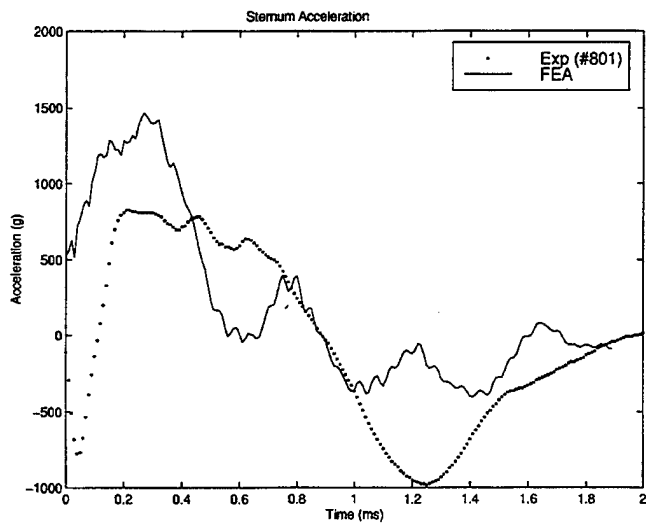
- Damping constant for damping discrete elements decreased by half



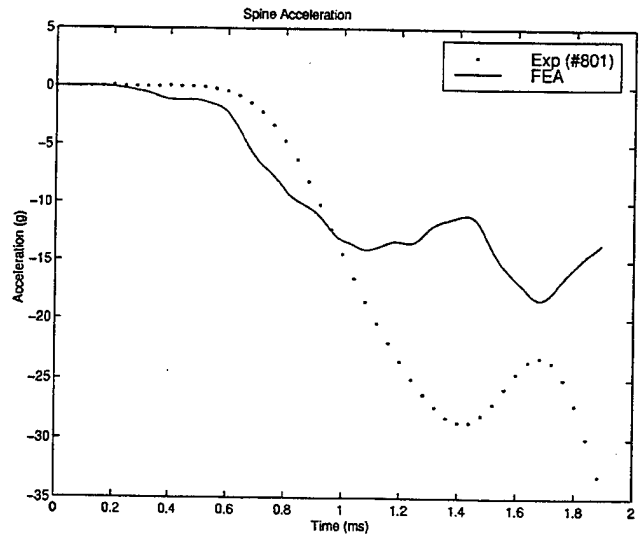
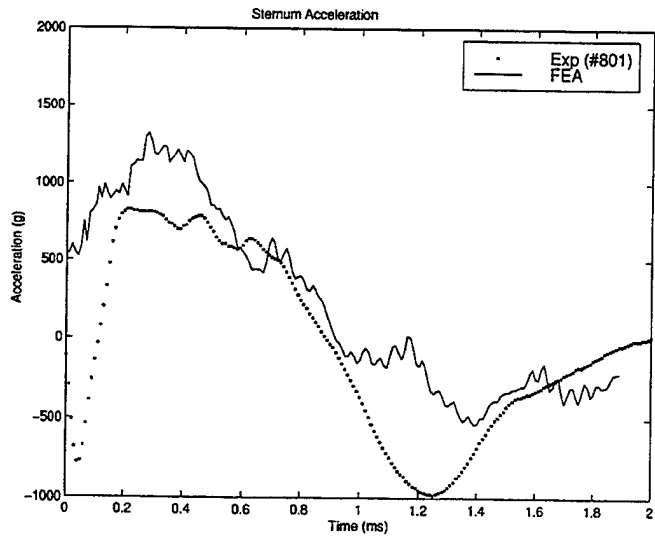
- Muscle material type changed from viscoelastic to elastic



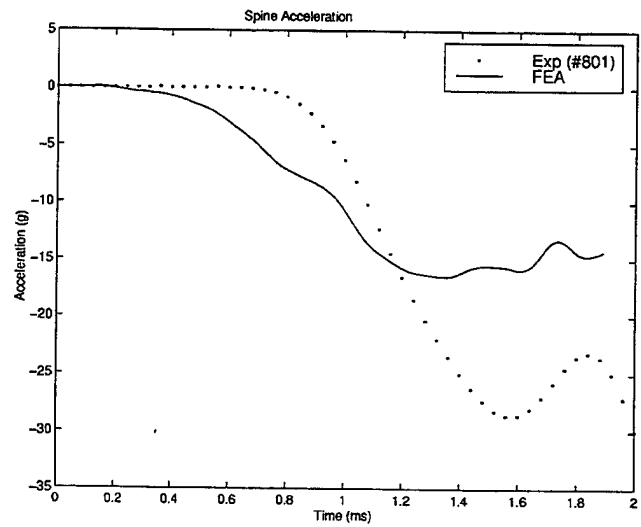
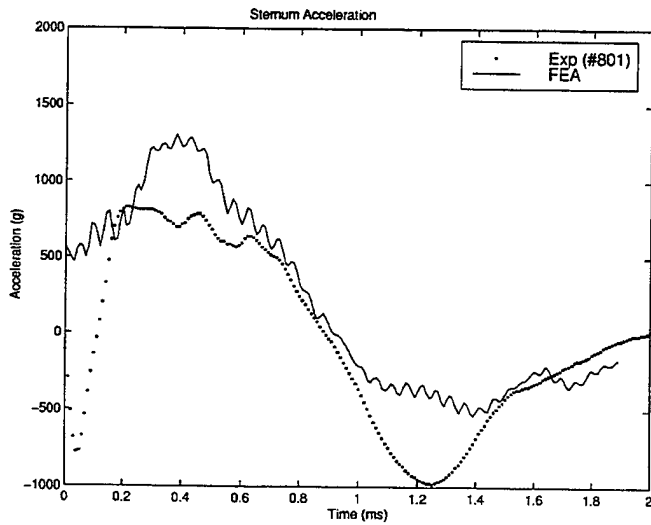
- Muscle Young's Modulus increased five times



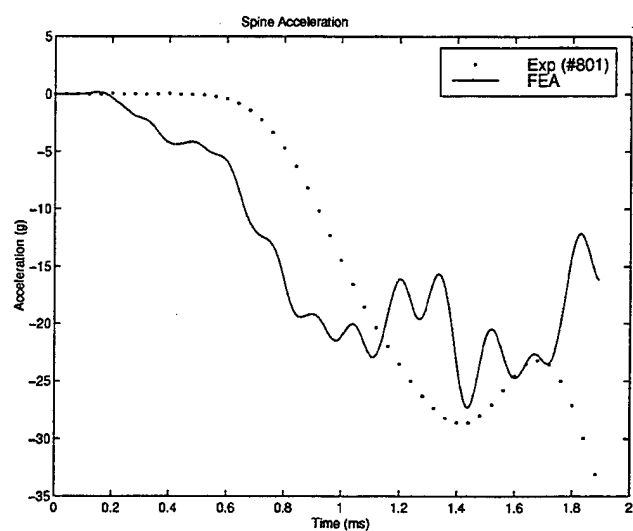
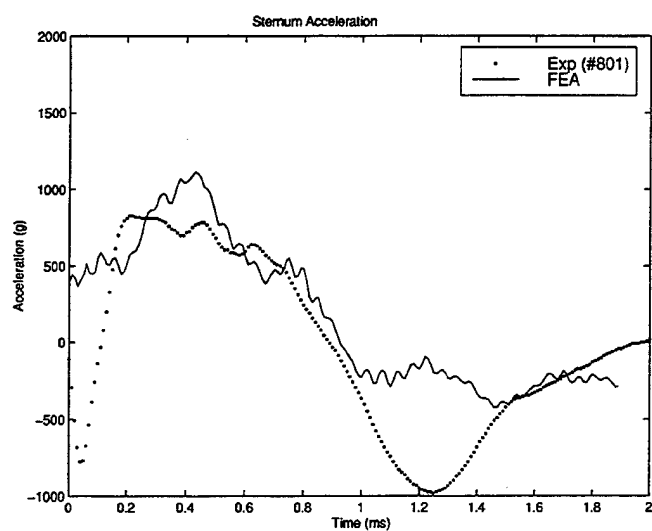
- Muscle density decreased three times



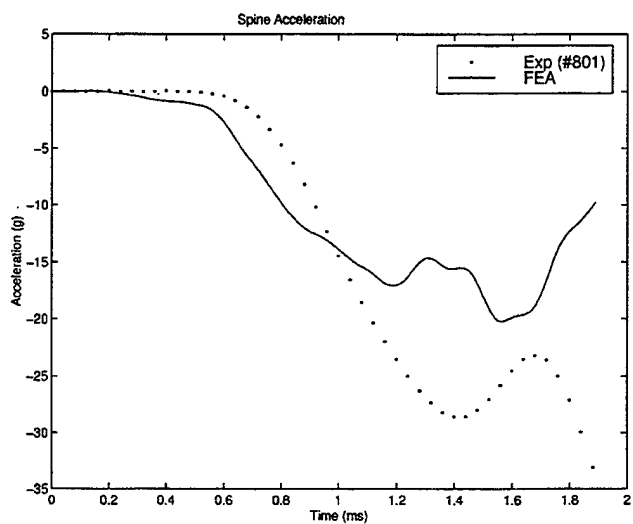
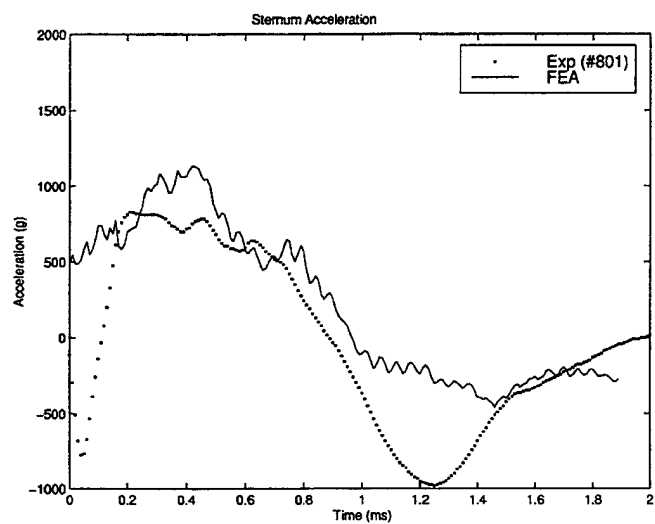
- Sternal articular cartilage density decreased ten times



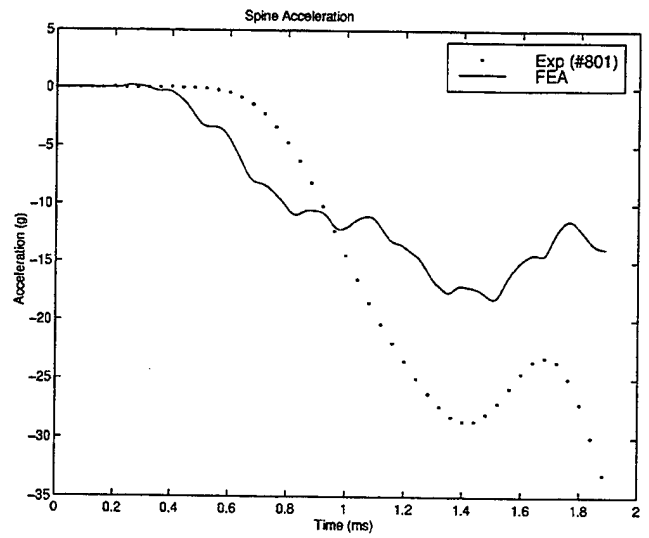
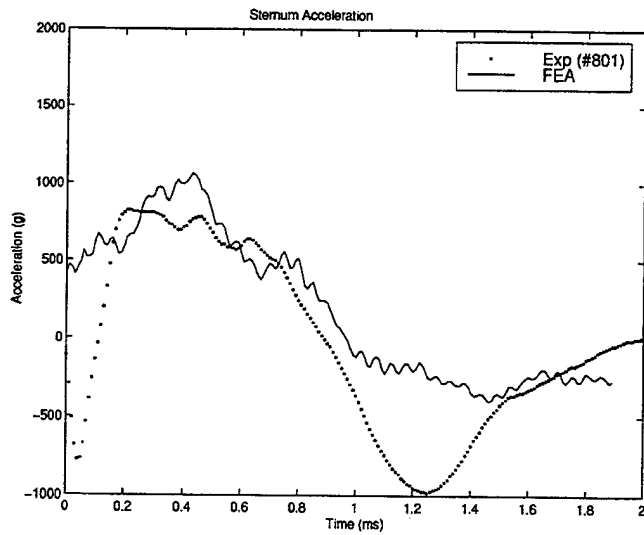
- Sternal articular cartilage Young's Modulus increased ten times



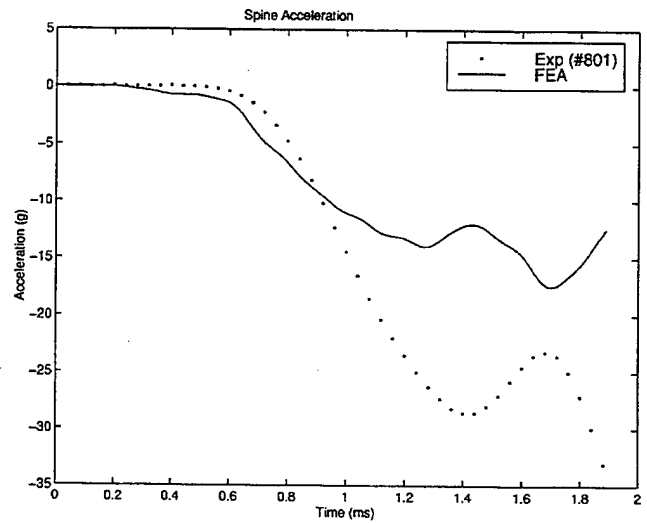
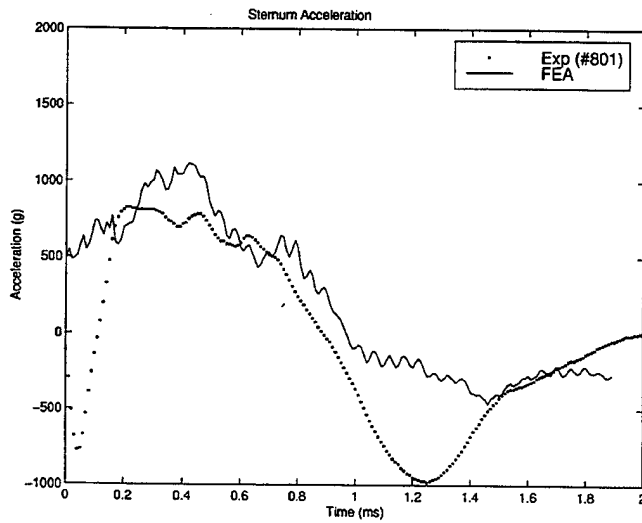
- Thoracic bones' densities set to 800 kg/m^3



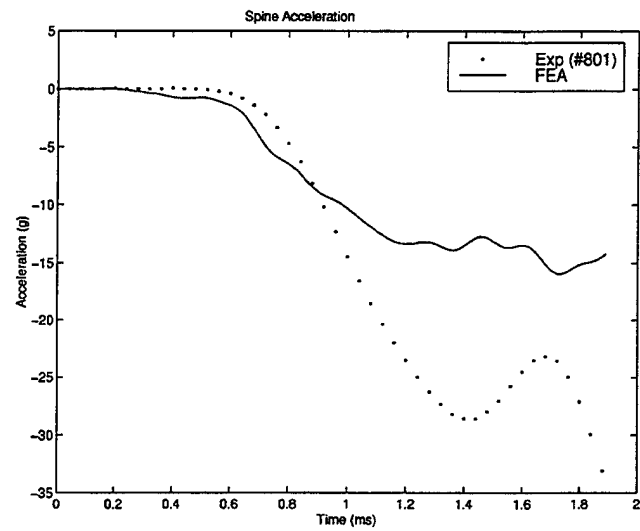
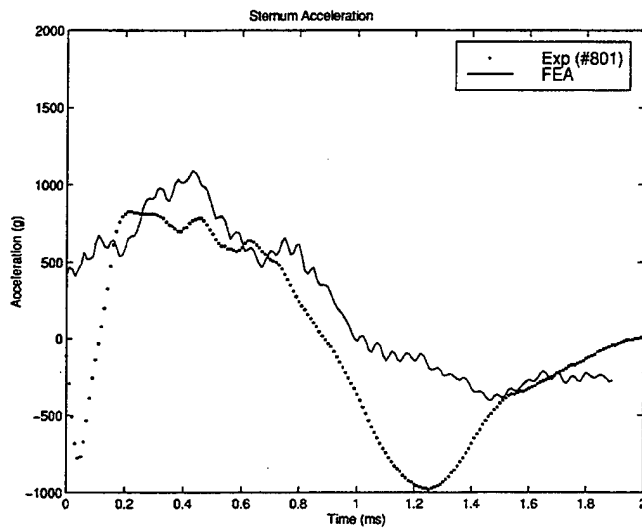
- Thoracic bones' Young's Modulus set to 12.1 GPa



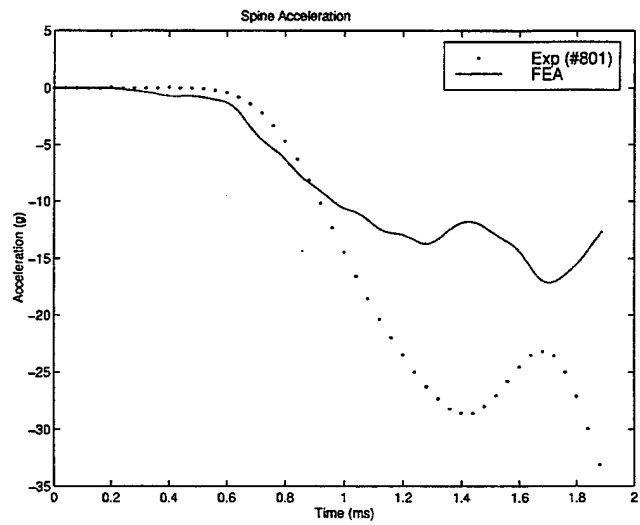
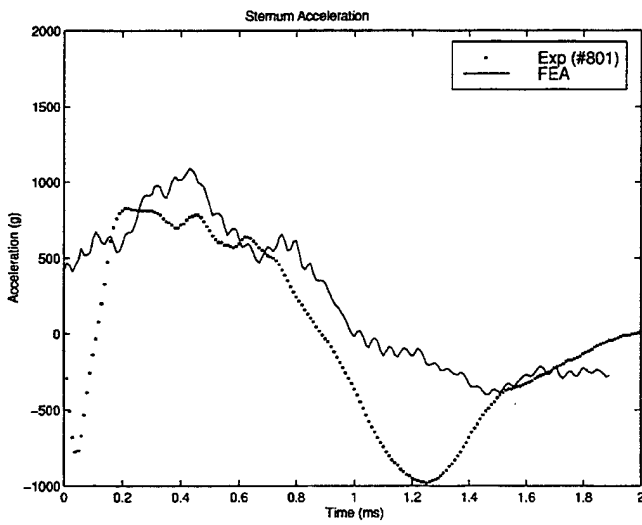
- Sternum bone density decreased 20%



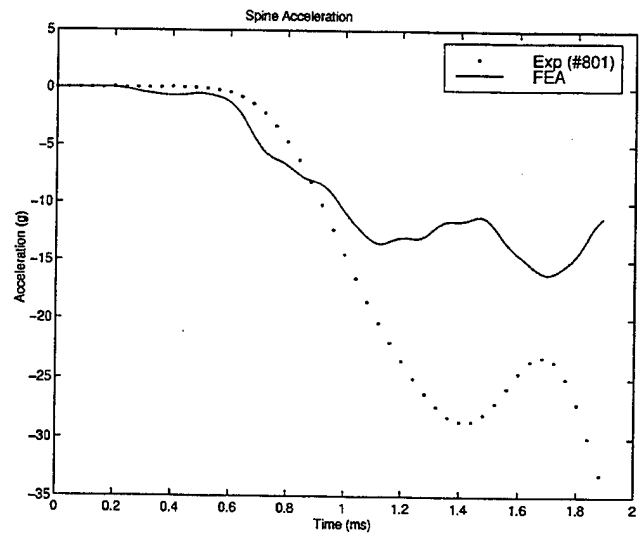
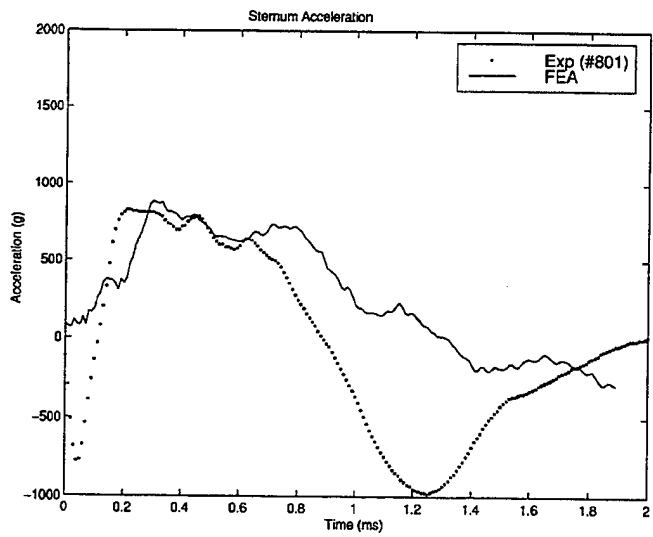
- Intervertebral disc Young's Modulus decreased by ten times



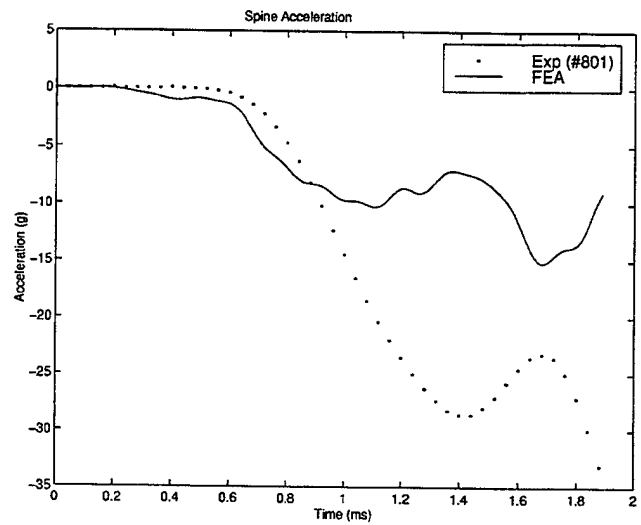
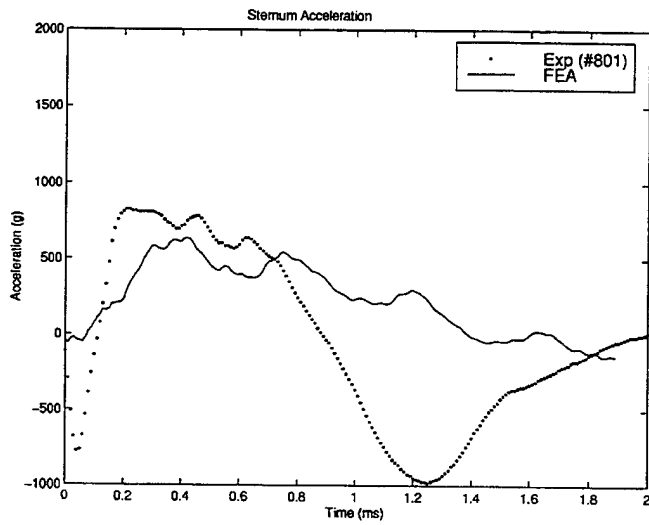
- Intervertebral disc density increased by five times



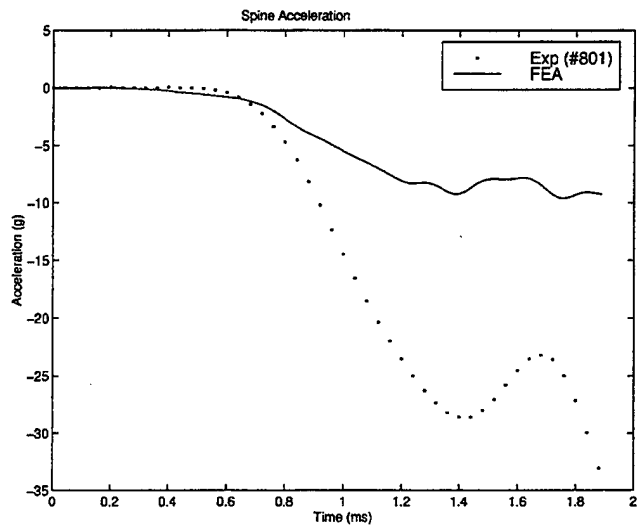
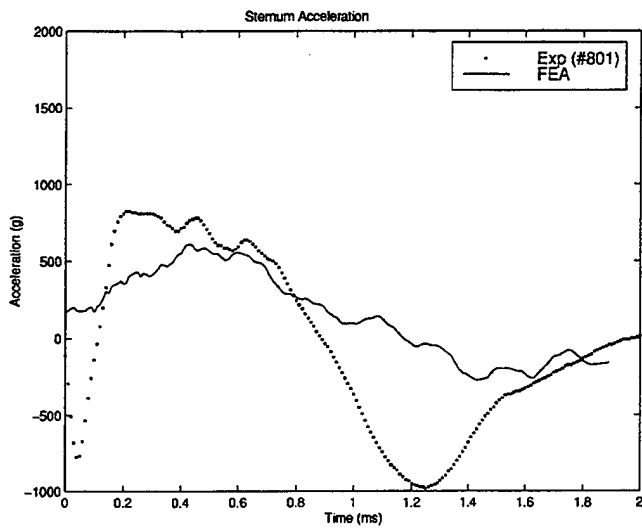
- Initial gap between sternum and vest removed



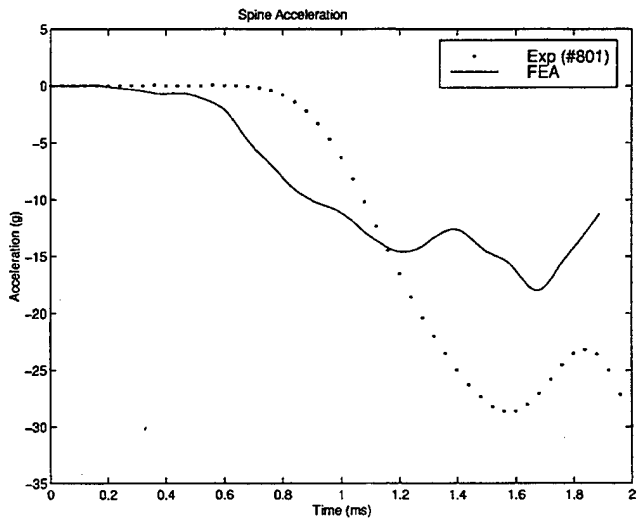
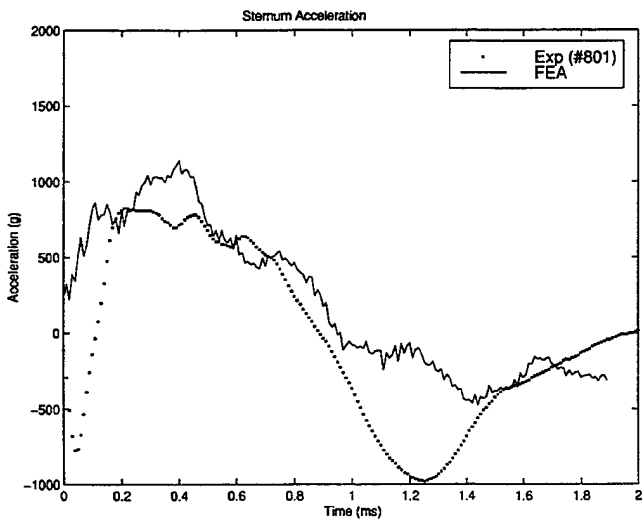
- Contact elements directly between sternum and vest removed



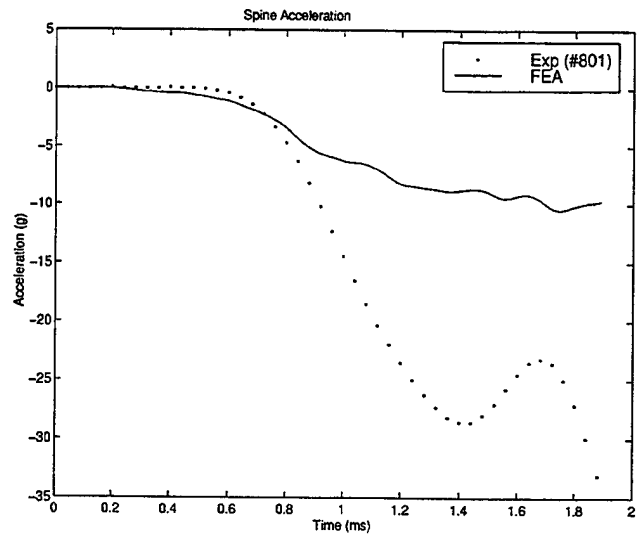
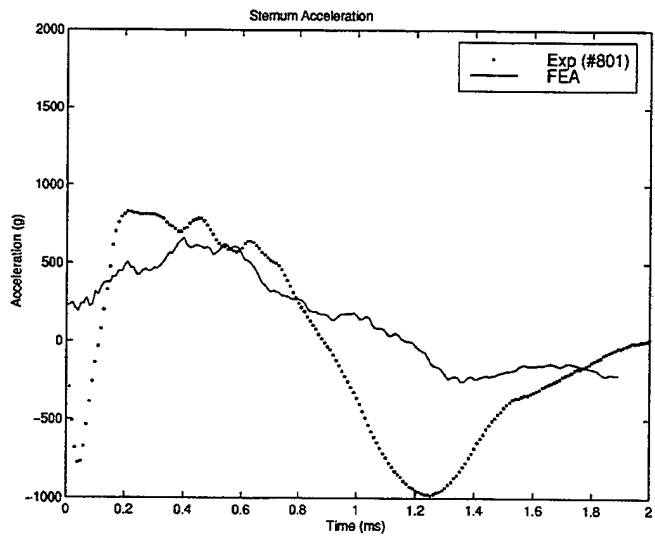
- Kevlar density increased five times



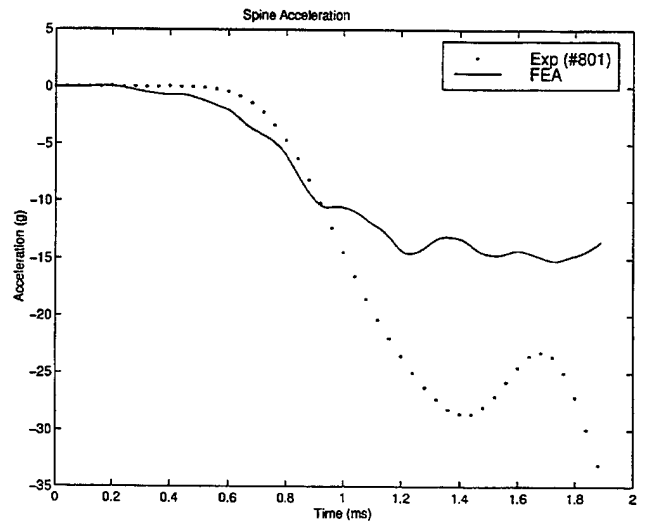
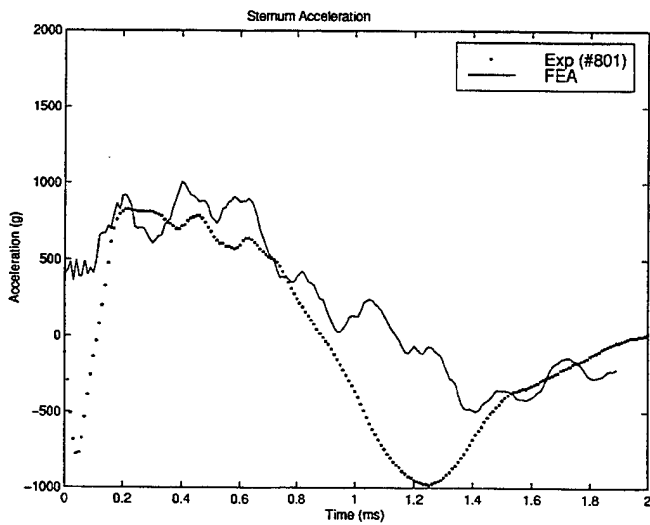
- Kevlar Young's Modulus increased five times



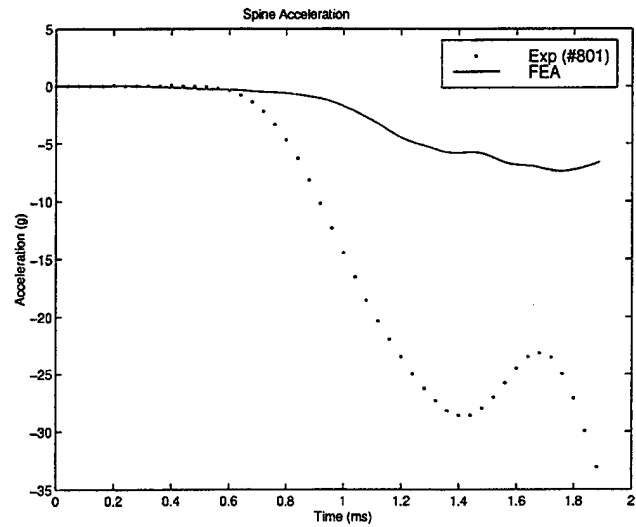
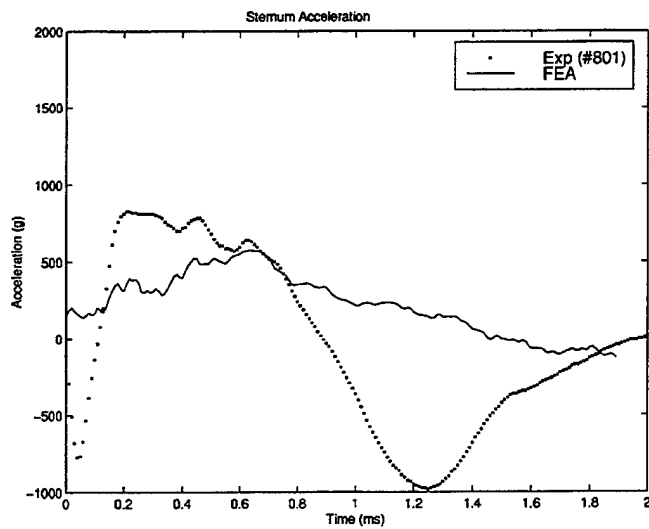
- CBA plate density increased two times



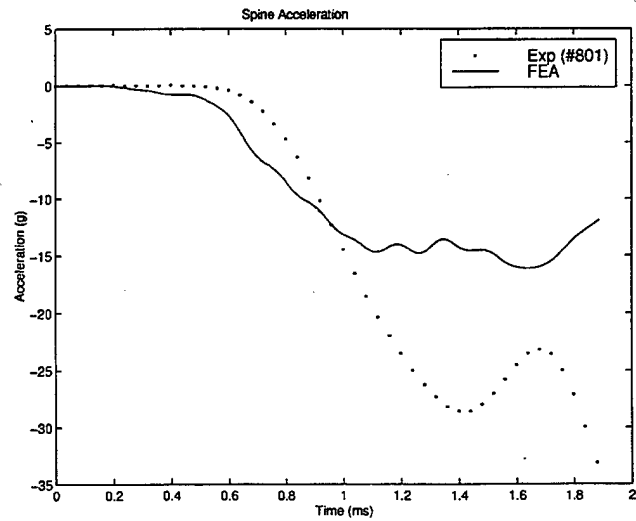
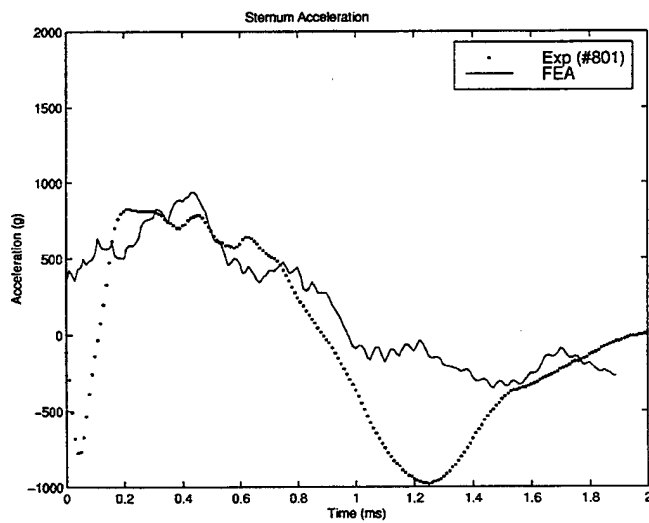
- CBA plate Young's Modulus decreased two times



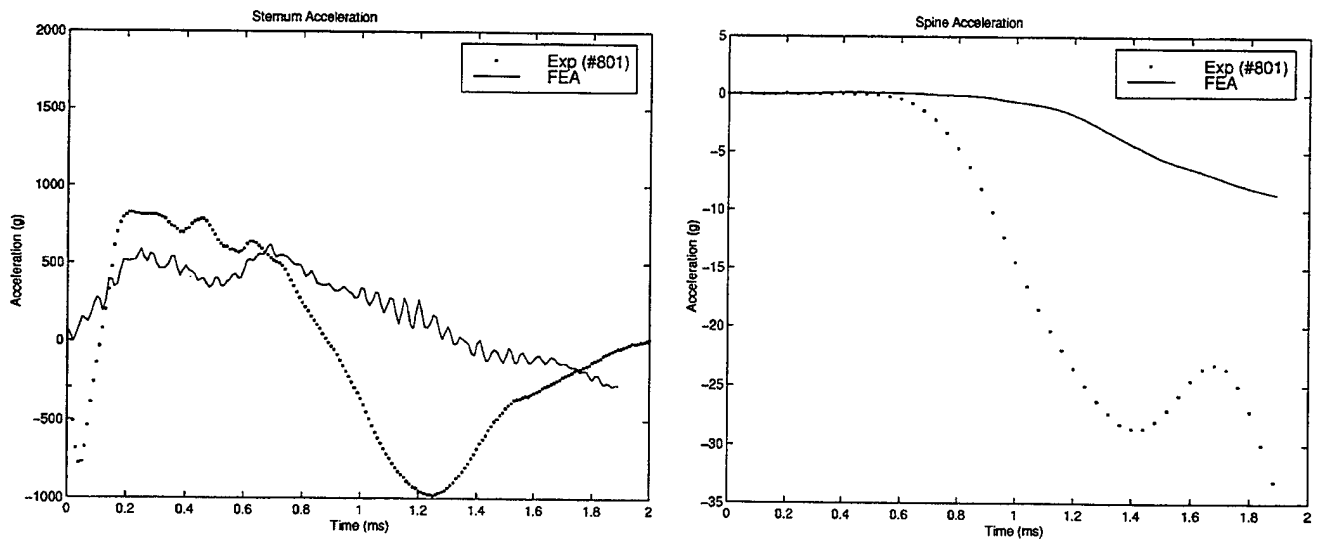
- Thorax and body armor dimensions increased 25%, Body armor thickness kept constant



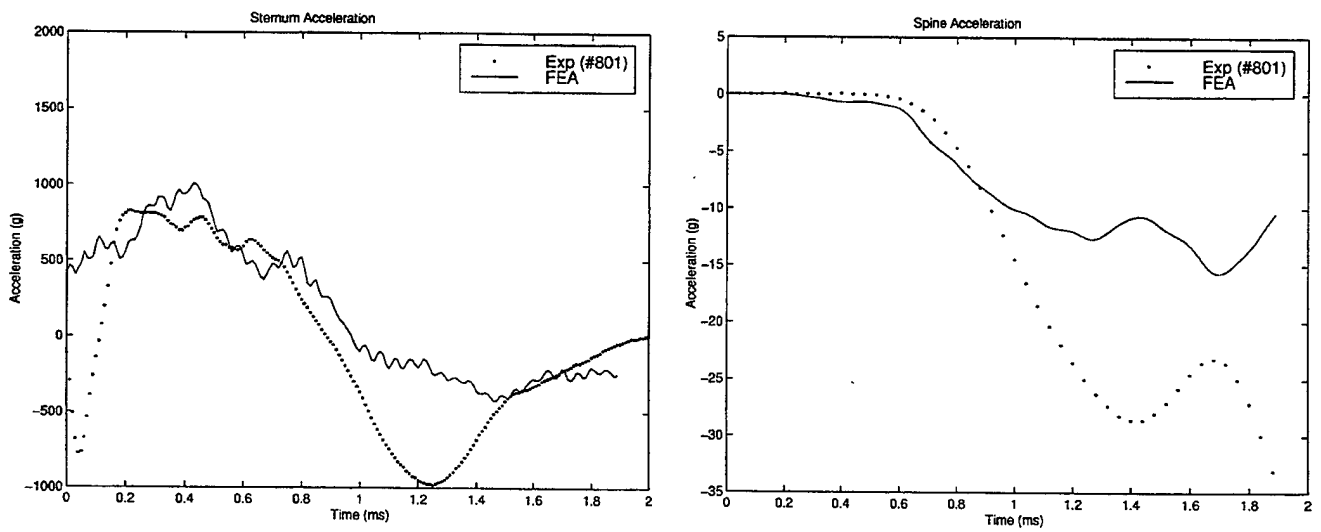
- Rib cross sections increased (diameters increased by 25%)



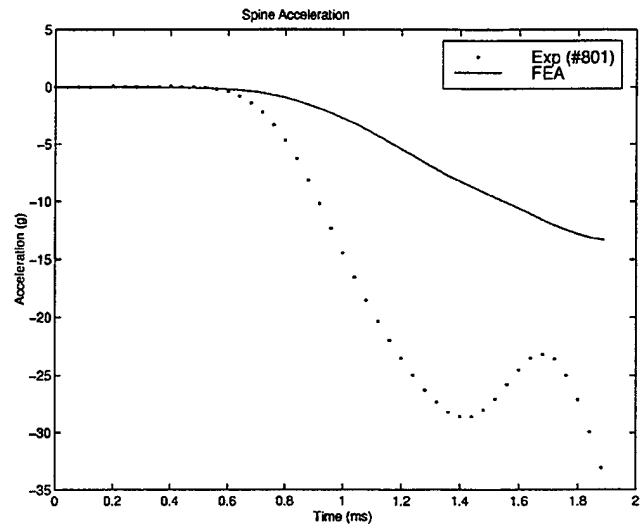
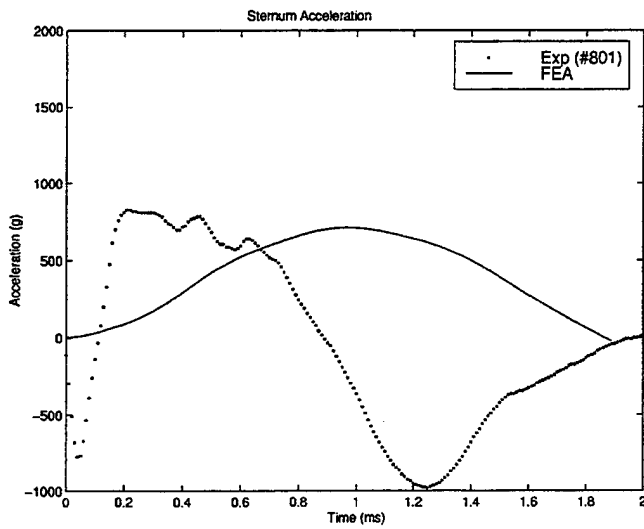
- Thorax dimensions increased by 25%, Body armor maintained at original dimensions



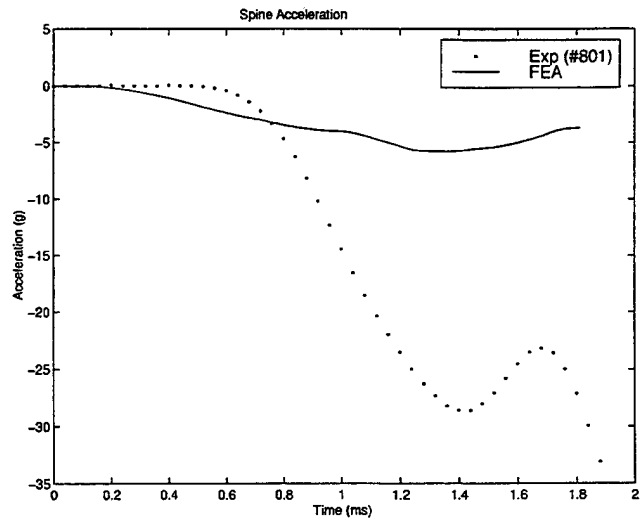
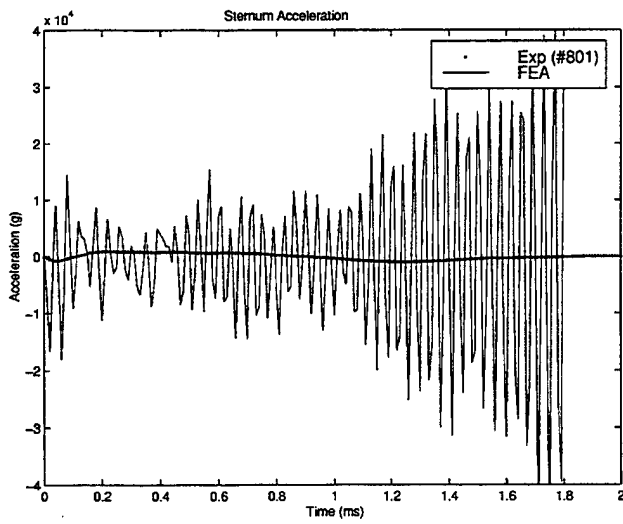
- Spring discrete element between muscle and ribs removed



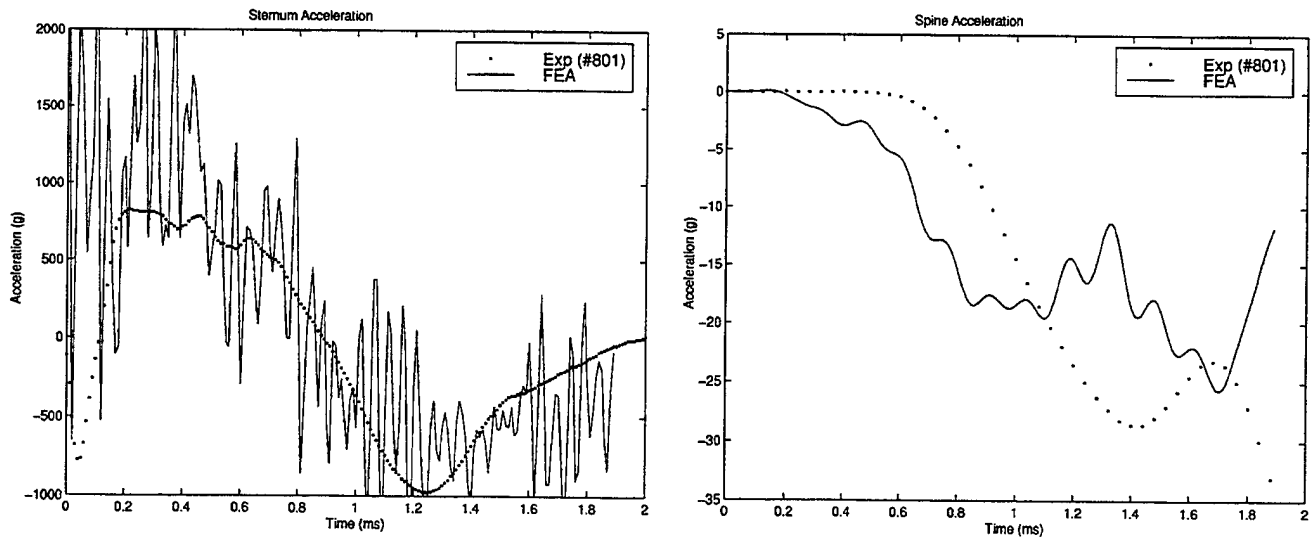
- Damper discrete element between muscle and ribs removed



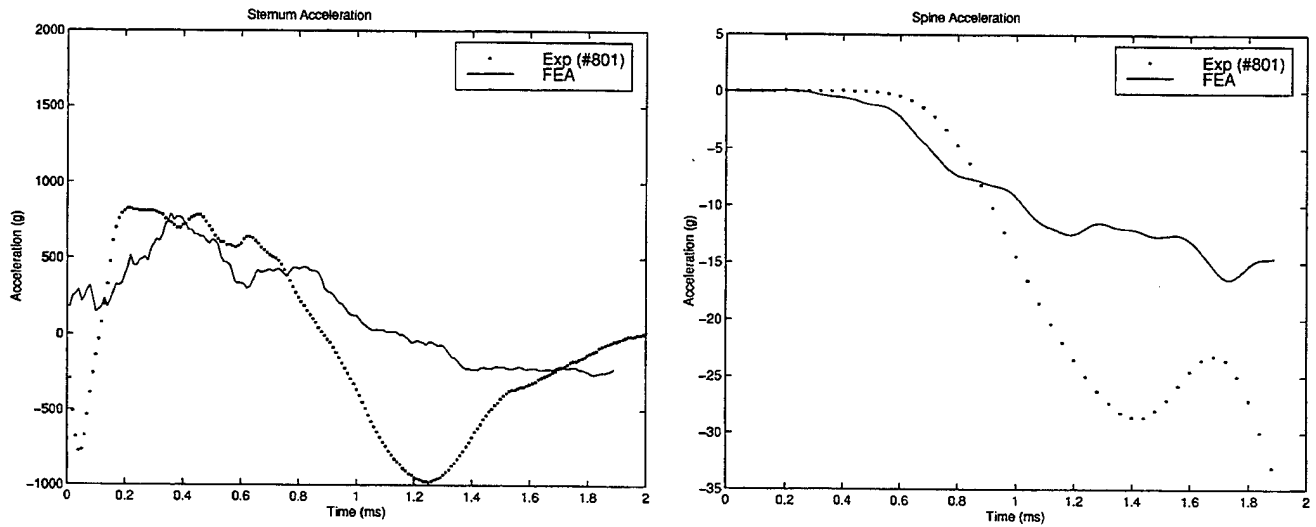
- Spring discrete elements and muscles removed from model



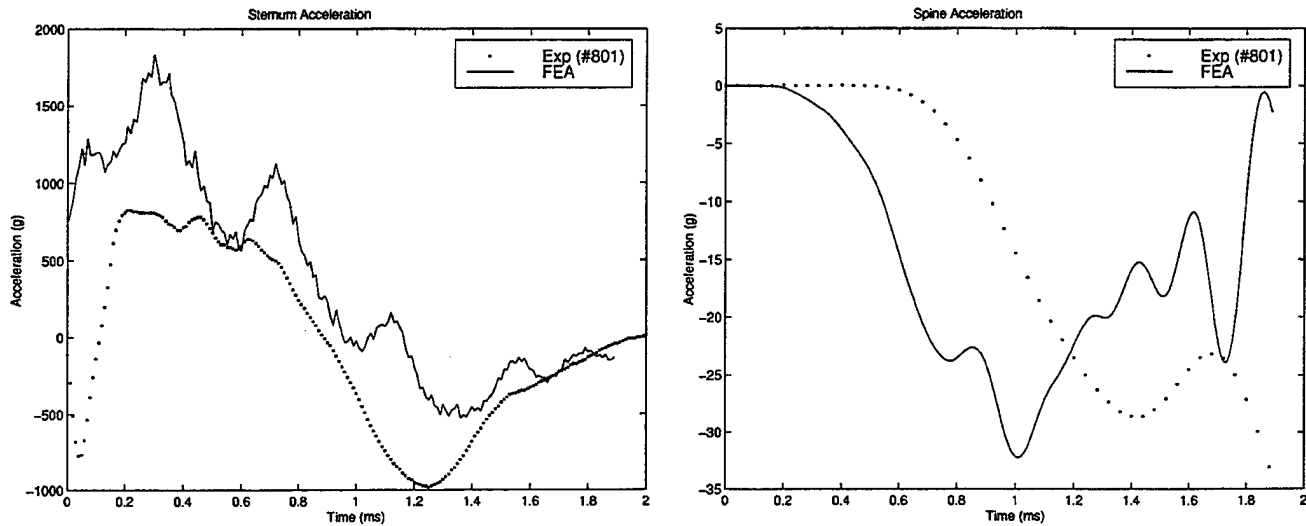
- Damper and spring discrete elements between muscle and ribs removed



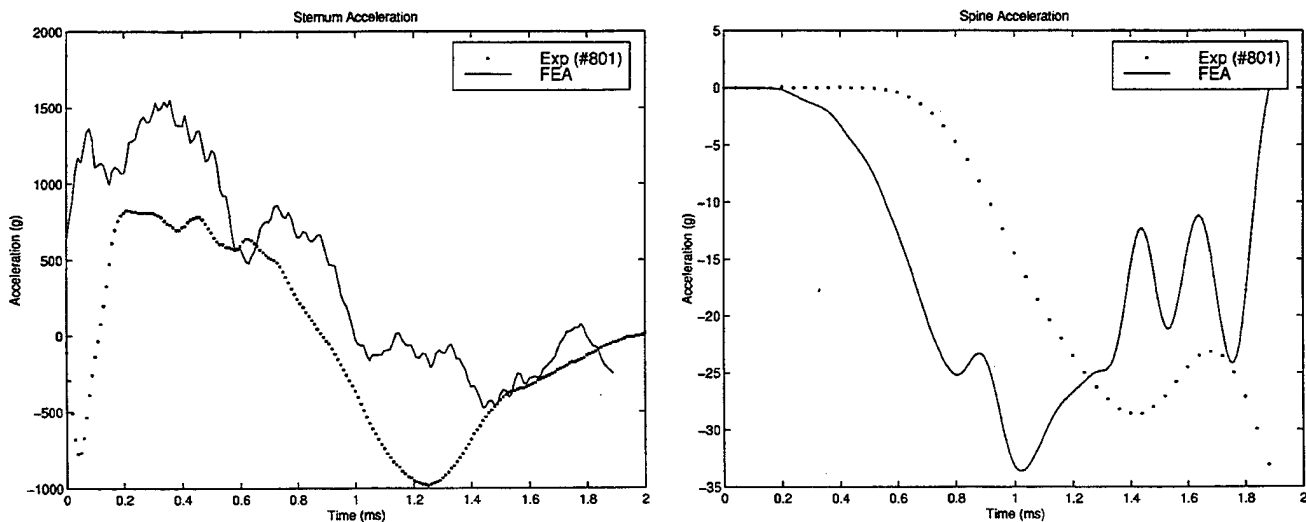
- Point of impact of projectile along sternum moved inferiorly by 6 cm



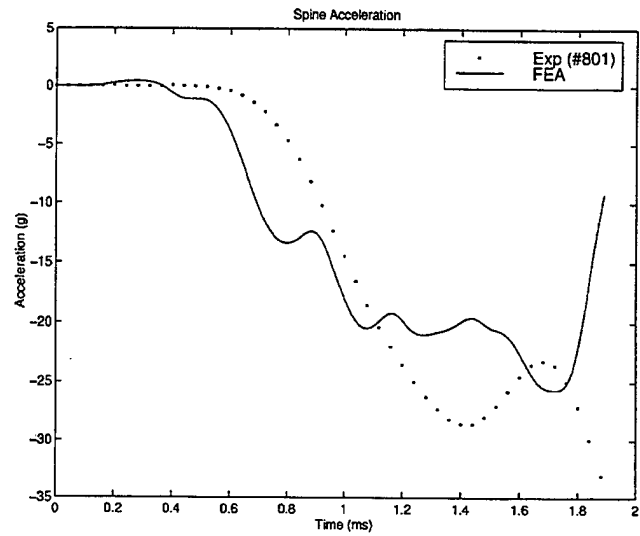
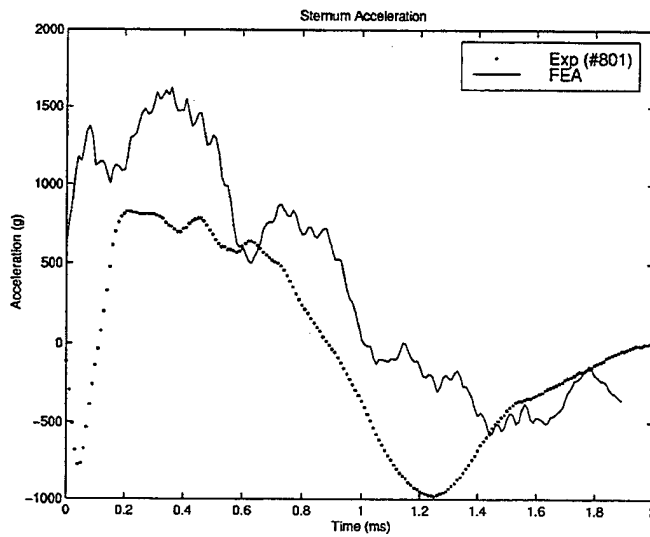
- Body armor dimensions increased to 25 cm by 18 cm, thorax dimensions constant, musculature between vest and thorax increased; densities of the CBA and Kevlar are scaled to maintain same mass for body armor; number of damper discrete elements increased



- Body armor dimensions increased to 25 cm by 18 cm, thorax dimensions constant, musculature between vest and thorax increased; densities of the CBA plate and Kevlar are not scaled; number of damper discrete elements increased



- Body armor dimensions increased to 25 cm by 18 cm, thorax dimensions constant, musculature between vest and thorax increased; densities of the CBA plate and Kevlar are not scaled; original number of dampers used



APPENDIX B: VISCOELASTIC SOLIDS

The use of a time-dependent shear modulus in the muscle elements of the thorax model was required to adequately model its viscous effects. In order to understand the theory behind the use of the equation to create the time-dependent response of the shear modulus, it is necessary to understand the modifications necessary to Hooke's Law. (See Refs. 24, 25 and 26 for a discussion on viscoelasticity.)

For a viscous material, the relationship between strain, ϵ , and stress, σ , can no longer be represented by the equation:

$$\sigma = E * \epsilon \text{ (Hooke's Law)}$$

Instead, various models are created to represent the behavior of a viscoelastic material. Several of these are depicted in Figure 56 below. By placing a combination of springs and "dashpots," modeled by the dampers, in series and in parallel, it is possible to create the desired behavior of the solid.

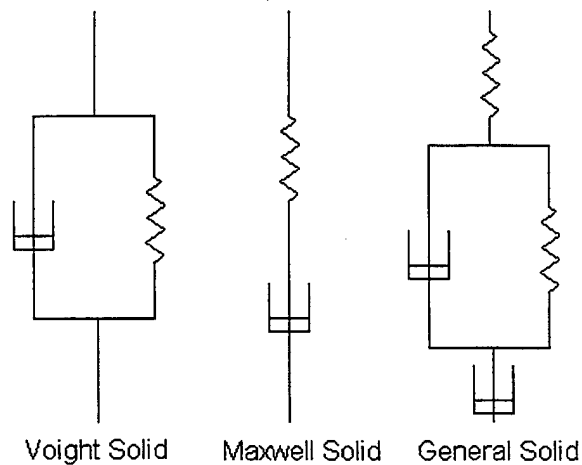


Figure 56: Models of Viscoelastic Solids. From Ref. [24]

The viscoelasticity represented by the DYNA3D material model is represented in Figure 57 below.

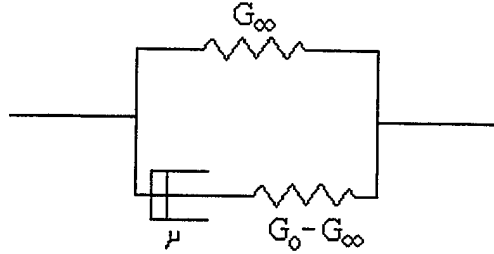


Figure 57: Model of DYNA3D Viscoelastic Solid

In order to determine the behavior of this model, the stress-strain relationships must be determined. In general, the behavior of a massless, linear spring with a spring constant, K , follows Hooke's Law,

$$\sigma = K * \varepsilon,$$

with σ as the stress and ε as the strain. [Ref. 25] The relationship between stress and strain in the dashpots is as follows,

$$\sigma = \mu * \dot{\varepsilon},$$

with μ as the viscosity of the dashpot and $\dot{\varepsilon} = \frac{d\varepsilon}{dt}$. [Ref. 25]

In order to determine the time-dependent shear modulus, the first step is to find the stress-strain relationship for the model presented in Figure 57. Since the model has elements both in series and in parallel, it is essential to know how stresses and strains combine for these combinations. For a dashpot and spring in series, illustrated by the

Maxwell solid in Figure 56, the stress in the series is equal to the stress in each element and the strain is the sum of the strain in the two elements, such as $\sigma = \sigma_K = \sigma_\mu$ and $\varepsilon = \varepsilon_K + \varepsilon_\mu$, with K as the spring constant and μ as the dashpot viscosity. For a dashpot and spring in parallel, illustrated by the Voight solid in Figure 56, the stress is equal to the sum of the stresses in each element and the strain is the equal to the strain in each individual element, such that $\sigma = \sigma_K + \sigma_\mu$ and $\varepsilon = \varepsilon_K = \varepsilon_\mu$. [Ref. 26]

For the model utilized by DYNA3D, the stresses in each branch must be computed individually and then combined according to the relationships presented above. Let the top branch, with the singular spring element, be branch A and let the bottom branch be branch B. First, compute the stresses and strains for branch B, according to the Maxwell model. Since $\varepsilon = \varepsilon_K + \varepsilon_\mu$, $\sigma = K * \varepsilon$, and $\sigma = \mu * \dot{\varepsilon}$, the following relationship can be determined for branch B:

$$\frac{\sigma_B}{\mu} + \frac{\dot{\sigma}_B}{G_0 - G_\infty} = \dot{\varepsilon}_B \text{ or rewritten, } \sigma_B = \left(\dot{\varepsilon}_B - \frac{\dot{\sigma}_B}{G_0 - G_\infty} \right) \mu$$

For Branch A, Hooke's Law applies and $\sigma_A = G_\infty * \varepsilon_A$.

Placing the elements in parallel, $\sigma = \sigma_A + \sigma_B$ and therefore, $\dot{\sigma} = \dot{\sigma}_A + \dot{\sigma}_B$.

Combining the terms yields the following:

$$\sigma = \sigma_A + \sigma_B = G_\infty * \varepsilon_A + \left(\dot{\varepsilon}_B - \frac{\dot{\sigma}_B}{G_0 - G_\infty} \right) \mu$$

Now,

$$\sigma + \left(\frac{\mu}{G_0 - G_\infty} \right) \dot{\sigma} = \mu \dot{\varepsilon}_B + G_\infty * \varepsilon_A.$$

Substituting in $\varepsilon = \varepsilon_A = \varepsilon_B$ and $\dot{\varepsilon} = \dot{\varepsilon}_A = \dot{\varepsilon}_B$,

$$\sigma + \left(\frac{\mu}{G_0 - G_\infty} \right) \dot{\sigma}_B = \mu \dot{\varepsilon} + G_\infty * \varepsilon, \text{ and}$$

$$\left(\frac{G_0 - G_\infty}{\mu} \right) \sigma + \dot{\sigma}_B = (G_0 - G_\infty) \dot{\varepsilon} + \left(\frac{(G_0 - G_\infty) * G_\infty}{\mu} \right) * \varepsilon$$

Finally, since $\dot{\sigma} = \dot{\sigma}_A + \dot{\sigma}_B$, then $\dot{\sigma} = G_\infty * \dot{\varepsilon}_A + \dot{\sigma}_B$ or $\dot{\sigma}_B = \dot{\sigma} - G_\infty * \dot{\varepsilon}_A$.

So,

$$\dot{\sigma} + \left(\frac{G_0 - G_\infty}{\mu} \right) \sigma = G_0 * \dot{\varepsilon} + \left(\frac{(G_0 - G_\infty) * G_\infty}{\mu} \right) * \varepsilon,$$

which is the stress-strain relationship for this model.

In order to find the shear modulus of the material, which is dependent upon the spring constants and viscosity, a simplification and several substitutions are required.

First, the parameter, $\frac{\mu}{G_0 - G_\infty}$, can be represented as τ , the retardation time for the model.

Also, substitute in $\varepsilon = \varepsilon_0 [U(t)]$ and $\dot{\varepsilon} = \varepsilon_0 [\delta(t)]$. These parameters represent the application of a strain to the Maxwell solid. $U(t)$ is the unit step function and $\delta(t)$ is the

delta-dirac function. Now, integrating with the integration factor, $e^{\frac{t}{\tau}}$, gives the following:

$$\sigma * e^{\frac{t}{\tau}} = \varepsilon_0 * (G_0) \int_0^t e^{\frac{t'}{\tau}} [\delta(t')] dt' + \frac{\varepsilon_0 * (G_0 - G_\infty) * G_\infty}{\mu} \int_0^t e^{\frac{t'}{\tau}} [U(t')] dt'$$

Using the relationships that $\int_{-\infty}^t f(t') [U(t' - t_1)] dt' = [U(t - t_1)] \int_{t_1}^t f(t') dt'$ and

$\int_{-\infty}^t f(t') [\delta(t' - t_1)] dt' = f(t_1) [U(t - t_1)]$, it follows that

$$\sigma * e^{t'/\tau} = \varepsilon_0 * G_0 \left[e^{t'/\tau} \right] [U(t - 0)] + \frac{\varepsilon_0 * (G_0 - G_\infty) * G_\infty}{\mu} [U(t - 0)] \int_0^t e^{t'/\tau} dt'$$

Simplifying leads to

$$\sigma * e^{t'/\tau} = \varepsilon_0 * G_0 + \frac{\varepsilon_0 * (G_0 - G_\infty) * G_\infty}{\mu} (\tau) (e^{t'/\tau} - 1)$$

and

$$\sigma = \varepsilon_0 * G_\infty + \varepsilon_0 * (G_0 - G_\infty) * e^{-t'/\tau}$$

Thus, using a generalized form of Hooke's Law, the modulus must be

$$G(t) = G_\infty + (G_0 - G_\infty) e^{-\beta t}, \text{ with } \beta = \frac{1}{\tau}.$$

THIS PAGE INTENTIONALLY LEFT BLANK

INITIAL DISTRIBUTION LIST

	<u>No. Copies</u>
1. Defense Technical Information Center 8725 John J. Kingman Rd., STE 0944 Ft. Belvoir, VA 22060-6218	2
2. Dudley Knox Library Naval Postgraduate School 411 Dyer Rd. Monterey, CA 93943-5101	2
3. Professor Young W. Kwon, Code ME/Kw Department of Mechanical Engineering Naval Postgraduate School Monterey, CA 93943	1
4. Professor Steven R. Baker, Code PH/Sb Department of Physics Naval Postgraduate School Monterey, CA 93943	1
5. Engineering & Technology Curricular Office (Code 34) Naval Postgraduate School Monterey, CA 93943	1
6. Department of Mechanical Engineering Naval Postgraduate School Monterey, CA 93943	1
7. Department of Physics Naval Postgraduate School Monterey, CA 93943	1
8. Johannes E. Jolly, ENS, USNR 2034 Shadow Lane Neptune Beach, FL 32266	1